

ABSTRACT

Title of Dissertation: NANOMECHANICAL RESONATORS
 TOWARDS SINGLE SPIN SENSITIVITY

Harish Bhaskaran, Doctor of Philosophy, 2006

Directed By: Professor Keith Schwab
 Department of Physics

Ultrasensitive force detectors are required for progress towards single atom imaging using magnetic resonance force microscopy (MRFM). MRFM is a scanned probe imaging technique, with potential for atomic-scale, non-destructive and sub-surface imaging. To achieve the goal of single atom imaging, technical development towards realization of high magnetic field gradients as well as force detectors with very high sensitivity are necessary. Given values of field gradients that can be achieved at present (typically of the order of 10^5 T/m), force sensitivity of an atto-newton (10^{-18} N/ $\sqrt{\text{Hz}}$) at low temperatures (0.3 – 4 K) is required for single spin sensitivity. This has been achieved using optical interferometry; however, optical interferometers corrupt measurements by heating the cantilevers and inducing decoherence of spins in the sample. Thus, there is a need to develop a light-free technique to measure cantilever motion with high sensitivity. In this dissertation, a design for ultrasensitive force detection using capacitive sensing is developed. Thermomechanical noise and position detection sensitivity constraints are

addressed. The fabrication of an ultra-thin, nanomechanical force sensing cantilever with an integrated sense electrode for capacitive detection (double cantilever architecture) is accomplished. Gallium Arsenide field effect transistors with potential for integration onto the double cantilever chips are fabricated and characterized at low temperatures. Measurement techniques for capacitive detection are explored and lay the groundwork for future research towards the development of integrated nanomechanical force detectors towards single spin sensitivity for magnetic resonance force microscopy.

**NANOMECHANICAL RESONATORS TOWARDS SINGLE SPIN
SENSITIVITY**

By

Harish Bhaskaran

Dissertation submitted to the Faculty of the Graduate School of the
University of Maryland, College Park, in partial fulfillment
of the requirements for the degree of
Doctor of Philosophy
2006

Advisory Committee
Professor Peter Sandborn, Chair
Professor Keith Schwab, Co-Chair
Professor Donald Barker
Professor P Chris Hammel
Professor Patrick McCluskey
Professor Julius Goldhar

© Copyright by
Harish Bhaskaran
2006

DEDICATION

To my parents

ACKNOWLEDGEMENTS

Over the last four years I have had an opportunity to interact with some of the most amazing individuals. Keith Schwab, my advisor, mentor and the research director has been the most instrumental in the completion of this dissertation. He has accommodated me as a student with a vastly different background, and has worked in the laboratory with me on several occasions, even on weekends, helping me sort out my measurements. When this project started out, he gave me a lot of freedom to explore various schemes and supported my idea that has spawned into this whole dissertation. I feel proud to have been part of his group during a time when they have made some of the most amazing scientific advances. And through these years, he has believed in me and has given me access to his large scientific network. For all this and more and for all the memorable and enjoyable times I have had over the last four years, I cannot thank him enough.

From the day I entered his office over five years back, Professor Peter Sandborn has been supportive and encouraging. He has given me very pertinent academic advice and has kept me glued to reality. He read through this dissertation when it was still nascent and provided very thoughtful insights. I am indebted to him for his patience and help over the years and for being a fantastic advisor. Thank you very, very much.

I sincerely thank Professor Chris Hammel who has been extremely supportive of our efforts in this project. He has funded this project at the University of Maryland for four years. And he has served as an expert advisor on almost all aspects of this project, via e-mail, phone calls, and video conferencing. I would also like to express my most sincere gratitude to Dr. Denis Pelekhov. He has pointed out many experimental flaws before implementation, which could have been expensive. And his vast knowledge and ability to explain difficult concepts is astounding. Without the help and knowledge of these two individuals this dissertation would never have been complete. Professor Michael Roukes also provided initial funding for this project and I am grateful to him.

Many thanks to Professor Donald Barker for his suggestions during the PhD proposal. I am also grateful to Professor Patrick McCluskey and Professor Julius Goldhar for serving on my committee.

I thank Dr. Bruce Kane for invaluable discussions on gallium arsenide processing and countless suggestions for characterization of the FETs. I could not have completed this work without the help and companionship of immensely talented, erudite and entertaining fellow group members- Benedetta Camarota –thanks so much for all the help initially with processing. Olivier Buu and Matt LaHaye for helping me with everything from making a low-temperature probe to helping me calculate experimental

parameters. Thanks to Akshay, Emrah, Jared and Patrick for innumerable daily conversations and for helping me with helium transfers - though I suspect that had to do with concern for their safety.

I truly appreciate the time and tireless effort of Devrez Karabacak and Professor Kamil Ekinici at Boston University in trying to read-out the cantilevers optically. A thank you to Inna Kozinsky and Sotiris Masmanidis in Professor Michael Roukes' group at Caltech for useful discussions and optical measurements. Thank you to Douglas Photiadis and Joseph Vignola of the US Naval Research Laboratory for their help and continuing effort to read-out the cantilevers. I have had several useful discussions with Michael Lilly at Sandia National Laboratories on GaAs FETs and III-IV fabrication and I appreciate his advice and supply of MBE grown 2-DEG structures. I am grateful to Professor Don DeVoe for letting me use his laboratory and Professor Eyal Buks for discussions on SEM-based detection.

I am indebted to the following people for valuable academic discussions and companionship through the years - Kuldeep Amarnath, Konrad Aschenbaum, Kenton Brown, Palash Banerjee, Sylvia Florez, Kin Chung Fong, Marcia Gollub, Alex Hutchinson, Inhee Lee, Jonghee Lee, Tim Mewes, Carlos Sanchez, Camelia Selcu and Luyan Sun.

I owe several thanks to the MBE team of Lynn Calhoun, Chris Richardson and Kanakaraju Subramaniyan, without whose help this

dissertation would have been impossible. Thanks to Russel Frizzel for his diligent and extremely precise work with wafer dicing and polishing. I am grateful to Mike Khbeis for his help with several aspects of silicon processing. Thanks much to Marc Manheimer and Barry Barker for allowing me to work at this laboratory and for giving me access to many resources. Toby Olver, Steve Brown, Lisa Lucas, Salvador Martinez, Scott Horst and Dan Hinkel have kept the cleanroom safe and user-friendly and have accommodated various process requests over the years. At LPS, I have been lucky to have J.D. Dottelius (JB), Les Lorenz, and George Dearstine machine parts of exceptional quality - thanks much. I am thankful to Lon Dill for his timely response to various facility requests.

Thanks also to Margaret Lukomska, Pauline Rirksopa, Tracy Chung and Elyse Beaulieu-Lucey for cheerfully taking care of paperwork and extremely prompt and courteous response to my queries. I am especially grateful to Elyse Beaulieu-Lucey for her exceptional handling of many issues that arose for me - the only student with two advisors and funding from another department.

I am indebted to my family for their many sacrifices – the few words here cannot capture my sense of gratitude. My parents to whom I dedicate this dissertation – my Mom and my late Dad for being the best parents ever. My lovely fiancé Varsha, who has been a great support through the difficult times

and long work hours. And my sister for her love and support through the years.

TABLE OF CONTENTS

DEDICATION	ii
ACKNOWLEDGEMENTS	ii
TABLE OF CONTENTS	viii
LIST OF FIGURES	xi
LIST OF SYMBOLS	xvi
Chapter 1	1
1.1 Introduction	1
1.2 Experimental Nanomechanics	2
1.3 Metrology requirements in Nanotechnology	4
1.4 Nuclear Magnetic Resonance (NMR)	6
1.5 Magnetic Resonance Imaging (MRI)	9
1.6 Magnetic Resonance Force Microscopy	11
1.7 Motivation	13
1.8 Dissertation Tasks	14
Chapter 2	16
2.1 Introduction to Cantilever Design	16
2.2 Previous Work	17
2.3 Design Issues for MRFM Cantilevers	18
2.4 Design of Single Crystal Silicon Cantilever	22
2.5 Fabrication of SCS Cantilevers	24
2.6 The Scribing Dilemma	33
2.7 Characterization of Cantilevers	39
2.8 Fabrication of Cantilevers Using DRIE	41
2.9 A New Dicing-Saw Method for Cantilever Scribing	43

2.10	<i>Limitations of Current Measurements Schemes</i>	45
Chapter 3		47
3.1	<i>Introduction</i>	47
3.2	<i>Literature Review</i>	47
3.3	<i>Proposed force sensor</i>	50
3.4	<i>Force Sensitivity Estimations</i>	53
3.5	<i>Circuit Model for Capacitive Detection</i>	55
3.6	<i>Impedance Transformation using Tank Circuits</i>	58
3.7	<i>Impedance Transformation Using FETs</i>	61
Chapter 4		64
4.1	<i>Introduction</i>	64
4.2	<i>Fabrication Sequence</i>	64
4.3	<i>Conclusion</i>	71
Chapter 5		72
5.1	<i>Introduction</i>	72
5.2	<i>Commercial FET characterization</i>	73
5.3	<i>The Structure for Custom FET</i>	75
5.4	<i>The FET Measurement Concept</i>	77
5.5	<i>Process Development for FET Fabrication</i>	79
5.6	<i>Wide Channel FET</i>	81
5.7	<i>FETs with 21fF Input Capacitance</i>	88
5.8	<i>Conclusion</i>	94
Chapter 6		95
6.1	<i>Issues of Measurement of the Cantilever Motion</i>	95
6.2	<i>Experimental Set-Up to Read-Out Cantilevers</i>	95
6.3	<i>SEM-Based Detection</i>	101
6.4	<i>Optical Detection of Cantilevers</i>	103
6.5	<i>Discussion</i>	104

Chapter 7	105
7.1 <i>Introduction</i>	<i>105</i>
7.2 <i>Proposed Direct Impedance Transformation</i>	<i>106</i>
7.3 <i>Contributions</i>	<i>110</i>
7.4 <i>Towards Single Spin Sensitivity – Future Work</i>	<i>111</i>
Appendix A	113
Appendix B	118
Appendix C (Electronic file)	121
References	122

LIST OF FIGURES

- Figure 1.1 The charged nucleus (e.g., ^1H) rotating with angular frequency $\omega_0=2\pi\nu_0$ creates a magnetic field B and is equivalent to a small bar magnet whose axis is coincident with the spin 7
- Figure 1.2 The phenomenon of flipping of energy states (spontaneous, upon application of RF energy, free induction decay (FID) after signal is withdrawn and return to thermal equilibrium, in that order, left to right) 8
- Figure 1.3 Schematic Operation of a one-dimensional MRI system. The magnetic field gradient generates a precession frequency gradient. A receiver picks out one frequency w_0 in a band of width Δw , allowing detection of the atoms in a slice at z_0 of width Δz , [1] 10
- Figure 2.3 Step 1: Deposit 100 nm (1000 Å) thick Silicon Nitride on both sides of the wafer 27
- Figure 2.8 The requirement of 'cantilever on an edge' represented schematically 32
- Figure 2.11 SEM image of a set of six cantilevers fabricated on a long (1.2mm) membrane 37

Figure 2.12 Set-up for scanning capacitive microscopy. The set-up shown also shows sample positioning and the magnetic fields as in an actual MRFM experiment. For characterization purposes, only sensing probe and cantilever without the sample and magnetic fields was employed. The cantilever was resonated using a piezoelectric resonator and the resulting resonance was sensed	39
Figure 2.13 Capacitively detected response of a triangular cantilever. The signal was acquired at $T = 300$ K in vacuum	41
Figure 2.14 Figure showing cantilevers fabricated using DRIE. Four different lengths of cantilevers were fabricated.	42
Figure 2.15 Edge Suspension of a cantilever using a dicing saw process	45
Figure 3.2 Cross-sectional view of proposed capacitive detection scheme. The glued magnet will be shaped using focused ion milling techniques	52
Figure 3.3 Representation of a mechanical element (moving) coupled to a sensing electrode for capacitive sensing.	56
Figure 3.4 The equivalent circuit of a voltage biased nanomechanical resonator and gate device. I_{CO} is the current through gate capacitance, and I_{RLC} is the current through the resonant circuit.	58

Figure 3.5 Tank circuit for transformation of an impedance Z . Note the two components of the tank circuit, the capacitance and the inductance	60
Figure 4.1 Fabrication sequence for double cantilever layer. The topmost layer (30 nm thick GaAs) is the resonator layer. The third layer (500 um GaAs) is the reference cantilever	66
Figure 4.2 Deep etch through GaAs carried out by the MEMS and Nanotechnology Exchange.	68
Figure 4.3 Two SEM micrographs showing double cantilevers before and after the selective HF etch. The picture on the right after the HF etch shows how critical point drying is necessary in order to prevent surface tension forces from causing damage	69
Figure 4.4 SEM micrographs of a cantilever chip. The left one shows a chips complete with bond pads and the cantilevers at the end of an 'arm'. The right shows the double cantilever	70
Figure 5.1 Measurement showing instabilities in the I-V curves for a ATF-35143 HEMT at 4.2 K	74
Figure 5.2 Cross sectional view of the field effect transistor (FET) to show the structure of growth	76

Figure 5.3 Schematic showing the FET structure including the drain, source and gate	76
Figure 5.4 Circuit model showing impedance tranformation using 2 FETs, once with lower gate capacitance and other with higher gate capacitance but greater bandwidth	78
Figure 5.5 Optical Microscope images of a bond pad pre and post annealing. The picture on the right shows an annealed contact, and surface roughness is seen clearly	80
Figure 5.6 Optimization of annealing times. Resistance drops as contact is made to the 2DEG	80
Figure 5.7 An optical microscope image of a wide-channel GaAs FET	82
Figure 5.8 Measured I-V Characteristic for the Wide FETs at 295 K	84
Figure 5.9 Measured Transfer Characteristic of wide FET at 293 K	85
Figure 5.10 Measured I-V Characteristic of Wide FET at 4.2 K	86
Figure 5.11 Measured Transfer Characteristic of wide FET at 4.2 K	87
Figure 5.12 SEM Micrograph of a FET with lower capacitance	89
Figure 5.13 Close-up of the gate region of the channel	90
Figure 5.14 Measured I-V characteristic for the low capacitance FET at 4.2K	90
Figure 5.15 Measured transfer characteristic for the low capacitance FET at 4.2 K	91

Figure 5.16 A simplified circuit demonstrating the use of FETs as amplifiers	92
Figure 5.17 Measured relationship between gain and power dissipation	93
Figure 6.1 Figure showing the mounting of cantilever on piezoelectric stack to minimize cross-talk	97
Figure 6.2 Circuit for measurement of cantilevers coupled to the wide FET	98
Figure 6.3 Photograph showing the circuit board used for measurements	99
Figure 7.1 Transformation of Mechanical Impedance to the lower input impedance of amplifier by a tank circuit	108
Figure A.1 Representation of a mechanical element (moving) coupled to a sensing electrode for capacitive sensing.	113
Figure B.1 Both sides of the circuit board are shown	118
Figure B.2 The bottom of the probe showing the connections and the board attachment	119
Figure B.3 Clockwise from left: The probe; close up of the top of the probe showing the BNC connectors, pressure gauge and the evacuation valve; The bottom can and that can be screwed on hermetically with an indium seal.	120
Figure C.1 Snap-shot showing the spreadsheet that is attached as an electronic file to this dissertation	121

LIST OF SYMBOLS

<u>Symbol</u>	<u>Description</u>
ΔE	Energy difference between two nuclear spin orientations
B_0	Strength of magnetic field
γ_N	Gyro magnetic ratio of nucleus
ν_0	Frequency of nuclear transition
h	Planck's constant = 6.63×10^{-27} erg s
B	Net Magnetic field at a given point
B_0	Uniform magnetic field
b	Field gradient in NMR
F	Force to be measured
\mathbf{m}	Spin magnetization
∇B	Field Gradient due to magnetic tip in MRFM
Q	Quality factor of resonator
f_c	Resonant frequency of cantilevers
t	Thickness of cantilever
E	Elastic modulus of material
ρ	Density of material

S_F	Square of spectral density of force noise
ΔF	Spectral density of force noise
k	Spring constant (stiffness) of cantilever
k_B	Boltzmann constant = $1.3806503 \times 10^{-23} \text{ m}^2 \text{ kg s}^{-2} \text{ K}^{-1}$
T	Temperature in K
V_{osc}	Harmonic AC voltage applied for scanning capacitive microscopy in 2.7
A_{res}	Amplitude of cantilever at resonance
d_{33}	Coefficient of piezoelectric material
$\sqrt{S_d}$	Spectral density of displacement noise
$\sqrt{S_v}$	Spectral density of voltage noise resolution
C_{Total}	Total capacitance, including all parasitic capacitance
C_{Cant}	Capacitance between parallel plates of the cantilevers
V_{Bias}	Bias DC voltage between the cantilevers
d	Gap between the plates of the double cantilever
L_m	Inductance of equivalent RLC circuit
C_m	Capacitance of equivalent RLC circuit
R_m	Resistance of equivalent RLC circuit
m	Mass of cantilever
C_s	Parasitic (stray) capacitance
V_{DS}	Drain-source voltage for FETs

V_{GS}	Gate-source voltage (voltage potential a gate)
I_{DS}	Drain-source current
g_m	Transconductance of FET
R_D	Bias resistor (for FET amplification)
Z_{LC}	Impedance of tank circuit
C_{TANK}	Capacitance required for tank circuit
L_{TANK}	Inductance required for tank circuit

Chapter 1

NANOMECHANICS FOR MAGNETIC RESONANCE FORCE MICROSCOPY

1.1 Introduction

The field of nanomechanics, a recently coined term, has been rapidly expanding with the surge in research in the field of nanotechnology. While nanotechnology is a broad term that is highly interdisciplinary, nanomechanics concentrates on aspects of this science primarily in the fields of Physics and Mechanical Engineering. It is a subset of nanotechnology, but a core knowledge area that helps in understanding the behavior of systems close to and smaller than the nanometer regime.

Nanomechanics as a field, has seen a significant developments in recent years because of vast advances in nanofabrication technology. The knowledge gained in fabrication and characterization of microelectromechanical devices (MEMS) has helped nanomechanics researchers make devices to observe phenomena previously not possible. Using novel materials to make microelectromechanical systems is a challenge, since the majority of microelectromechanical systems have been polysilicon based, as such spawning an entire infrastructure aimed at fabricating such structures [MUMPS, MOSIS]. Silicon nitride devices have been popular in nanomechanical devices because of the relative simplicity of fabrication as

well as the availability of good quality nitride films in the market. More recently, single crystal structures of silicon and gallium arsenide have also been used, though the higher cost of fabrication of such devices has greatly limited their use.

This chapter is aimed at giving a brief introduction to this novel field and the relevance of this dissertation in the development of this field. This dissertation focuses on the experimental techniques that extend the technological know-how in this field; hence much of the introduction will be in experimental nanomechanics. An introduction to magnetic resonance force microscopy is included and will serve as the backdrop for the rest of the dissertation.

1.2 Experimental Nanomechanics

Cleland [1] regards nanomechanics to be the mechanical behavior of nanometer-scale objects. Experimental nanostructures are often built to investigate various mechanical properties and applications of nanomechanical devices. Almost all experimental structures in nanomechanics are currently made using semiconductor processing techniques. Of course many experimental structures have potential applications either as the original structure or with modifications.

Nanomechanics has origins in many of the traditional fields (such as Physics, Mechanical Engineering, Electrical Engineering, Materials Science, Civil Engineering and the life sciences). This is because at the nanoscale, seamless integration of mechanical (structural) and electrical components is required, which in many cases obey the bizarre laws of quantum mechanics and demonstrate behavior highly dependent on the local properties of materials. Thus, the boundaries between the various fields have to be scaled in order to design systems with useful applications. More recently nanomechanics has come to be regarded as a subset of Mechanical Engineering and Physics – the use of engineering design tools such as the continuum theory combined with quantum mechanics to produce new tools such as the enriched continuum theory [2] have required engineers to learn the fundamentals of Physics normally not taught to mechanical engineers. Thus, both design tools as well as fabrication technologies have to be developed. **This dissertation is intended to be in the area of experimental nanomechanics.** As such, it will talk about experimental structures that can interact with elements that are governed by quantum mechanics.

Recent nanomechanical devices have demonstrated the theory of the limit of heat transfer [2], achieved very high displacement sensitivity [4], approached very close to the Heisenberg limit [5], [6] and have achieved sub-attoneutron force sensitivity [7] among other things. Clearly all the

applications listed above have bearing on future technological development. For instance, the Schwab-Roukes experiment in [2] determines the limit of thermal conductance which could be an important factor in electronic devices of the future as decreasing feature sizes could be limited. As evidenced later, the device described in [7] represents many aspects of the goal of this dissertation.

1.3 Metrology Requirements in Nanotechnology

One of the important requirements in the emerging field of nanotechnology is to be able to characterize materials at the nanoscale. While many new techniques are being employed (for instance, in [8]), it is widely accepted that most of these methods have severe limitations, both physical as well as in terms of generating pertinent information. The accurate characteristics of material properties is very important in nanomechanics, since micro-anomalies, normally ignored in engineering design with good reason, play an important role at these scales. Since in nanostructures, the interdependence of mechanical and electrical properties of the material are often exploited, the designer must take into account these properties, for which these properties must be well established.

Some of the important tools in current use are the nano-indentors, the atomic force microscope (AFM), the scanning probe microscope (SPM), the

electron microscope (both transmission mode (TEM) and scanning mode (SEM)) and some laboratory equipment such as profilometers etc. that yield limited scale-specific information. The AFM has been a very useful tool in the emerging field of nanotechnology, since it can produce ultra-high resolution images of surfaces. Another of the important tools of the twentieth century has been Nuclear Magnetic Resonance Imaging (NMR). NMR and its modified form Magnetic Resonance Imaging (MRI) have yielded interesting and useful information helping us better understand human anatomy, drug performance and chemical potentials in solutions among many other things.

There is no doubt that the concept of NMR is a powerful and indispensable tool for scientists, engineers and healthcare professionals. NMR provides a non-destructive (or non-invasive) technique to produce images of structures well below the surface. As for the AFM, it has been adapted by micro- and nanotechnologists to perform various applications beyond what it was originally designed for. (See [9] for an example)

A combination of MRI and AFM, i.e. a tool that has the three dimensional imaging capabilities of MRI, while at the same time having the lateral resolution of AFM would be the ideal tool for studying nanoscale materials and devices, as well to exploit properties of nanofabricated devices. Such a tool would enable metrology of nanostructures in-situ or otherwise and would provide a wealth of information about the characteristics of materials at the

nanoscale. In addition it would enable molecular imaging, which will revolutionize research in the biological and medical sciences. The fundamentals of development of such a tool are presented in this chapter and serves as the motivation for this dissertation.

1.4 Nuclear Magnetic Resonance (NMR)

The fundamentals of nuclear magnetic resonance are as follows. If a sample is placed in a magnetic field and is subjected to radiofrequency (RF) radiation (energy) at the appropriate frequency, nuclei in the sample can absorb the energy. The frequency of the radiation necessary for absorption of energy depends on three things. First, it is characteristic of the type of nucleus (e.g., ^1H or ^{13}C). Second, the frequency depends on chemical environment of the nucleus. The NMR frequency also depends on spatial location in the magnetic field if that field is not uniform. This last variable provides the basis for magnetic resonance imaging (MRI).

NMR is a well characterized technique and there is a large quantity of literature in the field. A short tutorial that the following description follows is found in [10]. A brief description of the nuclear magnetic resonance follows herewith. A spinning nucleus acts as a tiny bar magnet oriented along the spin rotation axis. If we put this small magnet in the field of a much larger magnet, its orientation will no longer be random. There will be one most probable

orientation. However, if the small magnet is oriented *precisely* 180° in the opposite direction, that position could also be maintained, i.e. the most favorable orientation would be the low-energy state and the less favorable orientation the high-energy state. This two-state description is appropriate for most nuclei of biologic interest including ^1H , ^{13}C , ^{15}N , ^{19}F , and ^{31}P ; i.e., all those which have nuclear spin quantum number $1/2$. It is a quantum mechanical requirement that any individual nuclear spins of a nucleus with spin quantum number $1/2$ be in one of the two states (and nothing in between) whenever the nuclei are in a magnetic field. It is important to note that the most common isotopes of carbon, nitrogen and oxygen (^{12}C , ^{14}N and ^{16}O) do not have a nuclear spin.

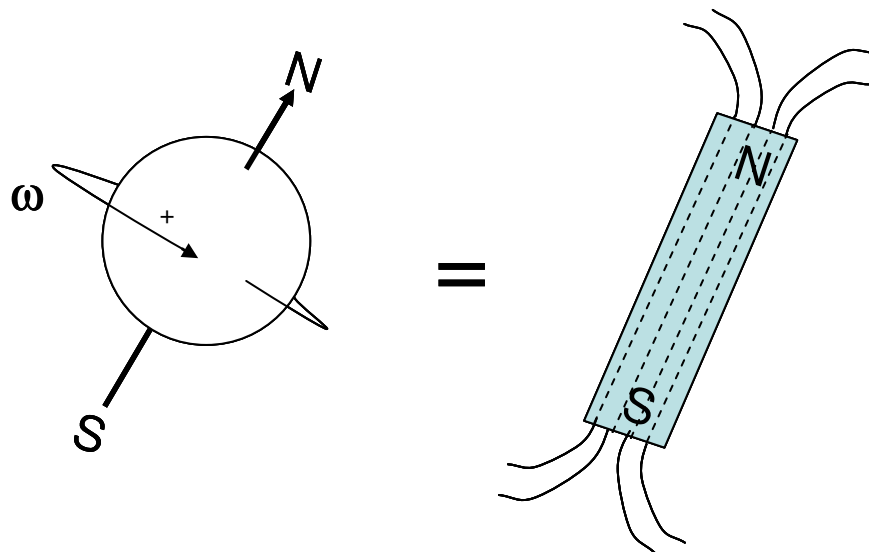


Figure 1.1 The charged nucleus (e.g., ^1H) rotating with angular frequency $\omega_0=2\pi\nu_0$ creates a magnetic field B and is equivalent to a small bar magnet whose axis is coincident with the spin

The small nuclear magnet may spontaneously "flip" from one orientation (energy state) to the other as the nucleus sits in the large magnetic field. This relatively infrequent event is illustrated at the left of Figure 1.2. However, if energy equal to the difference in energies (ΔE) of the two nuclear spin orientations is applied to the nucleus (or more realistically, group of nuclei), much more flipping between energy levels is induced. The irradiation energy is in the radio frequency (RF) range and is typically applied as a short pulse. The absorption of energy by the nuclear spins causes transitions from higher to lower energy as well as from lower to higher energy. This two-way flipping is a hallmark of the resonance process. The energy absorbed by the nuclear spins induces a voltage that can be detected by a suitably tuned coil of wire, amplified, and the signal displayed as a *free induction decay (FID)*. Relaxation processes (*vide infra*) eventually return the spin system to thermal equilibrium, which occurs in the absence of any further perturbing RF pulses.

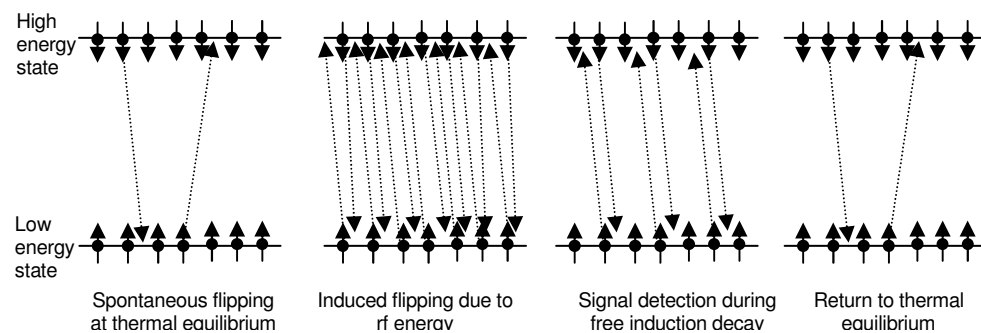


Figure 1.2 The phenomenon of flipping of energy states (spontaneous, upon application of RF energy, free induction decay (FID) after signal is withdrawn and return to thermal equilibrium, in that order, left to right)

The energy required to induce flipping and obtain a NMR signal is just the energy difference between the two nuclear orientations and depends on the strength of the magnetic field B_0 in which the nucleus is placed. It is given by:

$$\Delta E = \gamma h B_0 / 2\pi \quad (1.1)$$

where h is Planck's constant (6.63×10^{-27} erg s). The Bohr condition ($\Delta E = h\nu$) enables the frequency ν_0 of the nuclear transition to be written as:

$$\nu_0 = \gamma B_0 / 2\pi \quad (1.2)$$

Equation 1.2 is often referred to as the Larmor equation, and $\omega_0 = 2\pi\nu_0$ is the angular *Larmor resonance frequency*. The *gyromagnetic ratio* γ is a constant for any particular type of nucleus and is directly proportional to the strength of the tiny nuclear magnet. At magnetic field strengths used in NMR experiments the frequencies necessary to fulfill the resonance condition (Equation (1.2)) are in the RF range; e.g. in a magnetic field of 14.1 T, the transition frequency ν_0 for ^1H is 600 MHz.

1.5 Magnetic Resonance Imaging (MRI)

As mentioned in section 1.4, the NMR frequency also depends on spatial location in the magnetic field if that field is not everywhere uniform. This variable provides the basis for magnetic resonance imaging (MRI).

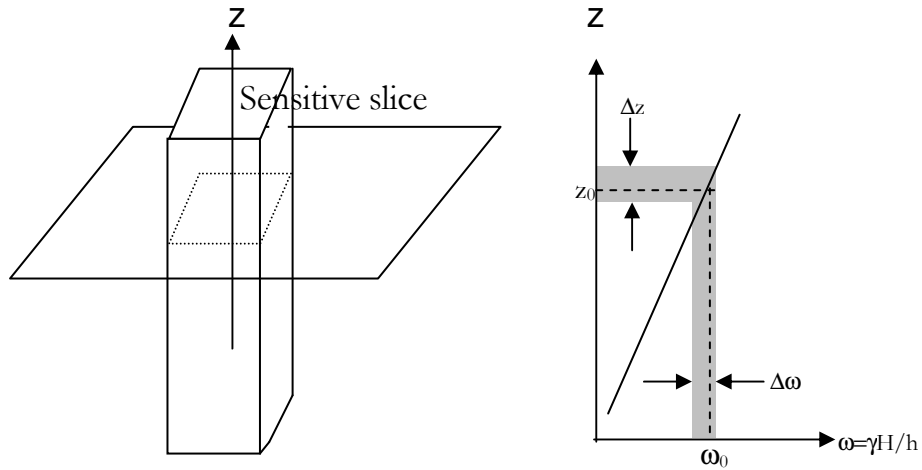


Figure 1.3 Schematic Operation of a one-dimensional MRI system. The magnetic field gradient generates a precession frequency gradient. A receiver picks out one frequency ω_0 in a band of width $\Delta\omega$, allowing detection of the atoms in a slice at z_0 of width Δz , [1]

In MRI, the use of controlled field gradients allow select ‘slices’ of nuclei at specific depths in the sample to be in resonance. The gradient of the field influences the thickness of the resonant slice – greater the gradient thinner the slice, thus superior resolution. The state of the art MRI can resolve to about $1\mu\text{m}$. MRI forms the basis for the magnetic resonance force microscope.

A brief description of the MRI as described in [1] is provided. A magnetic field with a gradient $B = (B_0 + bz)\hat{z}$ is applied to the object to be imaged. Here b is the field gradient, in units of T/m. At each point z , a particular type of atom (typically hydrogen) will have a local precession frequency $w_p(z) = \gamma_N(B_0 + bz)$. A receiver for the NMR signal tuned to a particular frequency w_0 will only pick up frequencies near w_0 and therefore will detect atoms with z coordinate near $z_0 = w_0 / (\gamma - B_0) / b$. If the bandwidth of receiver input frequency acceptance is

$\Delta\omega$, it will detect atoms centered at this height, in a slice of thickness $\Delta z = \Delta\omega / \gamma_N b$. The uniform field B_0 can then be changed slightly allowing detection in a slice at a somewhat different location, and thus by measuring the signal as a function of B_0 , the composition of an extended solid along the z-axis can be mapped out.

The proposed magnetic resonance force microscope (MRFM), originally envisioned by Sidles [11] is described in the following section.

1.6 Magnetic Resonance Force Microscopy

The use of nanomechanical devices to develop a microscopic imaging technique known as “magnetic resonance force microscopy” or simply MRFM has been among the thrust areas in nanomechanics in the last decade. MRFM is a visionary project the ultimate goal of which is to enable imaging of various atoms on a surface (and below it), complete with identification of the element. This would give a resolution of a single atom.

MRFM was proposed by Sidles [11] in 1991. The fundamentals of this proposal are as follows. A molecule whose structure is to be determined is placed below a sharp magnetic tip. The magnetic tip is attached to a sensitive micromechanical cantilever that will bend in response to small forces, including the magnetic forces due to the magnetic nuclei in the sample. (Many common elements, such as hydrogen, fluorine, carbon-13, phosphorus, etc.,

have magnetic nuclei.) Nuclear magnetic resonance is used to manipulate individual nuclei that are just the right distance from the tip (i.e., within the “resonant slice”). By applying a suitably modulated radiofrequency (RF) magnetic field using a small coil, the magnetic moment of the nucleus within the resonant slice can be flipped up, down, up, down, etc., thus generating an alternating force on the tip that causes the cantilever to vibrate slightly. This vibration is detected using a sensitive position detection scheme. By scanning the sample with respect to the tip in a three-dimensional raster pattern, an image of the atomic structure of the molecule can, in principle, be obtained. Figure 1.4 shows a schematic of an MRFM apparatus.

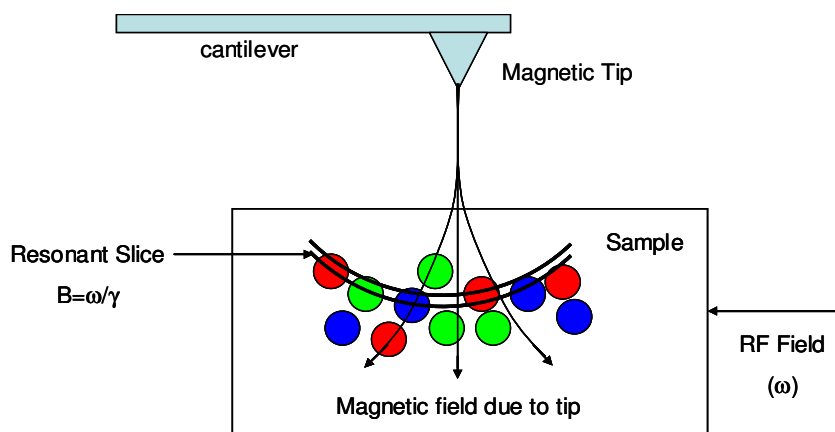


Figure 1.4 A schematic of the MRFM imaging apparatus

MRFM with single-nucleus sensitivity is still beyond present-day experimental capability because the magnetic force generated by an individual nucleus is so small ($\sim 10^{-20}$ N). Present research activity is focused

on the detection of individual unpaired electron spins with angstrom-scale spatial resolution. Despite the thousand-fold larger magnetic moment of the electron (10^{-17} N), the goal of single electron spin detection and imaging is a challenging one. This is because the forces that need to be detected are still extremely small - in the attonewton range - and because the behavior of individual spins in the presence of a nearby ferromagnetic tip is not well understood. Recent experiments by Rugar et al. have demonstrated the detection of a single electron spin [16].

1.7 Motivation

The motivation for this dissertation is laid out in the Sidles proposal to build a Magnetic Resonance Force Microscope. A working MRFM will transform imaging technology and result in a rapid progress in the field of nanomechanics, which is an essential theoretical field for the development of nanotechnology. Beyond the anticipated imaging capabilities of the MRFM, it can be used to carry out a number of interesting experiments that can result in exotic machines. One such application is to use such a MRFM as a possible read-out scheme for solid state quantum computing scheme proposed by Kane [12].

In magnetic resonance force microscopy (MRFM) mechanical detection of magnetic resonance signals is carried out by sensitively measuring the force

$F = \mathbf{m} \cdot \nabla B$ between a permanent magnet that provides a field gradient ∇B , and the spin magnetization \mathbf{m} . Periodically modulating this force by modulating \mathbf{m} alters the oscillation amplitude of a high Q, low spring-constant micro-mechanical resonator (cantilever or bridge) such as is used presently in AFM. A schematic of a MRFM is shown in Figure 1.5. The focus of this dissertation is the design and fabrication of a force detector, with sufficient sensitivity to detect single electron spins.

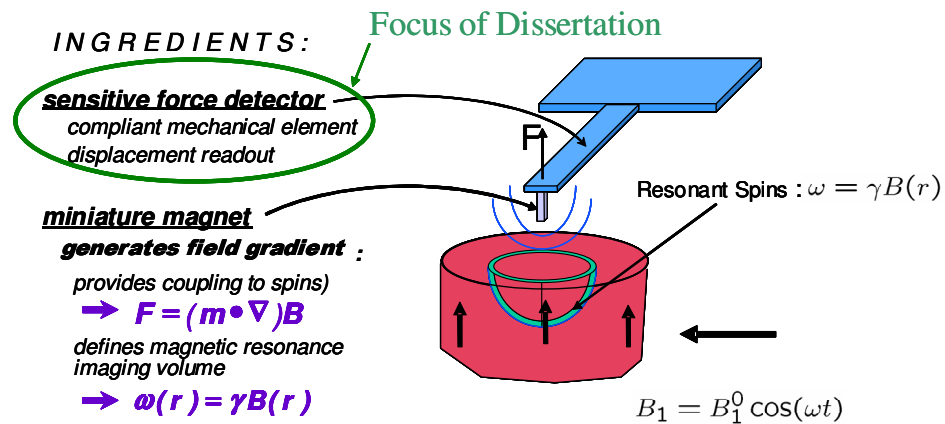


Figure 1.5 Necessary ingredients for a proposed magnetic resonance force microscope (P.C. Hammel, D.V. Pelekhov, and M.L. Roukes). The design and fabrication of the sensitive force detector is the focus of this dissertation

1.8 Dissertation Tasks

The major goal of this dissertation is to design and develop cantilevers with sufficient sensitivity to detect single spins. This would entail cantilevers that have a force sensitivity of at least $\sim 10^{-18} \text{ N} / \sqrt{\text{Hz}}$. Another desired requirement is the development of a lightless position detection scheme to

detect frequency shifts of the cantilevers. This is desirable since even a small amount of sub-bandgap light is known to increase relaxation rates in semiconducting samples by several orders of magnitude [13]. While these goals are general, I have defined the following tasks to be completed in this dissertation:-

1. To design and fabricate Single Crystal Silicon (SCS) cantilevers with frequencies in the 5 – 60 kHz regime
2. To develop a process for high yield scribing of cantilevers in order to suspend cantilevers on-an-edge
3. To conceive and design a light-free, ultra sensitive force sensing scheme in order to detect forces of the order of at least 10^{-18} N/ $\sqrt{\text{Hz}}$ for a single electron spin at a temperature of 0.3 K.
4. To develop processes for fabrication of ultra-thin cantilevers and other required electronic components with sufficient sensitivity
5. To fabricate and characterize field effect transistors for use as low temperature amplifiers
6. To make measurements of the designed components to verify suitability for low temperature experimentation

Chapter 2

THE SINGLE CRYSTAL SILICON CANTILEVER

2.1 Introduction to Cantilever Design

The design of cantilevers for ultrasensitive applications by itself is not novel, as seen in Section 2.2. However the design and fabrication of such structures with high yields is very involved and is not trivial. While the design of integrated force sensors is a good approach, one of the most prohibitive issues for single electron or atom magnetic resonance force microscopy is the design of a position detection mechanism that is sensitive to a single electron spin (for electron spin resonance) and a single nuclear spin (for species identification). It has been demonstrated in [16] that this can be achieved using optical interferometry, though its suitability for nuclear spin detection is unknown. While this approach is the most straightforward, it has some inherent disadvantages. These disadvantages include heating of the cantilevers, alignment issues and increased relaxation rates of spins in the sample [13].

Another serious issue is the thermomechanical noise of the resonator. The thermomechanical noise in MEMS is a well known phenomenon that restricts the measurement sensitivity of many devices [14]. Analogous to Johnson's noise in resistors, this noise has a direct dependence on the temperature. As

such measurements in magnetic resonance force microscopy are usually carried out at ultra-low temperatures and in ultra-high vacuum. The low temperatures also play another important role - they keep the spins in the sample coherent. While decreasing temperature certainly decreases thermomechanical noise, it still is the most severe road-block in the measurement of a single spin. This chapter examines design issues of cantilevers and reports the design and fabrication of a simple cantilever made of single crystal silicon. Some measurements of the frequency response of these cantilevers are presented. It is expected that the lessons learnt from the fabrication of these cantilevers and their testing will greatly help in further modifications to the design of the cantilever as well as in understanding the basic physics of magnetic resonance force microscopy and techniques to measure spins.

2.2 Previous Work

Previous work on the fabrication of silicon cantilevers for the purpose of MRFM is described in Stowe et. al.[15]. These cantilevers were fabricated using a similar process as described below. Further modifications of this work led to mass loaded cantilevers that were used to detect a single electron spin [16]. The cantilevers used in this experiment were fabricated using several process steps, including a crystal growth step for achieving mass loading.

2.3 Design Issues for MRFM Cantilevers

2.3.1 Material Selection

While there is no specific evidence yet that excludes the use of any particular material for the fabrication of cantilevers, there are three basic design considerations that must be taken into account: existing technology for fabrication, ease of fabrication given the material properties and the associated stiffness of the cantilever. While silicon-based fabrication obviously lends itself readily (based on decades-long development) for such processing, silicon based fabrication itself present many choices for the actual material for the cantilever – single crystal silicon, poly-silicon, silicon dioxide and silicon nitride to mention the most common. The fabrication process will have to accommodate easily the requirement of cantilevers without the presence of a substrate underneath the cantilever (unlike conventional MEMS processing). This requirement rules out the use of poly-silicon based processing (such as MUMPS and MOSIS) without introducing additional processing steps, which may not be compatible with these processes. Thus the two choices left are single crystal silicon and silicon nitride. Silicon nitride films have large residual stresses, thus the fabrication of these cantilevers will result in curled-up cantilevers. While this was not anticipated with low stress silicon nitride films, we found upon fabrication that even low-stress silicon nitride is not a

suitable material for the above reason. Gallium Arsenide - based cantilevers may be another suitable option as evidenced later in this manuscript. In this chapter only the silicon-based cantilevers are discussed.

2.3.2 *Geometry of Cantilever*

The geometry of the cantilever has great relevance in magnetic resonance force microscopy. Mozyrsky et. al. [17] have recently demonstrated theoretically that higher order modes of vibration of the cantilevers (due to intrinsic thermal noise) can cause spin relaxation rates in the sample to increase. Thus these higher modes will have to be damped. This can be accomplished by designing the cantilever in such a manner that the cantilever has greater mass toward the edge. The use of cantilevers with uneven cross sections to suppress spin relaxation is simulated in [18].

However, the above developments are fairly recent. When the silicon cantilevers were designed, this result was not known. Hence a triangular shape for the cantilevers was chosen based on one major consideration. For MRFM, the cantilevers will have to be brought very close to the sample, without touching the sample. A rectangular cantilever would have to be very thin (in terms of width) in order to reduce complications arising in the positioning of the cantilever to minimize tilt. The triangular shape is convenient in this regard. Another factor of consideration was the thermomechanical noise dependence of an equilateral triangular cantilever on its thickness. In such

cantilevers, the thermomechanical noise of the cantilever depends only on its thickness (for a given material). Thus the thickness of the cantilever can be varied arbitrarily (in practice is restricted to fabrication limitations) to suit thermomechanical noise requirements, while the other dimensions can be varied to suit frequency requirements. This appears to very convenient for calibrating MRFMs at various frequencies, while maintaining sensitivity.

Triangular cantilevers may have mode shapes at higher frequencies of thermal vibrations that contribute toward lowering relaxation times in spins. However, for purposes of establishing the basic functioning of MRFM technology, this shape was initially pursued in this dissertation. Also, the subsequent gluing of a magnetic particle to the tip of the cantilever can significantly damp higher order modes, thus meeting the ‘mass at tip’ requirement proposed in [17].

2.3.3 Position Detection

The mechanism used to detect the frequency shift of the cantilever can also play an important role in the design of the cantilever. In this dissertation three basic schemes are considered: optical detection using laser interferometry, capacitive detection using microwave resonator and integrated capacitive detection. The last scheme will be addressed in the following chapters, while this chapter will focus on the first two schemes.

Optical detection is an obvious method to employ for very sensitive detection since the position detection resolution of these methods approach 10^{-14} m. Thus, this method is readily suitable for employment in MRFM. Further, this method is fairly well established and many atomic force microscopes use optical detection for sensing cantilever displacement. The problems associated with using this method for MRFM are the effect of the laser power in decreasing relaxation times in the sample and the difficulty in aligning the lasers. The latter problem can be solved with some ingenious design of laser positioning methods and 'reflecting paddles' on the cantilever [15]. However, in semiconducting samples, the increased rates of relaxation are a serious problem associated with lasers. Thus a non-optical detection method is preferred, since the MRFM is expected to have widespread use in the semiconductor industry.

Scanning capacitive microscopy is another scanned probe technique that is seeing some renewed interest. This technique employs a capacitive sensing wire to sense displacement. This method can be used as a non-optical detection method. However, this method is not very useful for sensitive measurements, though it can prove invaluable in characterizing cantilever characteristics.

2.4 Design of Single Crystal Silicon Cantilever

The design of the single crystal silicon cantilever was done considering the above design issues. Resonant frequencies of the cantilever as well as the thermomechanical noise are calculated for a few thicknesses of equilateral, triangular cantilevers.

2.4.1 Assumed geometry

The assumed geometry of the cantilever is triangular. The geometry was assumed initially based on frequently used shapes for low-temperature, atomic force microscope cantilevers and requirements of frequencies in the megahertz regime. Thicknesses of cantilevers influence frequency more than shape (given the quadratic dependence of stiffness on thickness), thus a certain geometry

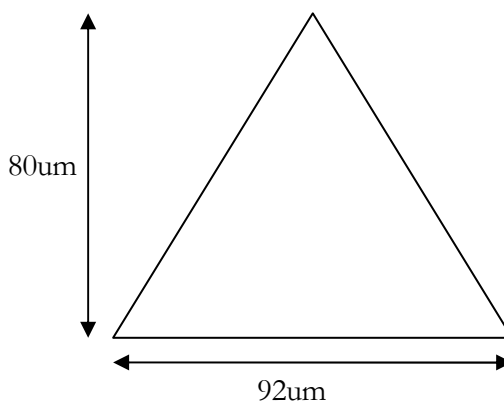


Figure 2.1 Geometry of single crystal silicon cantilever

was chosen and calculations for a few thicknesses are made. The shape chosen is a equilateral triangle of side 92 microns.

2.4.2 Resonant Frequency Calculations

The resonant frequency of an equilateral triangular cantilever is given by [19]

$$f_c = \frac{1.789t}{\Pi\sqrt{3}l^2} \sqrt{\frac{E}{\rho}} \quad (2.1)$$

Where f_c is the resonant frequency, t is the thickness of the cantilever beam a l is the height of the trianglular beam, E the young's modulus and ρ the density. For silicon, $E = 210$ GPa and $\rho = 2550$ kg/m³, thus giving resonant frequency for a thickness of 100nm to be 60 kHz.

2.4.3 Thermal Noise Calculations

The spectral density of force due to the thermomechanical noise of the equilateral, triangular cantilevers given by the equipartition theorem can be calculated using the below formula:

$$\sqrt{S_F} = \Delta F = \sqrt{\frac{k_b T}{\pi^2 Q f_c}} \quad (2.2)$$

Where k is the spring constant of the cantilever, k_b is the Boltzman's constant, Q the quality factor and f_c the resonant frequency. All measurements are made in ultra-high vacuum and at very low temperatures. Stowe et. al. [15] have achieved Q of greater than 100,000. Thus the Q is expected to be fairly high. Assuming a Q of 15,000, the table below shows thermomechanical noise

(at 300mK) of single crystal silicon, equilateral, triangular cantilevers of geometry described above at different thicknesses.

Thermomechanical noise of Silicon Cantilevers
for different thicknesses

Thickness (nm)	Thermomechanical Noise (N/ $\sqrt{\text{Hz}}$)
200	3.60×10^{-18}
100	1.80×10^{-18}
50	9.01×10^{-18}

Given that the required sensitivity at 300mK is of the order of an attonewton, cantilevers of thickness 100 nm will meet the needs of thermal noise sensitivity.

2.5 Fabrication of SCS Cantilevers

Fabrication of devices using existing MEMS technology is quite straightforward; however, the number and nature of devices that can be made out of single crystalline materials are quite limited. Most of current day commercial MEMS technology uses surface micromachining. While there are many commercial devices fabricated using bulk micromachining, most of these devices use a combination of both surface and bulk micromachining techniques.

In order to make cantilevers of single crystal silicon, silicon on insulator (SOI) wafers commonly used in the integrated circuit industry can be

employed. The specific type of wafer used is called a SIMOX wafer, which consists of an ion implanted buried oxide layer. These wafers have few flaws and if necessary very high quality material can be obtained. While such wafers have been used extensively in the integrated circuit industry, especially in almost all modern MOSFETs, the use of such wafers has been largely limited in MEMS because of their high cost.

The cross section of a SIMOX wafer consists of a handle or substrate of single crystal silicon and a device layer also of single crystal silicon separated by an oxide layer (BOX or buried oxide). Thicknesses of the device layer and buried oxide layer can be chosen from many available thickness combinations.

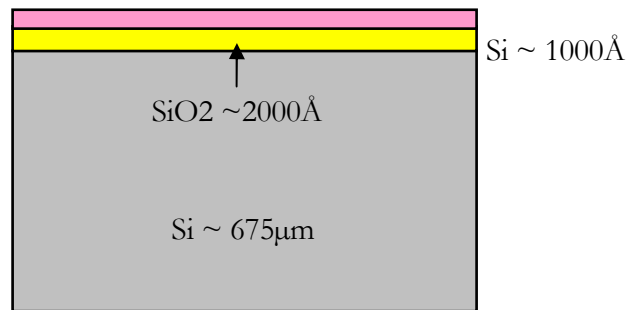


Figure 2.2 Cross section of a SIMOX wafer for fabrication of single crystal silicon cantilevers

For our particular device, it is desirable to have a 100 nm thick device layer and a sufficiently thick BOX layer (to serve as an etch stop). Initially we obtained SIMOX wafers of the cross section shown in Figure 2.2.

The proposed fabrication process is to etch the substrate from the bottom side of the wafer all the way to the oxide layer, and then to pattern the cantilever on the device layer to have cantilevers of required geometry. Note that the thickness of the device layer corresponds to the required cantilever thickness.

To etch down to the oxide layer, use of potassium hydroxide solution (40% KOH) at 80° C with constant agitation is employed. Calibration of etch rates at this temperature was done and set at 80 – 85 $\mu\text{m}/\text{minute}$. KOH etches silicon only along the (111) planes, thus the angle of etch would be approximately 54.74°. However, during the etch it is necessary to protect the thin device layer. Also a good mask is necessary for the etch. Standard photoresists do not offer protection against KOH at elevated temperatures. Hence it is decided to deposit a film of silicon nitride (Si_3N_4) on both the device and the substrate sides of the wafer. 1000 Å (or 100 nm) was chosen to be sufficient to act as a mask. It is necessary that the nitride layer be as free from defects as possible, since small pores can result in the completely etch of the thin device layer. The nitride thus serves as the mask for the KOH etch. Upon termination of the etch, the nitride and the oxide layer will have to be removed. Hydrofluoric acid (HF 49%) is highly selective to oxide and nitride and does not attack silicon. However, the etch rates of HF is 3 times quicker for silicon dioxide than for silicon nitride. Thus 2/3 rds of the nitride will be

etched away using a dry etch and then the wafer will be dipped in HF to remove the oxide and the nitride layers. Then, the silicon layer will be patterned using photolithography and cantilevers will be etched by another dry etch. The photoresists will be removed using organic solvents and critical point dried. The process is outlined in the following steps.

Step 1: Deposit a 100 nm thick layer of low stress silicon nitride (Si_3N_4) on either side of the wafer as shown in Figure 2.3.

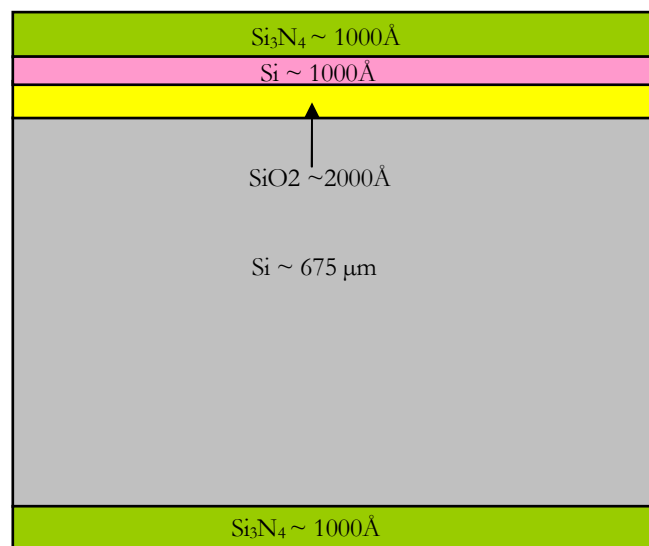


Figure 2.3 Step 1: Deposit 100 nm (1000 Å) thick Silicon Nitride on both sides of the wafer

Step 2: Membranes were patterned on the back side of the wafer using photolithography. SF_6 was used to etch away the nitride selectively to expose silicon only in the region to be etched. Then using KOH (45% at 80 C) the silicon was etched down to the oxide layer. The oxide layer is not an absolute

etch stop. However, KOH etches the oxide layer much slower than it etches silicon. Further it etches oxide isotropically without regard to crystalline planes. Hence an undercut can be observed if the oxide layer is etched further. This undercut helps in establishing if the etch has reached the oxide layer. The membranes thus formed have three layers, the device layer silicon sandwiched between silicon nitride and silicon dioxide, all 100 nm thick. The membranes are fairly delicate and extreme care was undertaken to ensure their integrity.

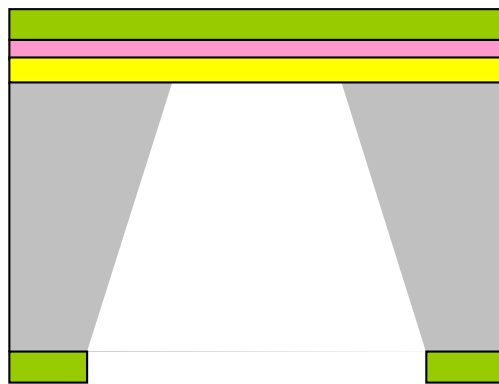


Figure 2.4 Step showing etched membrane

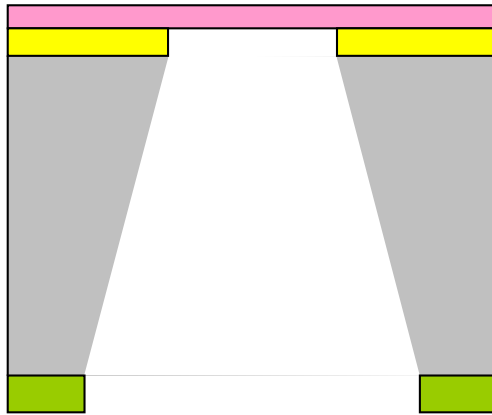


Figure 2.5 Step 3: Passivation removal

Step 3: The silicon nitride and the silicon dioxide have to be removed from the membrane. While concentrated hydrofluoric acid etches both SiO_2 and Si_3N_4 selectively with respect to silicon, it etches Si_3N_4 at a much slower rate than SiO_2 (recorded difference was 10 times longer for Si_3N_4). Hence it was necessary to remove most of the nitride prior to the HF dip. This was done using a dry etch, which removed about 950 \AA of silicon nitride. Then the membranes were dipped in HF for 2 minutes. A color change was seen from reddish to blue (due to the removal of the oxide, which is responsible for the reddish tinge). The result of this step is shown schematically in Figure 2.5 Step 3: Passivation removal. Also shown in Figure 2.6 is an optical picture of a membrane after the HF dip. The undercut can be seen as a border.

Step 4: Once the passivation was removed from the membranes the silicon of the device layer was patterned using photolithography. Since the membrane is translucent, alignment could be done using the contact aligner. Contact lithography was performed using low pressure vacuum contact to ensure that the delicate membrane is not damaged. The patterning is done using a positive photoresist. The particular resist used was OIR 908 HC 35. the thickness of the resist is estimated to be $4\mu\text{m}$. The exposure dosage was 160 mJ. An optical



Figure 2.6 Optical picture of a membrane showing undercut of oxide by HF. The undercut is seen as a border

picture of a patterned membrane is shown in Figure 2.7. the cantilevers are then released using a dry etch.

Step 5: Critical point drying is necessary for the cantilevers to survive surface tension forces of organic solvents used to remove the resists. The cantilevers

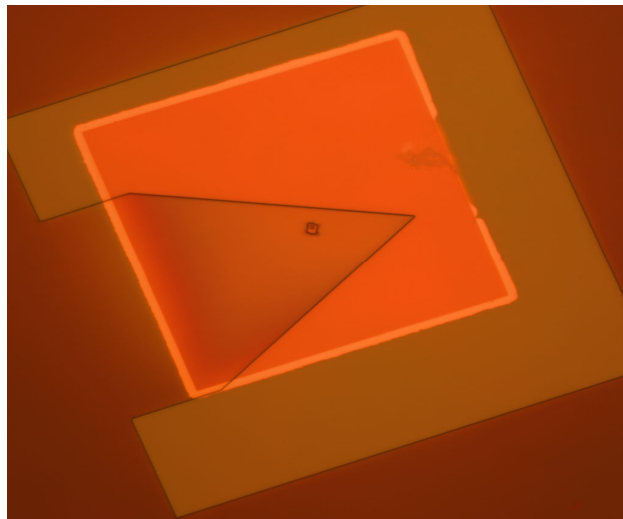


Figure 2.7 Picture of patterned membrane. The cantilver is patterned as a triangle using a positive resist

are transferred under methanol into a critical point dryer and drying is carried out. Critical point drying has been a low-yield process, primarily because of the damages caused by the handling of the chips with the free cantilevers. Current yields are estimated to be close to 80% after Step 4. The total yield for the process up to this stage is close to 60%.

Step 6: This is a step ubiquitous to the requirements of scanned probes, that requires cantilevers to be suspended of an edge, not in the center of a chip. This requirement is graphically represented in Figure 2.8. As such, this step

requires cleaving of the processed chip along a specific plane close to the edge.

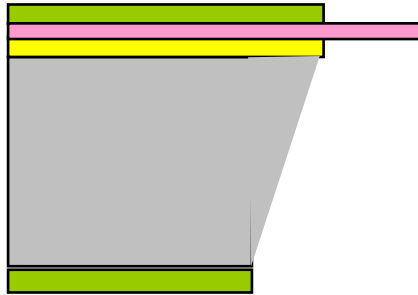


Figure 2.8 The requirement of 'cantilever on an edge' represented schematically

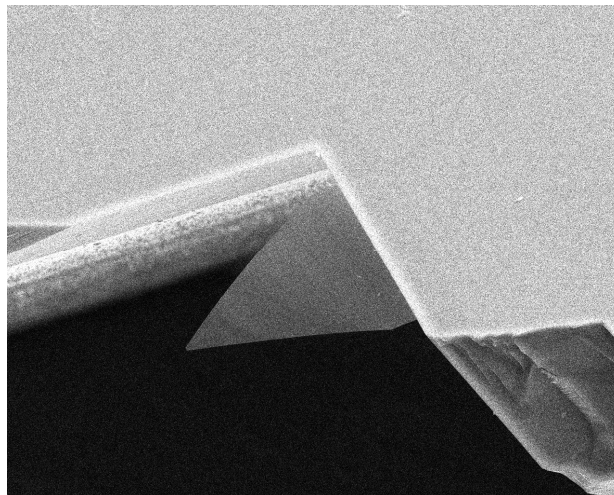


Figure 2.9 A failed attempt at scribing the chips in order to suspend the cantilever out on an edge

While standard wafer dicing operations lack the accuracy in order to cleave the chip within 100 μm , scribing is a process that one can envision to have better accuracy. Scribing requires that the scribe marks are made very straight along the planes (desired cleaving planes). This step requires careful

positioning of scribe and careful cleaving. Scribing requires fixing of the chip using a vacuum chuck. The vacuum chuck can destroy the fragile cantilever in these chips, hence the wafer was bonded onto an adhesive tape and this assembly was placed on the vacuum chuck. Scribe marks were made using a standard diamond scribe. Then, using a sharp diamond tip, the chip was cleaved along the scribe marks. However, this process being a mechanical process with high handling stresses, severely lowers yield. The final yield for the chips in the first attempt were 0%. A failed scribe attempt is shown in Figure 2.9. As seen from the SEM picture of the chip, even though the cantilever remained intact after the scribe attempt, the cleaving did not put the cantilever 'out-on-an-edge'. Hence this chip was not usable for MRFM experiments. Thus, even though cantilevers could be fabricated in the center of the chip reliably, the scribing required to suspend them on an edge greatly reduced yield.

2.6 The Scribing Dilemma

As mentioned in the previous section the scribing to suspend the cantilevers on an edge reduced yields to close to zero. Hence this problem was serious enough to consider a process change to ease scribing.

2.6.1 Polishing of wafer

SIMOX wafers have typical substrate thicknesses (for 6" wafers) of 610-710 μm . this thickness makes it extremely hard to cleave the wafer. Hence, it seemed like a possibility that the reduction in thickness would significantly ease the scribing process. The thickness of the wafer can be reduced by mechanical polishing known as lapping. For the substrate used, it was decided to use sandpaper lapping with constant water flow at 40 rpm. The sandpaper used was a Struer 1500 grit wet/dry. The lapping process would reduce thickness to about 150 μm .

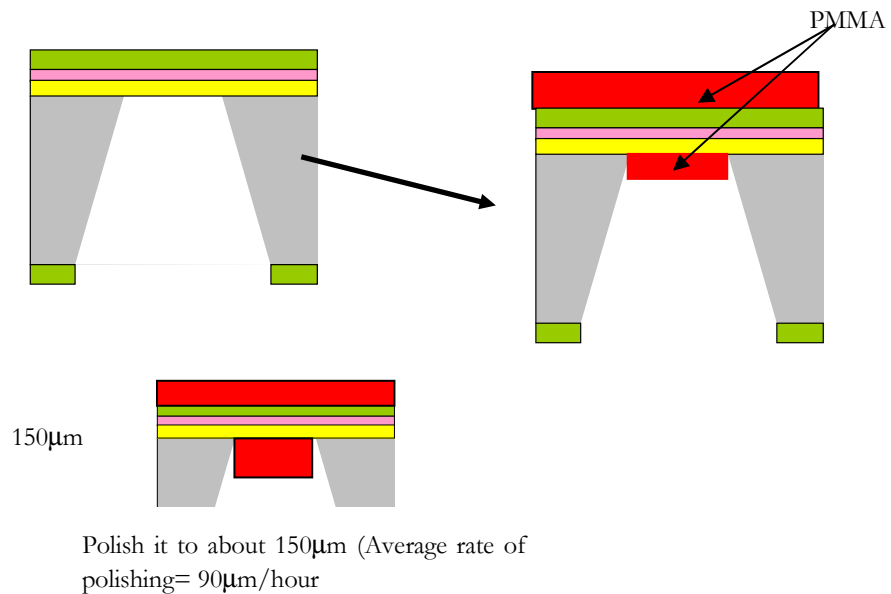


Figure 2.10 Schematic showing the steps of the lapping process

The lapping process being a mechanical process can result in the crystal planes being damaged. This may affect the KOH etch if done prior to the etch. hence it was decided to etch the membranes and then do the lapping process prior to the cantilever patterning and release. The process is shown schematically in Figure 2.10. However, after a few trials this process was abandoned since the few membranes that survived the process did not considerably ease the scribing process, since it was still difficult to align the cleaving of the chip exactly at the base of the cantilever. It is also suspected that the crystal damage due to lapping can contribute to uneven scribing.

2.6.2 *Long Membranes*

A desirable feature for initial testing of cantilevers is to have multiple cantilevers on one chip. This will be useful, since the set-up on the MRFM experiment is fairly time consuming and a broken cantilever otherwise would mean redoing the entire set-up. Taking into account these factors, it was decided to approach this problem differently. Instead of making small membranes with one cantilever on each membrane it was decided to make six cantilevers on a long membrane, three on each long side on the membrane. The anticipated advantages of this method are as follows:

- 1) More number of cantilevers per membrane

- 2) Scribing will result in straighter edges, because of the longer membranes. Further there is also the possibility to scribe them longitudinally

There are two points at which scribing can be attempted, one before the resist stripping and critical point drying (Step 5), or after the critical point drying. There are advantages to doing both as described below.

In the first case, the chips can be scribed prior to the critical point dry. This step has an advantage in that the dust accumulated during scribing will be taken off during resist stripping, thus giving a cleaner surface. However the disadvantage is that the cantilever, now suspended on an edge can come into direct contact with the sides of the drying chamber or with other chips and break.

In the second case, the scribing could be attempted after the critical point dry. This has the advantage that there are less chances of damage to the cantilever during the critical point dry; however, there is a high possibility of scribing dust attaching itself to the cantilever. We attempted scribing cantilevers post-dry, since this process seemed practical considering the cylindrical shape of the critical point dryer boat. Shows an SEM micrograph of a set of 6 cantilevers fabricated on a long membrane, three on each side of the membrane, staggered to accommodate all six. This process of using long membranes and scribing them resulted in yields close to 40%. This is a

definite improvement over the previous process. However, a more elegant solution to the scribing dilemma would be preferable.

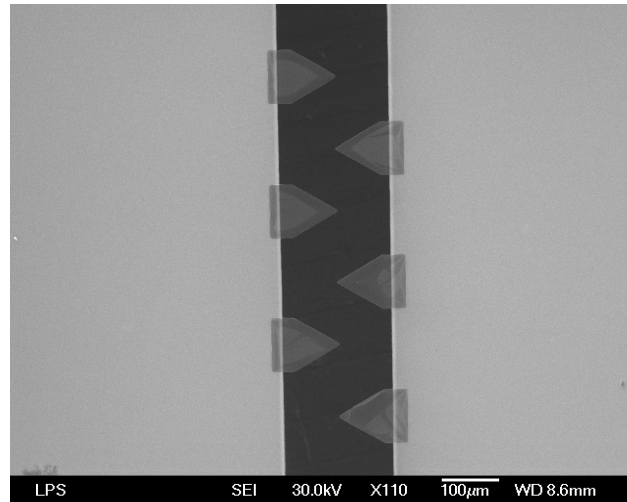


Figure 2.11 SEM image of a set of six cantilevers fabricated on a long (1.2mm) membrane

2.6.3 *Scribe Etch*

A scribe etch to ease scribing is a serious consideration, but this process comes attached with two specific limitations: the first is the process of using KOH to etch down to membranes is anisotropic with sidewalls sloped at an angle of 54° . While etching through thick substrates (typical substrate thicknesses for 6" wafers is 610-710 μm), large consumption of wafer real estate is a significant factor. Hence because of this angle of etch, the sidewalls may not be close enough to the membrane to get a good enough scribe. The second issue is the alignment of the scribe mark to coincide exactly with the edge of the membrane from which the cantilever will be suspended. While this

is not impossible, it is very difficult, since KOH etching depends on the crystalline planes and small imperfections in the crystal can easily result in an error of alignment in the final scribe mark by a few tens of microns. A combination of these two factors does not make the use of KOH to have chips with scribe marks a very viable one.

However, for scanning capacitive microscopy, as well as for optical detection, it is desirable to have sloped sidewalls, since the capacitive sensing wire as well as the optical fiber is brought down close to the cantilever. This is especially a problem for the capacitive sensing scheme, since straight sidewalls result in increased stray capacitance. A way to reduce stray capacitance is to lower the substrate thickness. This can be done either by polishing or by obtaining thinner wafers. Using thinner wafers and a combination and front and back reactive ion etching processes, one can hope to fabricate devices by incorporating scribe etches.

Hence, to incorporate scribe marks, the use of deep reactive ion etching (DRIE) to etch through the substrate was decided upon. The fabrication of such cantilevers was achieved through The MEMS and Nanotechnology Exchange and is described in 2.8.

2.7 Characterization of Cantilevers

The cantilevers fabricated using long membranes were characterized at room temperature using a capacitive probe at The Ohio State University¹. The work described in this section was not carried out solely by the author; rather it serves to identify the set-up in which the cantilevers were characterized. The set-up used was a vacuum bell jar and a microstrip resonator scheme as shown in Figure 2.12.

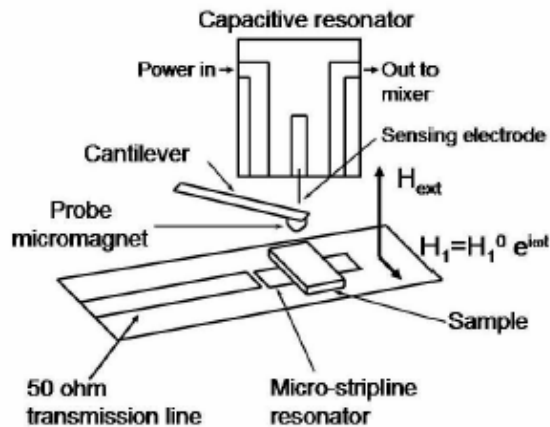


Figure 2.12 Set-up for scanning capacitive microscopy. The set-up shown also shows sample positioning and the magnetic fields as in an actual MRFM experiment. For characterization purposes, only sensing probe and cantilever without the sample and magnetic fields was employed. The cantilever was resonated using a piezoelectric resonator and the resulting resonance was sensed

¹ This work was carried out by Denis Pelekhov, Palash Banerjee, Camelia Selcu, Kin Chung Fong and P. Chris Hammel, Department of Physics, The Ohio State University

For testing, a cantilever was mounted on a piezo that was excited with a harmonic voltage of known amplitude V_{osc} and frequency. The resultant cantilever motion modulates the mixer output; this signal is detected with a lock-in amplifier [21] using the excitation signal as a reference. The frequency response of the cantilever oscillation is traced by sweeping the excitation signal through the mechanical resonance of the cantilever. Calibration of the cantilever response is based on the known displacement amplitude of the cantilever A_{res} at its resonant frequency, where

$$A_{\text{res}} = d_{33} V_{\text{osc}} Q$$

where $d_{33} = 4.8 \text{ \AA}/\text{V}$ is the coefficient of the EBL#6 piezoelectric material [22] used to excite the motion and Q is the measured cantilever quality factor.

Using this approach, detection of the displacement of various types of MRFM cantilevers has been demonstrated at room temperature. Fig. 3 shows the frequency response of a triangular cantilever. This cantilever was driven with piezo excitation amplitude of $4.8 \times 10^{-3} \text{ \AA}$. We find a readout sensitivity of approximately $5.0 \times 10^{-12} \text{ m}/\sqrt{\text{Hz}}$; in this case the overall detector noise level is dominated by displacement readout noise which corresponds to a force sensitivity of $80 \text{ aN}/\sqrt{\text{Hz}}$ [23].

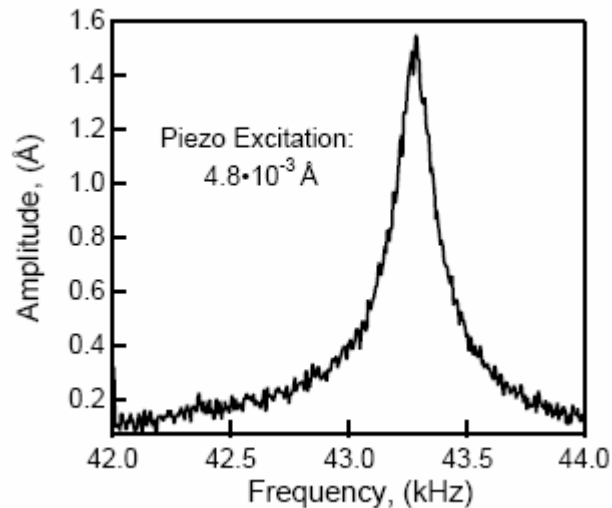


Figure 2.13 Capacitively detected response of a triangular cantilever. The signal was acquired at $T = 300$ K in vacuum

2.8 Fabrication of Cantilevers Using DRIE

As described previously, use of deep reactive ion etches (DRIE) with vertical or near-vertical side-walls would greatly ease the scribing process and increase yields significantly. To this end, a process using DRIE to fabricate single crystal silicon cantilevers was developed. This process is similar to the process described in 2.6, except that a DRIE step is incorporated instead of the KOH etch. Further, the DRIE step was performed as the last step of the process. Thus cantilevers were defined on the front-side of a SIMOX wafer with oxide on both sides. The wafer was then patterned using front-to-back alignment and photo-lithography on the back-side. A DRIE was performed to stop on the buried oxide layer (BOX) of the SIMOX wafer. The cantilevers

were now released in hydrofluoric acid (HF) followed by critical point drying. This HF-dip step also removed the oxide on top the cantilevers.

This process was performed by MEMS-Exchange using the process steps that were specified by me. The process resulted in high yields, with almost 95% of the cantilevers being useable. In order to have a variety of cantilever designs for MRFM experiments, these cantilevers were rectangular with two different widths and 4 different lengths.

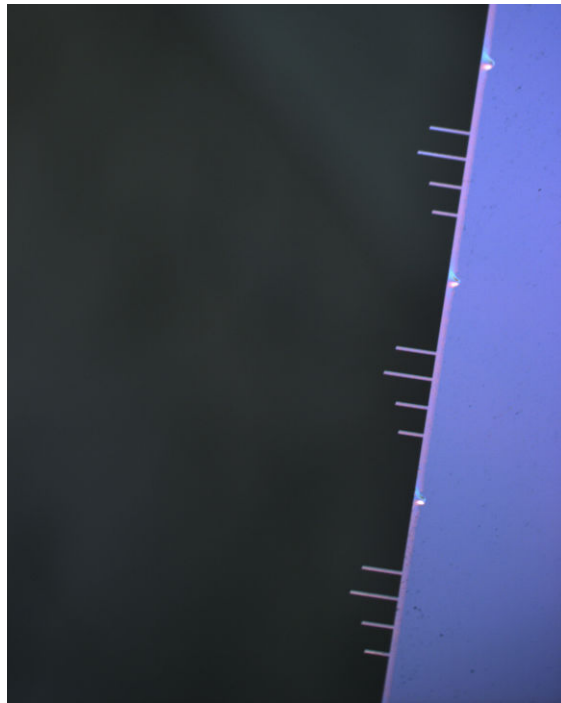


Figure 2.14 Figure showing cantilevers fabricated using DRIE. Four different lengths of cantilevers were fabricated.

2.9 A New Dicing-Saw Method for Cantilever Scribing

In order to make cantilevers quickly and reliably on an edge, another method using a combination of a dicing saw cut, front-side lithography and scribing is developed. This method is described as follows:

2.9.1 Step 1

In this step a scribe is made in the wafer using some technique such as sawing using a dicing saw. This cut is made in such a way that it is easy to scribe the wafer in future along this cut. This scribe is preferably made along defined crystal planes in the wafer so that it would preferentially cleave. It would be prudent to protect the front side of the wafer using photoresist that can later be removed. The wafer is cleaned thoroughly in solvents after the scribe is made.

2.9.2 Step 2

The scribed wafer is then patterned using a lithographic process (optical, e-beam etc.). The pattern is defined using back-to-front alignment such that the cantilever features are defined with the base of the cantilever close to the scribe mark. The cantilever features are then protected and etch to the sacrificial layer is made. This etch could either stop at the sacrificial layer or go beyond it.

2.9.3 *Step 3*

In this step the cantilever is released using some sacrificial etch. This step would suspend the cantilever over the substrate. Supercritical drying may be necessary for very thin cantilevers to prevent surface tension forces from damaging the cantilevers.

2.9.4 *Step 4*

This is the last step that suspends the cantilever on an edge. In this step the wafer is broken along the previously made scribe mark, which would result in accomplishing the scribe. This step could be done in liquid, (before the supercritical dry in step 3, for instance) to protect delicate cantilevers from flying particles (which is typical while breaking wafers).

The process flow is shown in Figure 2.15. A patent has been filed for this process [24].

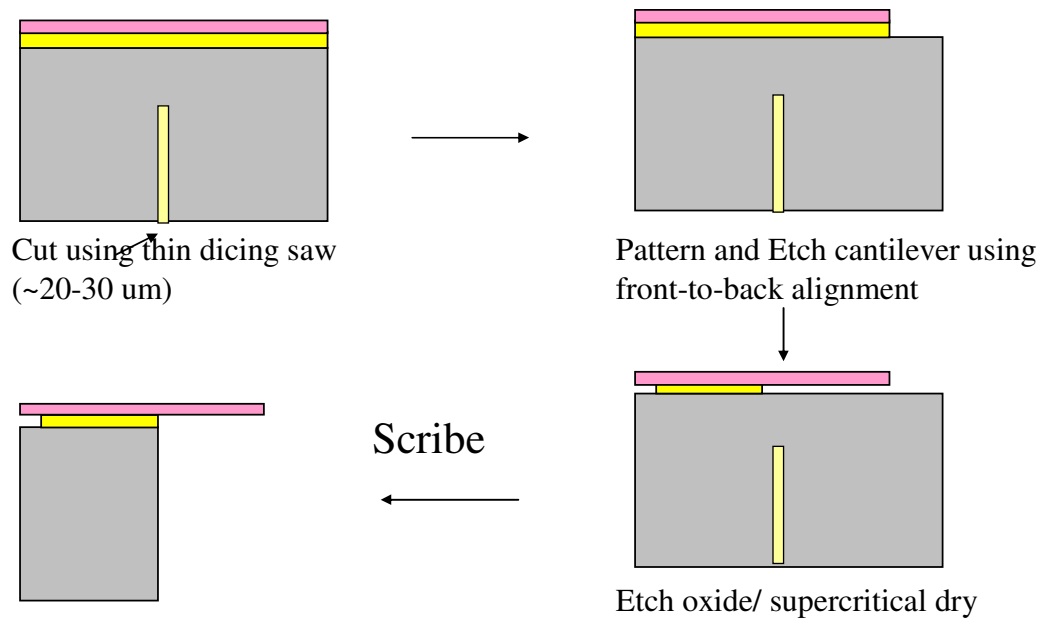


Figure 2.15 Edge Suspension of a cantilever using a dicing saw process

2.10 Limitations of Current Measurements Schemes

The fabrication of single crystal silicon cantilevers is extremely important for studying the physics of magnetic resonance and for the development of MRFM. Current state-of-the-art position detection techniques for ultra-sensitive applications utilize optical detection schemes. The limitation of this approach is that light induces excitations in semiconducting samples, lowering relaxation times by orders of magnitude. Further, as cantilevers become smaller, optical detection becomes greatly complicated at low temperatures owing to difficulty in alignment of the laser beam on the cantilever. For high-precision detection lasers must be operated at high power. However, this

would increase the cantilever temperature. This is a significant problem for very thin cantilevers, since thermal conduction reduces with decreasing cross-sectional area. Thus there is a non-optimum trade-off between sensitivity and laser power, as the feature sizes of the cantilevers decrease.

The alignment problem persists even for non-optical detection using the technique as described in 2.7. This capacitively scheme is a novel approach toward a lightless detection procedure. However, it is expected that these probes may not ultimately have sufficient position detection sensitivity to detect nuclear spins. Further, alignment of the microwave resonator (wire in this experiment) is still required, which is very difficult, and poses similar problems as the optical scheme, as feature sizes decrease. **Thus, an integrated approach to position detection as compared to using external position detection probes must be developed. The development of such a technique as well as its fabrication and measurement are the focus of the rest of this dissertation.**

Chapter 3

DESIGN FOR ULTRASENSITIVE CAPACITIVE DETECTION

3.1 Introduction

As mentioned at the conclusion of the previous chapter, a position detection scheme that incorporates an all electronic detector would be ideal. In addition to the obvious advantages of having a ‘plug-and-play’ capability, such a scheme would possibly be superior to existing position detection schemes for the simple reason that alignment of the laser on the beam is not necessary. Further, high power lasers can significantly heat up the cantilever, thus increasing thermal noise. Thus a sensitive all-electronic read-out of cantilevers for MRFM is necessary. The development of such a scheme is the focus of this chapter.

3.2 Literature Review

A literature review of existing schemes for electronic position detection schemes for ultrasensitive applications reveals the use of piezoelectric properties of materials. Among the most sensitive schemes that have been demonstrated is the piezoelectric scheme using GaAs/ AlGaAs cantilevers coupled to high electron mobility transistors [25]. They have achieved a displacement detection of $0.002\text{\AA}/\sqrt{\text{Hz}}$ that corresponds to a force detection

noise of $1\text{pN}/\sqrt{\text{Hz}}$ at a temperature of 4.2K . These cantilevers use the piezoelectric effect intrinsic of these heterostructures and couple them to a GaAs field effect transistor (FET). The strain in the cantilevers modulates the gate voltage of the FET, which can then be read out.

GaAs/ AlGaAs FETs are a good choice as on-chip amplifiers for two reasons: -

1. They can be custom fabricated to meet a wide variety of needs, while still maintaining higher switching speeds (compared to MOSFETS in silicon-based materials).
2. They do not freeze out at ultra-low temperatures, thus making them operable at low temperatures.

Given these inherent characteristics of HEMTs/ GaAs FETs and existing technologies to grow wafers with custom epi-layers, the use of GaAs/ AlGaAs heterostructures to make nanoelectromechanical systems (NEMS) is highly favorable.

Another very common method employed in force detection in microelectromechanical systems (MEMS) is capacitive sensing. Capacitive sensing is among the most common sensing mechanisms in MEMS. Quite frequently, these sensing schemes use comb-drive sensing mechanisms to mitigate to an extent the high damping forces of squeezed film that can lower the quality factor Q dramatically. (for example the actuator described in [26])

Some applications that do not require operations at moderate to high frequencies do use parallel plate capacitive sensing schemes, though these are rare. Among the factors that make capacitive sensing schemes impractical for sensitive sensing schemes is the signal division by parasitic capacitance of connections and cables. The parasitic capacitance in many cases is the determining factor that restricts the use of capacitive sensing schemes for ultra-sensitive applications. For capacitive sensing schemes to be adopted more widely in ultrasensitive applications, mitigation of effects due to parasitic capacitance is necessary.

Current state of the art in position detection includes the cantilevers used in Rugar's experiment [16]. These cantilevers have a fundamental resonance frequency of 5.5 kHz and thermomechanical noise of about 0.5 aN. Optical interferometry is used to detect position of these cantilevers. Another experiment that has gained widespread attention is the Lahaye experiment [5]. In these experiments a doubly clamped beam (with resonant frequency of 20 MHz) is coupled to the gate of a single electron transistor (SET). SETs are nearly ideal amplifiers, limited only by the quantum limit. Using such a set-up, this experiment has a position detection sensitivity of 1 aN and is a factor of only 4.5 away from the quantum limit (imposed by the Heisenberg Uncertainty Principle). A further improvement to this experiment is described in [6], where Naik, Buu et. al. have shown 0.5 aN force sensitivity and are a

factor of only 2 away from the uncertainty limit. These are the most sensitive measurements of position detection thus far.

3.3 Proposed Force Sensor

As mentioned in the previous section, there is a need to develop a light-free, ultra-sensitive sensing mechanism to sense cantilever motion. MEMS-based force sensors have often used many integrated sensing schemes such a

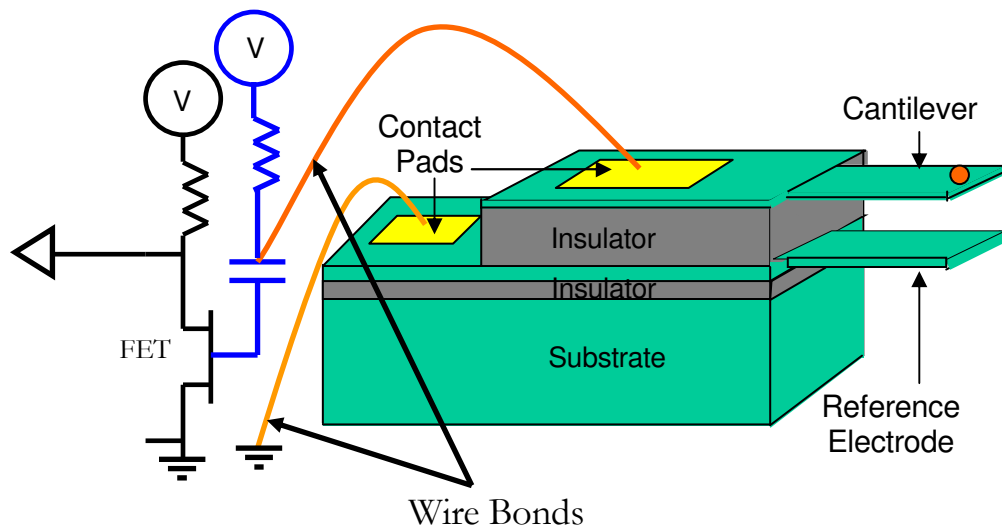


Figure 3.1 Proposed Force Sensor. The bond pads contribute to parasitic capacitance, thus dividing away signal from the capacitive sensing scheme. Integration of FET onto the same chip as the cantilever will reduce parasitic capacitance

piezo-electric, piezoresistive and capacitive detection. While these schemes have merits and demerits, almost all of them are used for applications where the required sensitivity is several orders of magnitude less than that required for MRFM. The thermomechanical noise of a beam is one of the limiting factors in the design of ultra-sensitive force sensors. The other limiting factor is the position detection sensitivity. The highest sensitivity achieved by non-optical sensing schemes is by Beck et. al [25], where they demonstrate a force sensitivity of $\sim 10^{-12} \text{ N}/\sqrt{\text{Hz}}$ at 4K using the piezoelectric effect. In this section we present a capacitive sensing scheme coupled to an on-chip transistor that serves as an amplifier.

This scheme utilizes a GaAs/AlGaAs heterostructure with integrated mechanical and electronic layers. Heavily doped GaAs form two plates of a parallel plate capacitor coupled to an on-chip, very low gate capacitance, high electron mobility transistor or HEMT as shown in Figure 3.1 and Figure 3.2. The choice of using a GaAs/AlGaAs heterostructure is made based on established procedures for low gate-capacitance HEMTs and the ease of growth of custom epi-layers.

For the upper cantilever of GaAs, a 195 kHz resonator for a 10 μm long and 30 nm thick cantilever with a spring constant of 1.73mN/m is expected. The gap between the two plates is 3 μm . The width of the cantilever is chosen to be 3 μm . The lower cantilever is thicker so that it will have a higher

resonance frequency, acting as a reference at the resonant frequency of the thinner cantilever. One plate of the capacitive scheme is grounded, while the other serves as the gate for a GaAs Field Effect Transistor (GaAs FET). Integration of the FET to function as an ‘on-chip’ amplifier would reduce parasitic capacitance that would otherwise divide away the signal from the capacitive scheme.

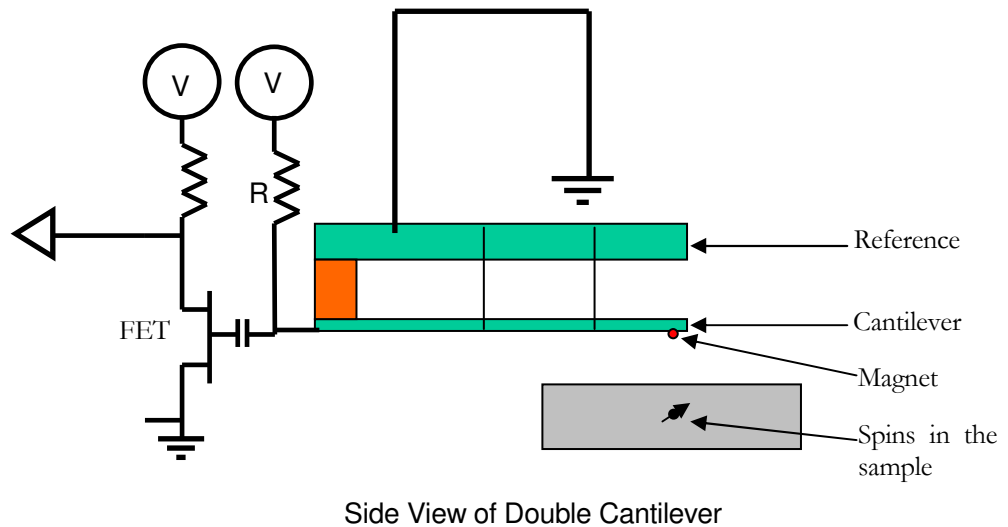


Figure 3.2 Cross-sectional view of proposed capacitive detection scheme. The glued magnet will be shaped using focused ion milling techniques

Mar et. al. [27] have achieved a bandwidth of 1 MHz with an input gate capacitance of 0.15pF – 0.3pF, for a GaAs FET structure at $1 \text{ nV.Hz}^{-1/2}$. Power dissipated in FET was 7 mW. In this dissertation, it is anticipated that such FETs can be emulated for integration into the capacitive scheme described above. The capacitance between the upper and lower triangle should be $\sim 32\text{fF}$ matching well to the input capacitance of the FET (15fF) described

in [27]. The maximum DC voltage we can apply between the two cantilevers for biasing should be about 10 V. This is calculated by simple snap-in considerations (when cantilever moves by 1/3 of the gap).

3.4 Force Sensitivity Estimations

A set of calculations to arrive at the proposed force sensitivity of the capacitive scheme is presented in this section. The frequency of the cantilevers for the above geometry is 195 kHz. The pull-in voltage for the capacitive plates is calculated to be 10 V. This determines the limit of the bias voltage that can be applied between the capacitive plates. Given that many commercial amplifiers have a voltage spectral density resolution of $\sqrt{S_v} \sim 1\text{nV}/\sqrt{\text{Hz}}$, and assuming a bias voltage lower than the pull-in voltage, the spectral density of displacement can be calculated as

$$\sqrt{S_d} = \frac{C_{\text{Total}} \cdot d}{C_{\text{Cant}} \cdot V_{\text{Bias}}} \cdot \sqrt{S_v} \quad (3.1)$$

Where C_{Total} , C_{Cant} , d and V_{Bias} are the total capacitance (including stray capacitance that does not contribute to position detection), the capacitance between the cantilevers, the distance between the parallel plates and the applied bias voltage. Assuming large parasitic capacitances (of bond pads that 220 mm square and wire bond capacitances of 0.1pF) $\sqrt{S_d}$ is calculated to be

$\sim 10^{-11}$ m/Hz^{1/2} for our design. Using this value, one can calculate the expected force sensitivity in terms of spectral density as follows: -

$$\sqrt{S_F} = \frac{k}{Q} \cdot \sqrt{S_d} \quad (3.2)$$

Since measurements are done in ultra-high vacuum at low temperature (300mK), we expect the quality factor (Q) to be fairly high. Assuming the Q to be 10,000 (Q of 200,000 have been achieved [7]), the expected position detection sensitivity is $\sim 10^{-18}$ N/Hz^{1/2} – close to that necessary for single electron spin detection. Lowering the parasitic capacitance to 50 fF by integrating the FET onto the same chip, one can expect the sensitivity of position detection to be $\sim 10^{-14}$ m/Hz^{1/2}. This would correspond to a force sensitivity (of measurement scheme, excluding thermal noise) of 10^{-23} N/Hz^{1/2}, sufficient to detect single nuclear spins. These estimates illustrate the potential of this relatively simple scheme for high-precision force measurement.

Another important consideration is the thermomechanical noise of the resonator. The spectral density of force at resonance due to the thermomechanical noise of the equilateral, triangular cantilevers given by the equipartition theorem can be as:

$$\sqrt{S_F} = \Delta F = \sqrt{\frac{k \cdot k_b T}{\pi^2 Q f_c}} \quad (3.3)$$

Where k is the spring constant, k_b is the Boltzmann Constant, Q is the quality factor and f_c is the resonant frequency of the cantilever.

For the scheme proposed the spectral density of force of the thermomechanical noise is expected to be $\sim 10^{-19}$ N/ $\sqrt{\text{Hz}}$ at a temperature of 300mK. Thus, at this temperature the thermomechanical noise is expected to limit sensitivity.

Detailed estimates of force sensitivity are made in the following sections. These estimates reveal the challenges associated with the fabrication and experimentation associated with ultra-high sensitivity force detection using all electronic read-out. Further the discussion may shed light on alternate techniques that may be possible using capacitive coupling.

3.5 Circuit Model for Capacitive Detection

Noise estimates for detection of capacitively coupled nanomechanical resonators can be made once a model for detection is built. The circuit model for capacitive detection of cantilevers can be built on generic models that can express mechanical elements as equivalent electrical components in a circuit. This greatly eases estimation of the parameters of detection, including noise and parasitic capacitance effects. As noted on the previous section, excessive parasitic capacitance can severely limit sensitivity of the measurement scheme. Thus it is important to estimate its value in advance.

A mechanical element with a sense electrode for capacitive detection can be represented in a circuit as a variable capacitor. Once biased with a large DC

source (large such that it is practically constant as compared to the time constant of the resonator), this changing capacitor functions as an AC source in the circuit with a frequency corresponding to that of mechanical motion. This is the basis for capacitive detection in MEMS devices.

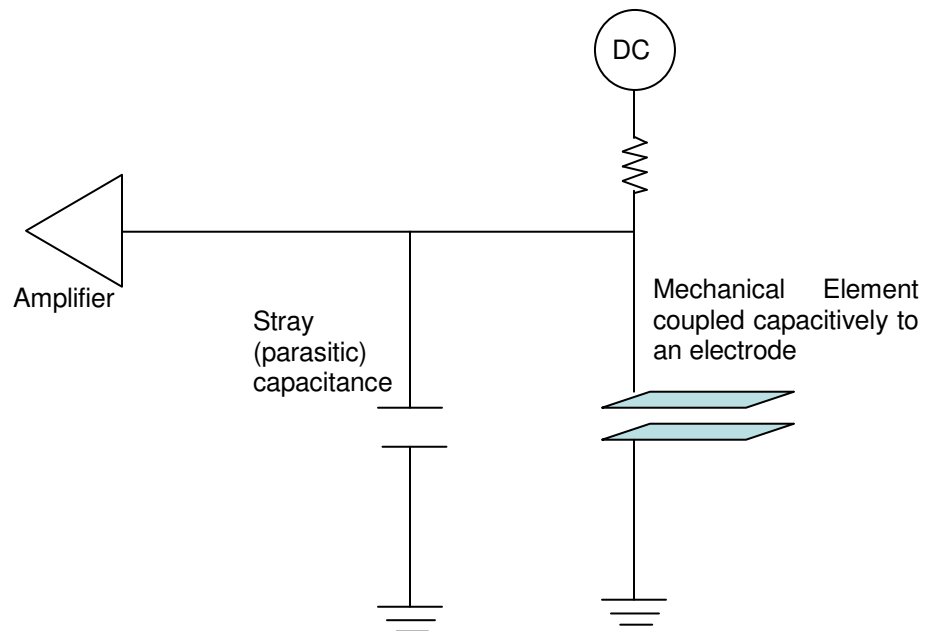


Figure 3.3 Representation of a mechanical element (moving) coupled to a sensing electrode for capacitive sensing.

Reflectometry measurements are very common for capacitive sensing. However, reflectometry methods typically require very well matched impedances. The formalism to express mechanical motion for capacitive detection is well known [28] and is described in Appendix A. It is shown that a

moving mechanical element that is capacitively coupled is equivalent to a RLC circuit, with the equivalent R, L and C components given by:

$$\begin{aligned}
 L_m &= \frac{d^2 m}{V_{\text{Bias}}^2 C_{\text{Cant}}^2} \\
 C_m &= \frac{V_{\text{Bias}}^2 C_{\text{Cant}}^2}{\omega_0^2 d^2 m} \\
 R_m &= \frac{d^2 m}{V_{\text{Bias}}^2 C_{\text{Cant}}^2} \frac{\omega_0}{Q}
 \end{aligned}
 \tag{3.4}$$

Thus the mechanical motion can be completely modeled by an equivalent RLC circuit with circuit values shown in Equation 3.11. At mechanical resonance (analogous to the RLC circuit resonance), the inductive and capacitive parts of the circuit are equal in magnitude and opposite in sign, thus canceling each other. The impedance thus drops dramatically at resonance and is equal to R_m . This result will be useful in future discussions pertaining to the impedance of the circuit and impedance matching techniques.

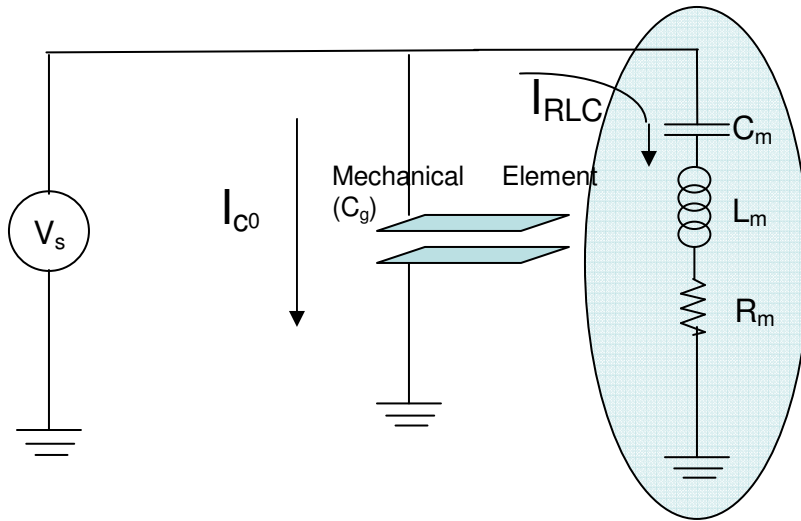


Figure 3.4 The equivalent circuit of a voltage biased nanomechanical resonator and gate device. I_{CO} is the current through gate capacitance, and I_{RLC} is the current through the resonant circuit.

3.6 Impedance Transformation using Tank Circuits

The section above is important in order to estimate the AC electrical impedance of a cantilever that is being capacitively coupled to a sense electrode. Clearly, the impedance drops dramatically at mechanical resonance of the cantilever. This is due to the inductive and capacitive parts of the equivalent RLC configuration canceling each other. Thus, the impedance that is seen by an amplifier is equal to the resistance of such an equivalent circuit.

This lends some insight into possible measurement techniques for capacitive detection. Since measurements are carried out in a cryostat, long cables are required to carry signals to and from the cantilevers. Clearly, high impedances cannot be measured outside the probe directly, because of the substantially large cable capacitances, which would divide the signal. Thus

impedance matching techniques are necessary in order to transform these mechanical impedances.

Impedance matching can be carried out in many ways and these can be explored in many standard texts on the subject, for instance [28] and [30]. The two techniques that I shall discuss in this dissertation are transformation using a transistor inside the cryostat and a tank circuit.

In order to understand the impedance matching techniques, estimation of the impedance of the cantilever at resonant frequency is necessary. For the geometry of the cantilever discussed in Section 3.3, and from equation 3.11 we can estimate impedance of the mechanical elements at resonance to be give by

$$R_m = \frac{d^2 m}{V_{\text{Bias}}^2 C_{\text{Cant}}^2} \frac{\omega_0}{Q} \quad (3.5)$$

Assuming $Q = 15000$, the impedance at resonance will be $1.37 \text{ M}\Omega$.

To transform an impedance of $1.37 \text{ M}\Omega$ to close to 50Ω , which is a typical value for standard coaxial cables and inputs of most amplifiers, a tank circuit can be used. However, the impedance (given by Equation 3.11) requires very accurate determination of the frequency, which typically is not known before measurement. Thus, alternate means to find the frequency of the cantilevers prior to measurement is necessary. Essentially, impedance transformation is a narrow-band detection technique. Given the high expected Q of the resonators, this is a severe disadvantage of this technique. However, this technique offers one other very attractive benefit. In order to explore this, let us consider a

typical tank circuit used for impedance transformation shown in Figure 3.5. The tank circuit essentially transforms an impedance Z to a value close to that of the input of the amplifier. The value of the tank circuit impedance can be estimated from which both L_{Tank} and C_{Tank} necessary for impedance transformation can be derived as follows, assuming amplifier input is 50Ω .

$$\begin{aligned}
 Z_{\text{Tank}} &= \sqrt{R_m \times 50} \\
 L_{\text{Tank}} &= \frac{Z_{\text{TANK}}^2}{\omega} \\
 C_{\text{Tank}} &= \frac{L_{\text{TANK}}}{Z_{\text{TANK}}^2}
 \end{aligned}
 \tag{3.6}$$

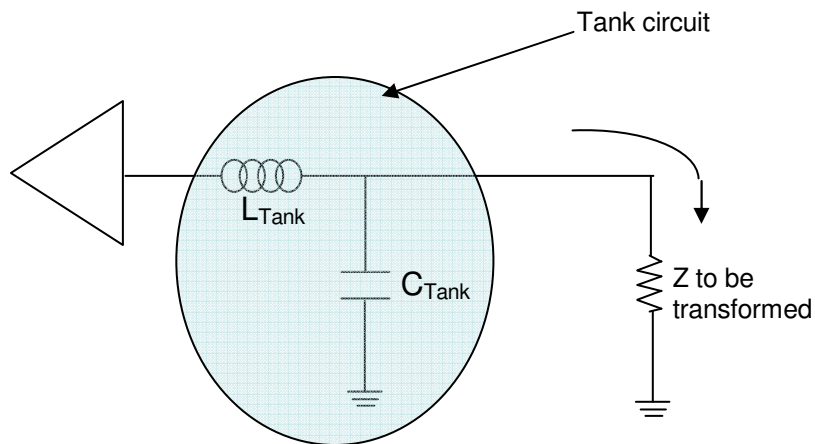


Figure 3.5 Tank circuit for transformation of an impedance Z . Note the two components of the tank circuit, the capacitance and the inductance

For the geometry under consideration, the impedance of the tank circuit is $1.65 \text{ k}\Omega$. Thus the value of the inductance L_{Tank} and the corresponding value of the capacitance C_{Tank} can be 0.05 H and 18 nF respectively. The desired Q for the tank circuit is given by

$$Q = \frac{R_m}{L_{\text{Tank}} \cdot \omega_0} \quad (3.17)$$

For this particular set of conditions, it can be shown to be 23.

One of the interesting and beneficial aspects of using a tank circuit for impedance transformation is that the parasitic capacitance of bond pads, wire bonds etc. can be used as part of the tank circuit. Thus the C_{Tank} in Figure 3.5 can be the parasitic capacitance. Thus as long as the value of the parasitic capacitance is reasonable, it is possible to completely null the effect of the parasites by making it a part of the tank circuit. This can be very useful for sensitive measurements especially for MRFM.

One of the concerns of using this technique is that amplifiers with suitable input impedances but with low noise temperatures are very difficult to obtain and use easily. This topic will be covered in Section 7.2.

3.7 Impedance Transformation Using FETs

The previous section dealt with the method of transforming the impedance to match that of the input of an amplifier some distance away, assuming that the amplifier input impedance was lower than that of the capacitive cantilevers. However, an alternative is to have an amplifier close to the cantilever system. Such an amplifier can have very high input impedance, ideally an open input, but the output impedance is close to that of the lines (the lines are 50 Ω , typically). This technique has the advantage that since parasitic

capacitance can be limited (owing to the proximity of the FET to the cantilever system), one can effectively measure the cantilevers with a larger bandwidth; thus the exact frequency of the cantilevers can be obtained by the same method. An ideal implementation would be to realize both the cantilever system and the FETs on the same chip. This would greatly reduce parasitic capacitance, in addition to being conducive for convenient measurements.

The parasitic capacitance for this type of measurement is important. In the first generation of devices, it is anticipated that the two components, namely the cantilever system and the FETs will be realized on separate chips. Thus bond pads are required for the cantilever system. The bond pads increase the area of the total capacitance with respect to that of the capacitance that is varying (in Equation 3.1). Clearly this would decrease the sensitivity of the measurement. Assuming square bond pads of side $220\ \mu\text{m}$ for an initial design, the parasitic capacitance is $1.76\ \text{pF}$. The parasitic capacitance is also influenced by the wire bond itself (typically $0.1\ \text{pF}$) as well as the input capacitance of the FET. Commercial FETs have input impedances of $1\ \text{pF}$ or higher. It is possible to make FETs with low capacitance as mentioned in Section 3.4. Considering an FET with an input capacitance of $32\ \text{fF}$, the value of the total parasitic capacitance is $\sim 2\ \text{pF}$. Thus from Equation 3.1, the sensitivity of the position detection scheme can be estimated to be 75.3

aN/ $\sqrt{\text{Hz}}$. Thus the parasitic capacitance in this case limits the sensitivity of the measurement scheme.

If the components are integrated together, assuming that the lines from the cantilever system to the FET on the chip is 20 μm long and 3 μm wide, and since there will be no bond wires, the sensitivity increases to ~ 1 aN/ $\sqrt{\text{Hz}}$. Thus clearly this measurement scheme has the potential for

1. Integrated detection when FETs are integrated on to the same chip as the cantilever system
2. Broadband detection of the cantilevers, thus not requiring that Q and frequency be known prior to detection

However, this scheme poses several challenges, including the fabrication of FETs for use at low temperatures, and integration of the FETs into the same chip as the double cantilevers, especially since the fabrication of ultrathin cantilevers is in itself a challenge.

In the following chapters, the process development for fabrication of ultrathin cantilevers in a double cantilever configuration is described. Design, fabrication and characterization of GaAs FETs for use as low temperature amplifiers is presented. A chapter on measurement techniques used for initial characterization of the cantilevers coupled to the FETs is presented prior to the conclusion.

Chapter 4

FABRICATION OF ULTRA-THIN ‘DOUBLE’ CANTILEVER

4.1 Introduction

In the previous chapter, a design for ultra sensitive measurement using an integrated sense electrode in a double cantilever configuration was presented. The dimensions of the cantilever used as the resonator is described in the previous chapter. It is noted that the thickness of the cantilever resonator is only 30nm. At the time this dissertation was commenced there were no reports of the realization of 30nm thin cantilevers. This chapter describes the process development for fabrication of ultra-thin cantilevers in a double cantilever configuration.

4.2 Fabrication Sequence

To fabricate the double cantilevers, an ideal sequence would be to obtain wafers with the two structural layers (the 30 nm resonator layer and the thicker sense or reference electrode layer). The two structural layers must also be conducting. Since the FETs for low temperature applications are typically in GaAs heterostructures, and ideally the structural layers would be integrated with the FETs on a single ship, it is much simpler to have the structural layers in GaAs/ AlGaAs heterostructures, as described in Chapter 3. Since wafers

with the desired thicknesses are not available readily, they have to be custom-grown.

Custom grown wafers are obtained with required layer compositions and thicknesses. These wafers were grown at the Laboratory for Physical Sciences by Molecular Beam Epitaxy (MBE) [32]. For the design described in the previous chapter, this would require 2 conducting layers of GaAs separated by a dielectric, sacrificial layer that is 3 μm thick. The dielectric that can be conveniently grown with GaAs is AlGaAs. The amount of aluminum in AlGaAs determines the selectivity of the sacrificial etch, typically hydrofluoric acid (HF). HF typically etches AlGaAs when the aluminum content is 55% or more. We chose $\text{Al}_{0.7}\text{Ga}_{0.3}\text{As}$ as the dielectric material based on experimental observations of etching rates. The etching rate in 49% HF is estimated to be 10 $\mu\text{m}/\text{minute}$.

The proposed fabrication sequence to make double cantilevers is as shown in Figure 4.1. In the first step a mesa is defined using standard photolithography and etched down to the reference cantilever layer. This is done in two parts. In the first part, a plasma etch using Cl_2/BCl_3 at 5 mT pressure and RF power of 70 mW is carried out to etch $\sim 2.5 \mu\text{m}$. In order to remove any trace of AlGaAs, the wafer is now dipped in 49% HF for 10 seconds. The depth of etch is noted and the HF dip is performed until the etch depth does not change. This is done to ensure that all the AlGaAs is etched and the lower

GaAs layer is exposed. This step provides access for subsequent bond-pad definitions on both these layers, necessary to make electrical contact for measurements.

The bond pads are then defined using standard photolithography. Since the bond pads are to be defined on highly doped layers (n-type silicon dopants $> 10^{18}/\text{cm}^2$), ohmic contacts are not necessary. Thus standard Ti-Au contacts were evaporated for bond pads to make electrical contact to both the structural GaAs layers. The resistance of such contacts was evaluated to be 3.5 k Ω at room temperature and 15 k Ω at 4.2 K. This is an acceptable resistance, since as shown in the previous chapter, the mechanical resistance of the capacitive cantilever appears to be $> 1 \text{ M}\Omega$ – thus an additional 15 k Ω is not significant.

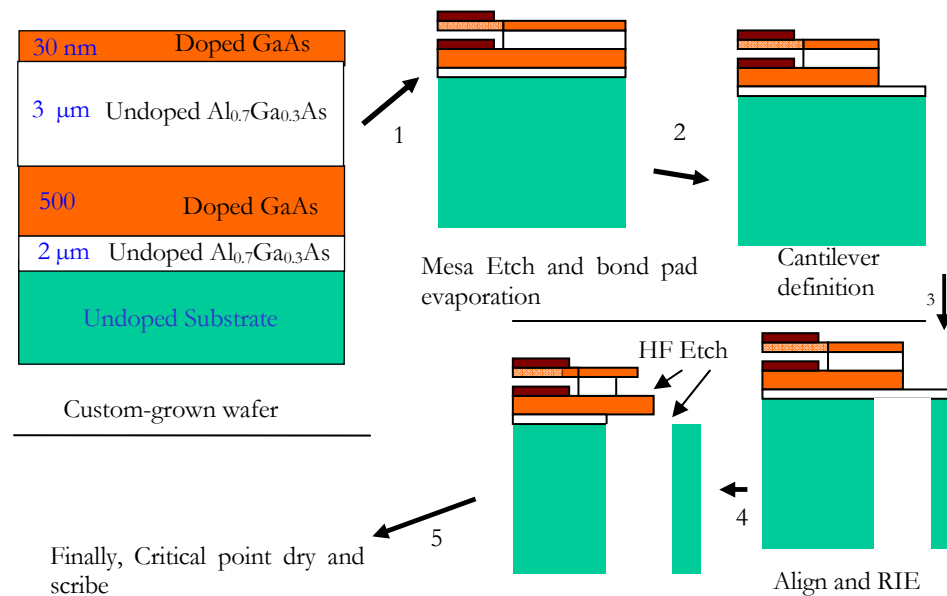


Figure 4.1 Fabrication sequence for double cantilever layer. The topmost layer (30 nm thick GaAs) is the resonator layer. The third layer (500 nm GaAs) is the reference cantilever

In the second step, the cantilever is patterned using standard photolithography. In this step both the bond pads are also protected from the subsequent etch. The cantilever is defined at the end of a long arm. This is to accommodate eventual use of this scheme on magnetic resonance force microscopes, which requires cantilevers close to the sample. Thus a short cantilever on the edge of a wide wafer would make the scanning very tedious. In this process, the cantilever is defined and etching is done all the way into the lower AlGaAs layer.

In the third step, the wafer is inverted after protecting the top of the wafer with a polymer (such as a photoresist). The backside of the wafer is aligned to the front side using infra-red alignment and the backside is to be patterned using photolithography. While deep etches through silicon substrates are very well controlled and processes for such etches are widely available, carrying out such a process for GaAs is not trivial. One of the major hurdles in overcoming this step is to have a mask that can withstand a long etch in an inductively coupled plasma (ICP) reactive ion etch (RIE) using Cl_2 and BCl_3 . Our approach was to reduce wafer thickness to 150 μm prior to etch. Subsequently, etch was carried out by the MEMS and Nanotechnology Exchange in Reston, VA (www.MEMS-Exchange.com). The optical image of the wafer after etch is shown in Figure 4.2. In this optical photograph, the

shade differences in the resist indicate the $95\mu\text{m}$ thickness of the resist. The resist used was Futurrex NR5-8000, which is a negative resist.

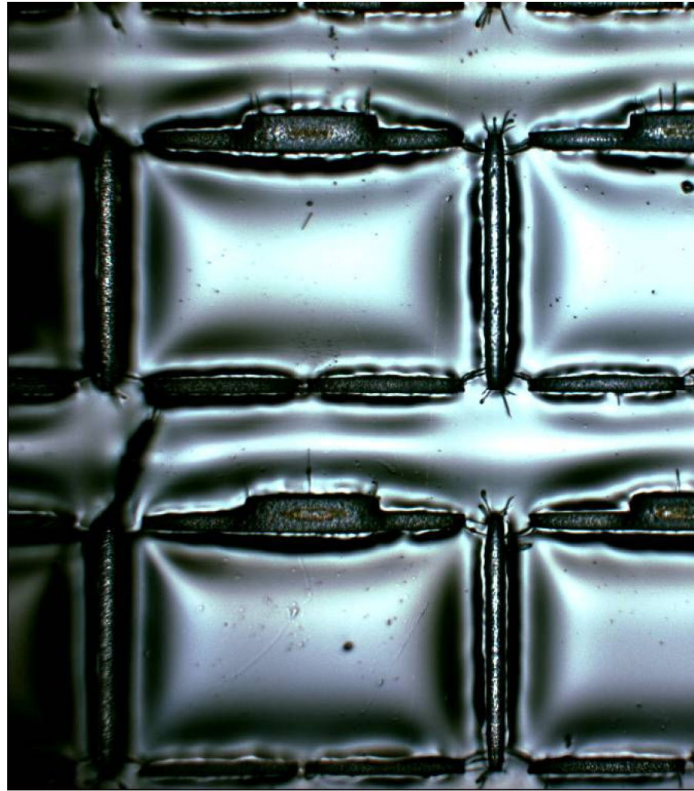


Figure 4.2 Deep etch through GaAs carried out by the MEMS and Nanotechnology Exchange.

For this dissertation, it is noted that the RIE step is not required for the purposes of evaluating the capacitive detection scheme. The process above was developed in order to validate the feasibility of this scheme for use in scanned probe techniques which require cantilevers on an edge. Thus for the rest of this dissertation, the third step is skipped.

In the fourth and final step, the cantilevers are released in 49% HF. This process is done delicately to protect the cantilevers; the under-etch of the AlGaAs is not a very controlled process, and etch rates can vary widely. Thus constant monitoring of the etch is required. Care is taken never to remove the chips from liquid during and after this process.

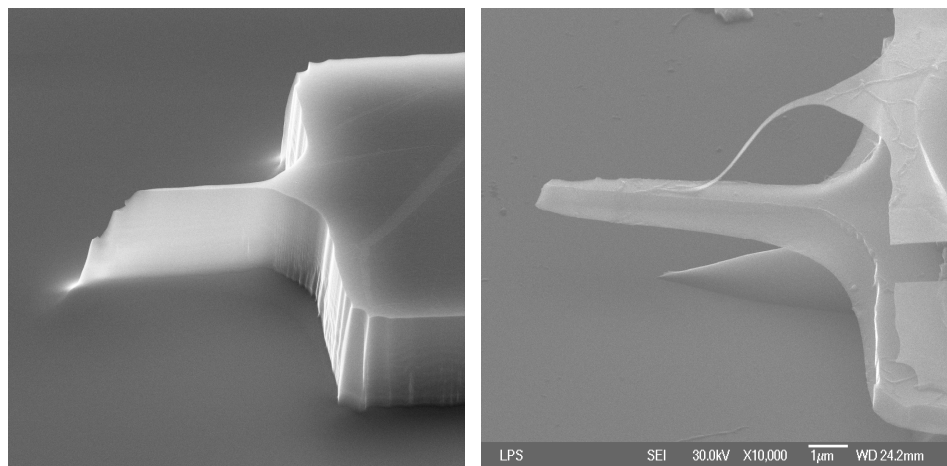


Figure 4.3 Two SEM micrographs showing double cantilevers before and after the selective HF etch. The picture on the right after the HF etch shows how critical point drying is necessary in order to prevent surface tension forces from causing damage

The chips are transferred in methanol to a critical point dryer in order to prevent surface tension forces from damaging the cantilever. Supercritical drying in CO₂ is carried out.

This process is very important since the cantilever after the release is very delicate and can be easily damaged. Surface tension forces can cause the 30 nm thick cantilever to stick to the bottom cantilever. This is shown in Figure

4.3. Hence care is taken in performing this step diligently. Critical point drying is carried out in a Tousimis Samdri PVT-3B apparatus.

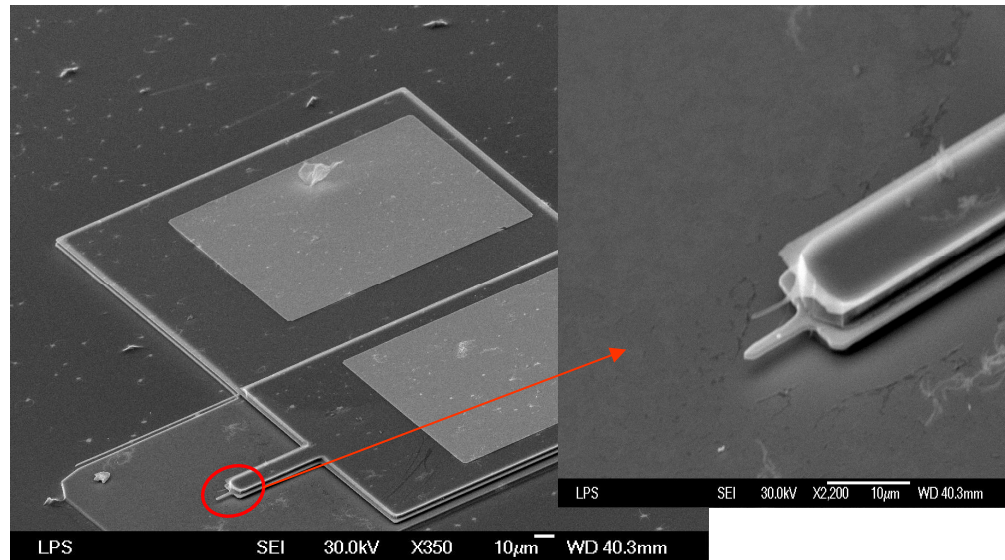


Figure 4.4 SEM micrographs of a cantilever chip. The left one shows a chips complete with bond pads and the cantilevers at the end of an 'arm'. The right shows the double cantilever

In Figure 4.4, a cantilever chip with the double cantilever is shown. The double cantilever is suspended at the end of a long arm (50 mm long and 20 mm wide). The cantilevers are clearly seen to be suspended. Further the bond pads making electrical contact to the two cantilevers are also seen in the micrograph.

However, it is noticed that the exact point of suspension of the cantilevers is difficult to control. This is because of the sacrificial etch under the cantilevers is isotropic, thus the cantilever is suspended not off a straight edge, but off a curved edge. Given this, it is very difficult to predetermine

analytically the frequency of the cantilevers. Finite element analysis was performed for typical geometries obtained by this etch and the frequency was shown to be 155-170 kHz.

4.3 Conclusion

A process to fabricate cantilevers in a double cantilever configuration was developed and ultra-thin cantilevers were fabricated. The 30nm thick resonator is one of the two ultra-thin microfabricated cantilevers to date, and was the first reported. Future work would focus on the read-out of these ultra-thin cantilevers using a capacitive detection scheme.

Chapter 5

THE FIELD EFFECT TRANSISTOR

5.1 Introduction

The previous chapter described the process development that led to the fabrication of ultra-thin cantilevers with an integrated sense layer fabricated together as a double cantilever. This demonstrated the feasibility of fabricating ultra-thin cantilevers required for MRFM. Another step towards achieving very high sensitivity is to demonstrate the feasibility of fabricating field effect transistors (FETs) that can function as low-temperature amplifiers.

As described in Section 3.7, impedance transformation can be achieved by the use of an FET close to the double cantilever scheme. This is a very desirable configuration since this scheme has the potential for broadband detection. Given that the frequency of the cantilevers is not very well known and can vary greatly depending on the etch parameters and the growth of the double capacitive layers, it is desirable to have a scheme where the frequency can be scanned easily. This is the reason that FETs are particularly attractive for achieving impedance transformation.

This chapter describes the fabrication and characterization of GaAs/AlGaAs FETs that can eventually be integrated into the same chip as the

cantilevers. This would achieve the purpose of laying the groundwork for future fully integrated, simple-to-read cantilevers for MRFM.

5.2 Commercial FET characterization

Since the first design was to find if the measurement scheme using an FET is feasible, the use of commercial FETs are very desirable, since this does not require extensive process development in order to fabricate custom-made FETs. The ATF-35143 high electron mobility transistor (HEMT) from Agilent Technologies [33] has been shown to have noise temperatures as low as 100mK at low temperatures of below 400mK [34]. The disadvantage is that operating frequencies for such amplifiers are typically high, in the 1 MHz to several GHz regimes. The corner frequency of the $1/f$ noise for this transistor is 300 kHz, which is above that of the cantilevers in this dissertation.

However, it is noted that the very low voltage noise is not required for the sensitivity estimates in this scheme. In fact, in the estimates in Chapter 3 for sensitivity, the assumed voltage noise resolution of $50\text{nV}/\sqrt{\text{Hz}}$ yields sensitivity of several orders of magnitude below that of the thermomechanical noise. Thus the noise of the transistor below 300 kHz is also of interest.

In order to characterize the HEMT at low temperatures the HEMT was mounted on a board attached to a probe as described in Appendix B. The probe was then cooled to 4.2K by dipping in liquid Helium. The I-V

characteristics of the probe were extracted and is shown in Figure 5.1. The characteristics clearly show the instability of these HEMTs, as can be evidenced from the sudden jumps in the I-V characteristic. Further, these instabilities were not repeatable. Configuration of these HEMTs as low frequency amplifiers showed sudden jumps in gain that could potentially hurt measurements.

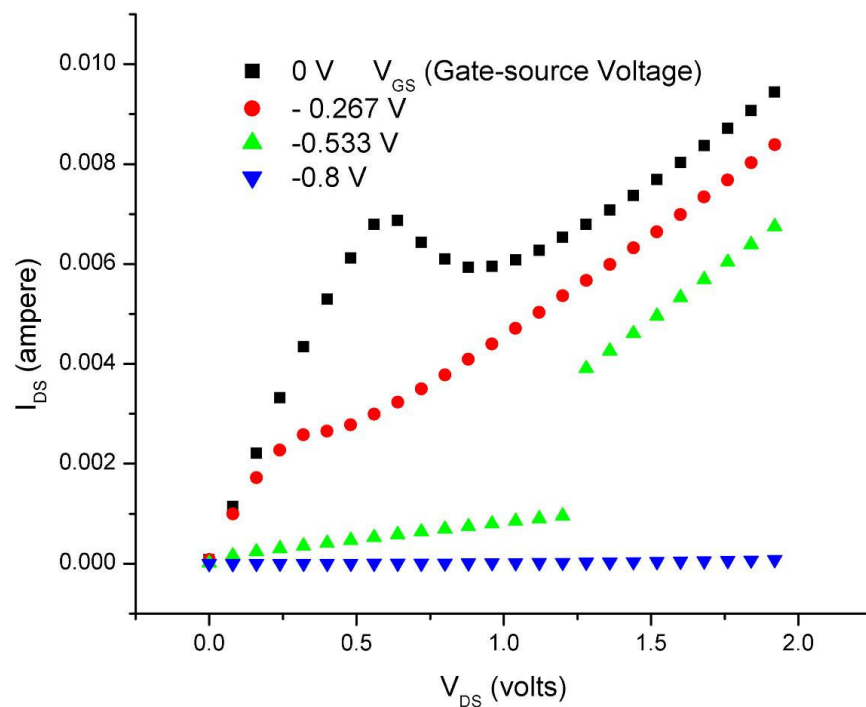


Figure 5.1 Measurement showing instabilities in the I-V curves for a ATF-35143 HEMT at 4.2 K

Thus, the use of commercial FETs for initial characterization was not possible without extensive investment of time and effort in their optimization.

Further, since the eventual goal is integration of the components, it was decided to fabricate FETs for the purpose of future measurements. The rest of the chapter described the fabrication and measurements of the characteristics of the fabricated FETs.

5.3 The Structure for Custom FET

As mentioned in Section 3.2, GaAs/AlGaAs FETs are a good choice for this purpose, particularly because of their usability at low temperatures. This is critical for MRFM where experiments are typically conducted at and much below 4.2 K (liquid Helium). One of the goals of this thesis is to realize simple FETs without extensive epitaxial growth, since that would ease integration of components (the cantilevers and the FETs) in future. Another goal is also to fabricate FETs with input capacitance lower than 30 fF, since that would minimize signal division due to input capacitance of FET.

In order to realize such FETs, the structure of the wafer chosen was similar to Beck et.al. This structure suspends a two-dimensional electron gas (2DEG) 1500 Å below the surface. The benefit of using this structure was the simplicity of the growth. This structure has a total epitaxial growth of 0.95 μm, thus potentially easing integration onto the mechanical layers of the double cantilevers. At the same time the 2DEG is sufficiently beneath the surface to minimize input gate capacitance as compared to [27]. The structure is shown in Figure 5.2.

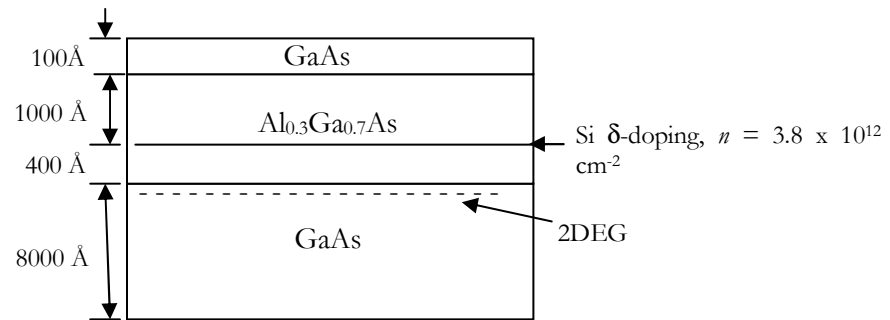


Figure 5.2 Cross sectional view of the field effect transistor (FET) to show the structure of growth

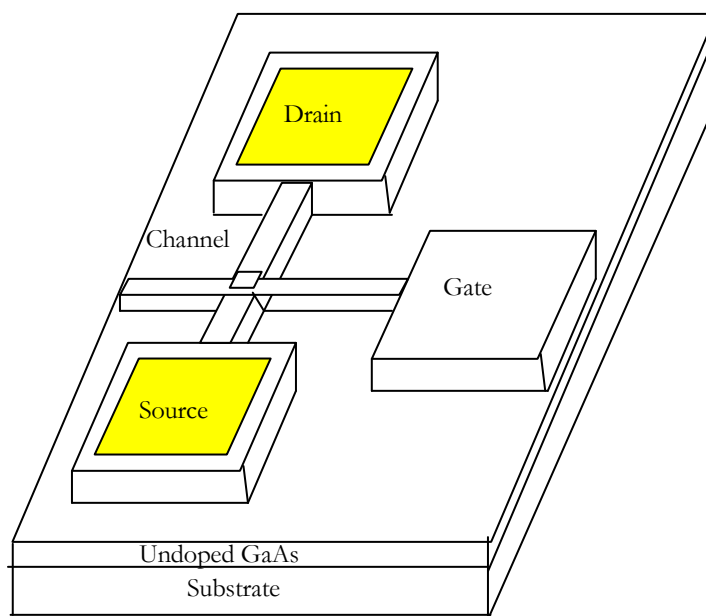


Figure 5.3 Schematic showing the FET structure including the drain, source and gate

The FETs are fabricated on such a structure. For the FETs described in this thesis, the structures were grown by molecular beam epitaxy by a commercial epitaxial vendor [IQE, Inc., Bethlehem, PA]. The substrate was undoped

GaAs. The doping density (2DEG) as measured by the manufacturer was $3.55 \times 10^{11}/\text{cm}^2$. The mobility of the 2DEG as obtained from hall measurements by the manufacturer is $7.46 \times 10^3 \text{cm}^2/\text{V s}$. a schematic of the FETs on the wafer is shown in Figure 5.3.

5.4 The FET Measurement Concept

The three-fold goal of having a simple GaAs/AlGaAs heterostructure for the FET, low input capacitance to the FET as well as broadband response are difficult to meet. Consider the first two goals together: A simple FET structure would mean that the 2DEG is not far below the surface (since growth is minimized to maintain simplicity and to keep costs down). However, this would mean that capacitance would increase, since gate capacitance is a function of the proximity of the gate electrode to the 2DEG.

Similarly the second and the third goals are also contradictory. To keep capacitance low, both the gate dimensions as well as channel dimensions must be minimized. However, minimizing the channel width would mean higher channel impedance. This would restrict the bandwidth unless mobility can be increased greatly. Thus it is clear that the three goals are in general very difficult to meet and a compromise must be engineered.

Given the structure described in the previous section, an alternative is to use one FET with low input capacitance, but higher channel resistance, and

couple the output of this FET amplifier to another FET with higher gate capacitance. The second FET is relatively close to the first one, such that the channel resistance of the first does not restrict the bandwidth sufficiently before being coupled to the second.

This concept can be viewed on the circuit model shown in Figure 5.4 and is meant to give an overall picture of the impedance transformation network.

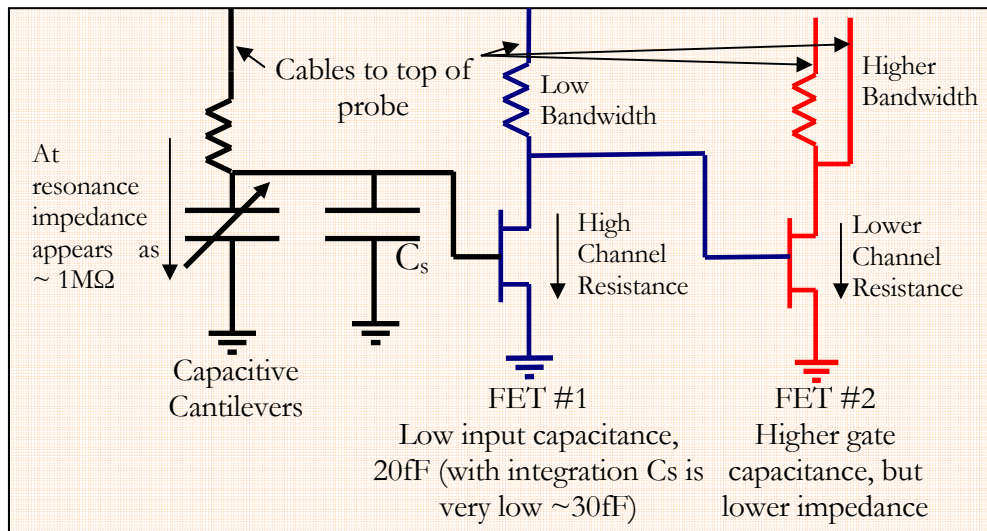


Figure 5.4 Circuit model showing impedance transformation using 2 FETs, once with lower gate capacitance and other with higher gate capacitance but greater bandwidth

Thus, this would require fabrication and testing of two types of amplifiers. In the following section, I describe the fabrication and IV characterization of the FETs with lower channel resistance and a capacitance of 1.75 pF.

5.5 Process Development for FET Fabrication

The fabrication of FETs using the structure grown as described in section 5.2 is carried out using a three mask process. There are several issues to be tackled in the successful fabrication of HEMTs. Among the most pertinent issues is the fabrication of ohmic contacts, which is the first mask layer.

To make the contacts, the following layers were evaporated using a standard electron beam sputtering system: 10 nm Ni, 30 nm Ge, 30nm Au, 80 nm Ni and 300 nm Au. These are standard ohmic contact layers for GaAs. Annealing of ohmic contacts is necessary in order for the dopant Ge to make a contact to the 2-DEG. The ohmic contacts are 150 μm square.

An indication of sufficient annealing is visual and highly subjective. While exact mechanism of the annealing process is unknown [36], it is generally accepted that Ge acts as a dopant and at elevated temperatures diffuses into GaAs to make contacts. This diffusion process causes the surface of the contacts to have ‘wart-like’ texture. This was observed post-annealing in our samples and is shown in Figure 5.5 .

The optimization of annealing times was performed using a probe station and multimeter. The resultant graph is shown in Figure 5.6. The contact resistances were measured using 2- and 4-wire measurements and were 170 - 200 Ω at room temperature and 110-140 Ω at 4.2 K.

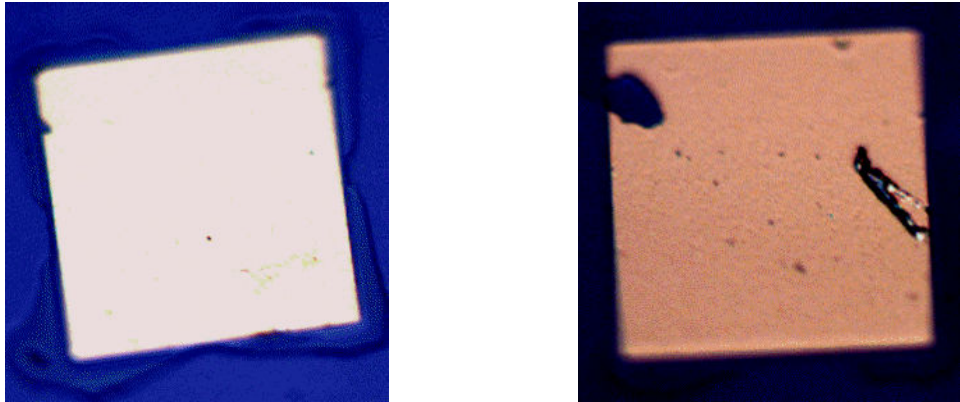


Figure 5.5 Optical Microscope images of a bond pad pre and post annealing. The picture on the right shows an annealed contact, and surface roughness is seen

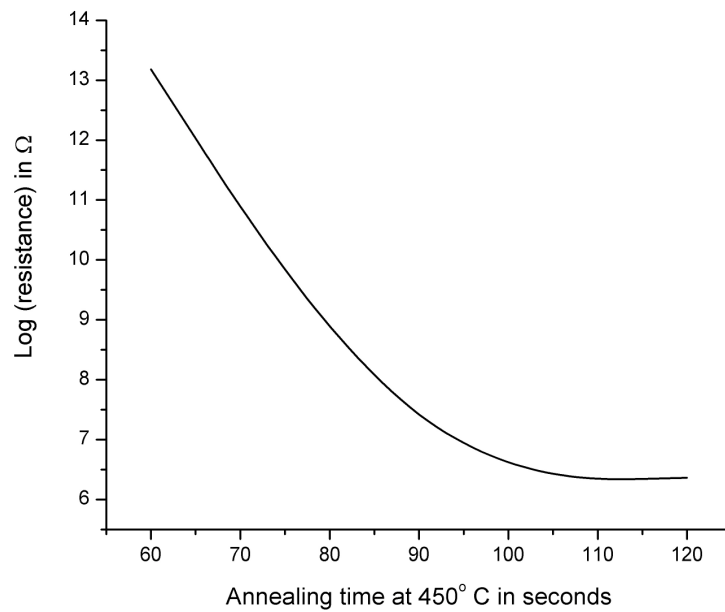


Figure 5.6 Optimization of annealing times. Resistance drops as contact is made to the 2DEG

It is seen in Figure 5.6 that the resistance drops as the annealing time at 450° C is increased. Beyond a certain time, though the resistance does not

change appreciably, indicating that contact has already been made. The annealing time used for the FETs described in this dissertation is 120 s.

Once the ohmic contacts to the 2DEG are made, the next step is to define the channel. The channel is defined using standard photolithography and is etched using an inductively coupled plasma reactive ion etching tool (ICP-RIE). The gases used for the etch is a combination of BCl_3/Cl_2 . The depth of etch is such that the 2DEG has been constrained to the channel dimensions. Thus etching is carried out into the lower undoped 8000\AA GaAs layer. This defines the FET channel.

The final step is the evaporation of a Schottky gate. This is a standard Au gate evaporated using e-beam evaporators. The thickness of the gold layer is such that it is greater than the depth of the channel etch ($< 2000\text{\AA}$) in order to provide continuity. In this dissertation, the gates are 3500\AA thick. A thin Ti layer is evaporated prior to Au to provide superior adhesion.

The next section explores the results of the fabrication and characterization of the FETs with higher gate capacitance (2pF) and lower channel resistance, what I term to be the wide-channel FET.

5.6 Wide Channel FET

As mentioned earlier in this chapter, the FETs with larger input capacitance are fabricated in order to use them as low-temperature amplifiers.

Since the initial design comprises of cantilever system with large bond pads (and the associated large stray capacitance), these FETs will probably serve quite well for initial characterization of the system of cantilever coupled to FETs. The initial coupling can be done using wire bonds close to the cantilever chip.

The FETs have ohmic contacts that are $150\mu\text{m} \times 150\mu\text{m}$ and a channel with a width of $150\mu\text{m}$ and length (between bond pads) of $100\mu\text{m}$. The gate is $15\mu\text{m}$ wide. The ohmic contacts, channel and the gate are fabricated as described in Section 5.5. One such FET is shown in Figure 5.7.

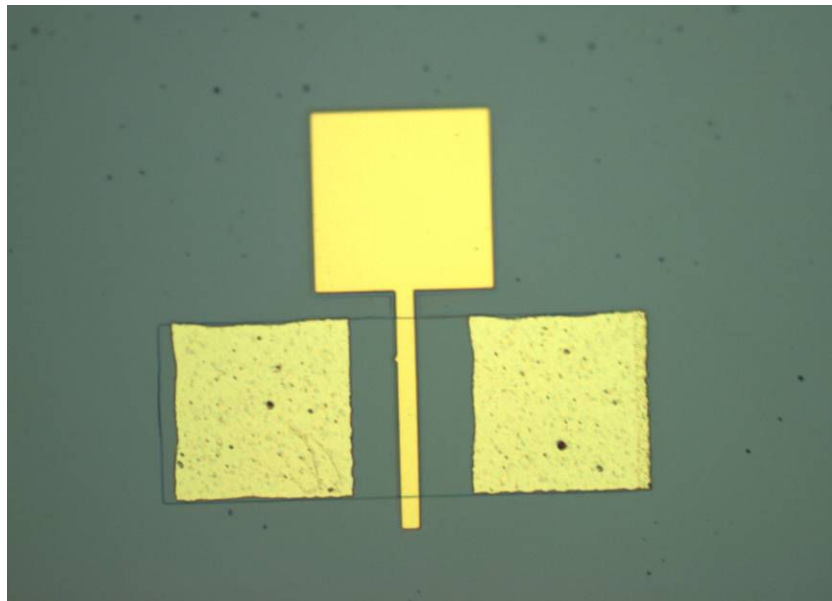


Figure 5.7 An optical microscope image of a wide-channel GaAs FET

The input capacitance to the FET can be easily obtained knowing the width of the gate and channel (which gives the area of the gate) and the depth

of the 2DEG (1500 Å for the structure used in this dissertation). For the wide channel FETs this is calculated to be 1.75pF.

The I-V curves for the fabricated FETs were obtained by mounting the FETs on a board similar to the one described in Appendix B. The I-V curves are extracted by sweeping the voltage and measuring the current through the channel at various gate-source voltages. Characterization was carried out at both room temperature and at 4.2 K. The temperature could be verified by a thermometer attached to the circuit board. Since the channel can be depleted by applying negative voltages the current through the channel can be modulated by the gate potential. Figure 5.8 shows a series of current-voltage (I-V) curves at different gate-source voltages (V_{GS}) at room temperature (295 K). As expected the saturation current in the channel decreases for decreasing V_{GS} .

This confirms that the wide FETs are functional and the gate potential effectively modulates the channel current. This property of FETs is used for amplification widely [30]. Observation of the I-V curves of the FET yields information as to the operating point of the FET for effective amplification. For this FET the saturation region of I_{DS} is an obvious operating point.

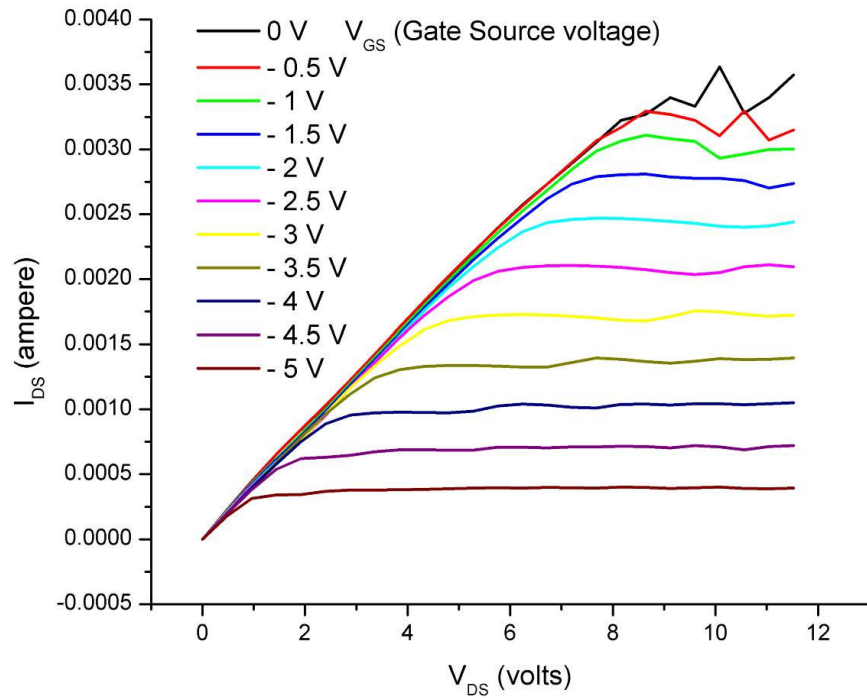


Figure 5.8 Measured I-V Characteristic for the Wide FETs at 295 K

To characterize the amplification of the FET, transfer characteristics are obtained. The transfer characteristic at 293 K for $V_{DS} = 12$ V is plotted in Figure 5.9. It is seen that the channel current can be ‘pinched-off’ at -5.8 V. The slope of the transfer characteristic is the transconductance g_m . For this transfer characteristic $g_m = 0.0012$ S. The transconductance is useful to find the amplifying characteristics of an FET as will be seen later.

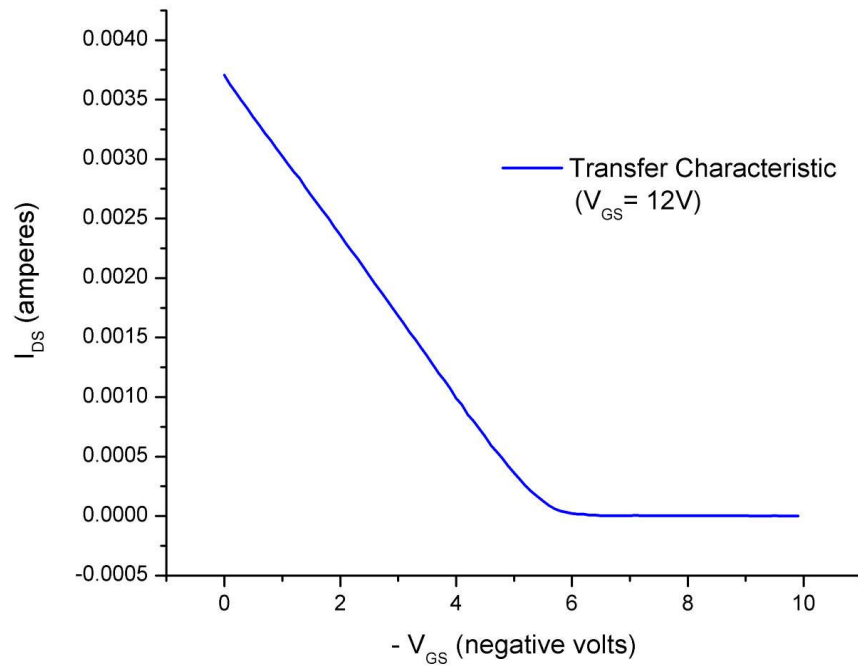


Figure 5.9 Measured Transfer Characteristic of wide FET at 293 K

The next goal is to characterize the FET at low temperatures. For the purposes of this dissertation this is 4.2 K, which is liquid Helium temperature. The probe (described in Appendix B) is dipped in a liquid helium dewar, and the temperature of the board is monitored. Typically a puff of helium is introduced into the probe which rapidly cools the electronics inside. The He is then pumped out using a turbo mechanical pump. The I-V curves for the FET are extracted. A set of curves for the FET is shown in Figure 5.10. Once again, the channel current is modulated by a gate potential, and can eventually be pinched off.

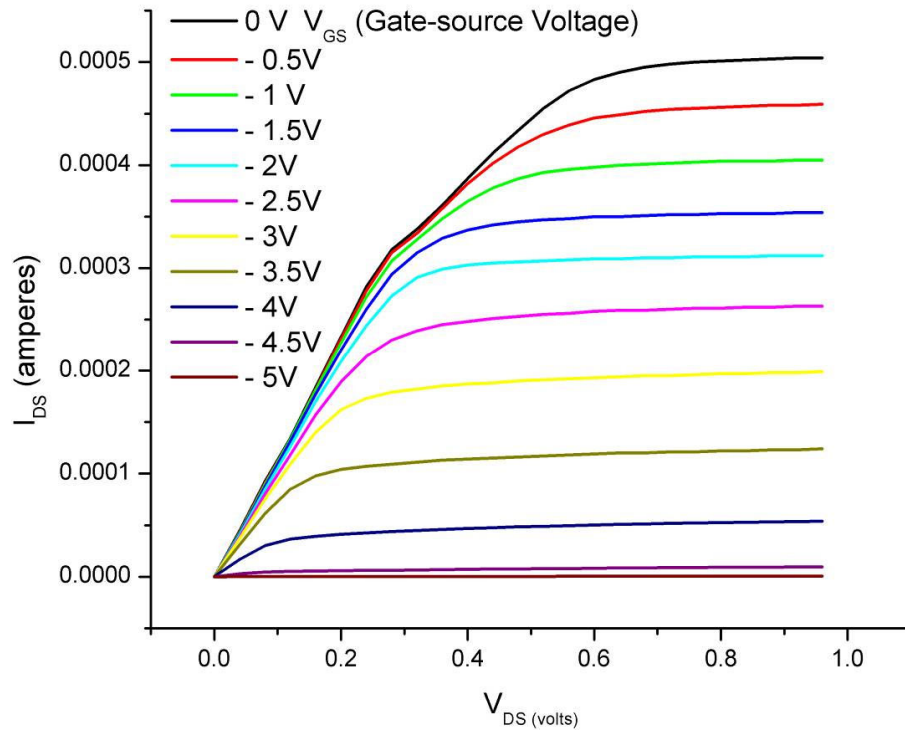


Figure 5.10 Measured I-V Characteristic of Wide FET at 4.2 K

The FET current at saturation is lower as expected, since fewer carriers are available for conduction at 4.2 K. The transfer characteristic at 4.2 K is shown in Figure 5.11. For this transfer characteristic $g_m = 0.001$ S.

Another aspect of FETs that could be a potential problem is gate leakage. Gate leakage appears as a resistance to ground at the gate, and this could act as a voltage divider (see Figure 5.4). Typically gate leakage can be minimized or even eliminated by choosing values of V_{GS} and I_{DS} such that the amplification is minimal. This is the most practical method, since gate leakages and optimal

operating point vary considerably for the FETs described in this thesis. This method is very simple to implement and hence the preferred method for biasing the FET at its optimal operational point.

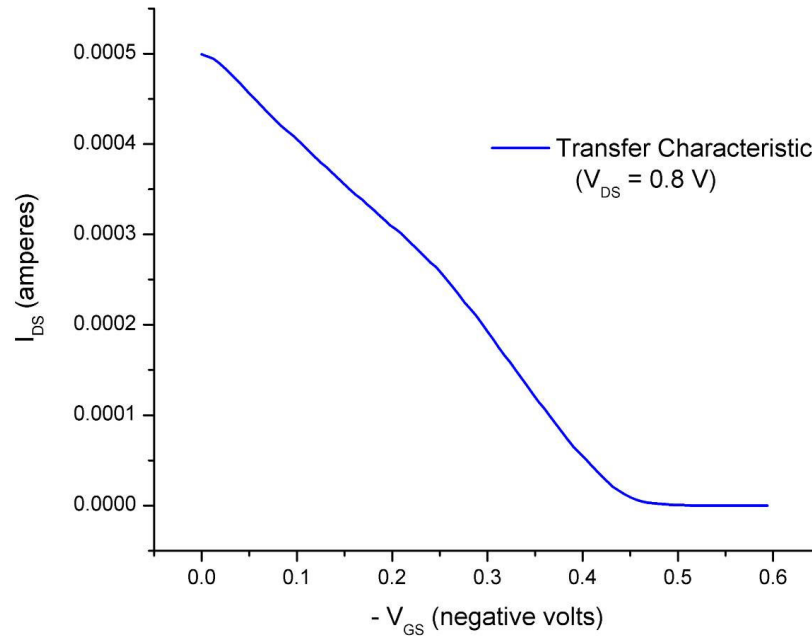


Figure 5.11 Measured Transfer Characteristic of wide FET at 4.2 K

This section demonstrated the fabrication and characterization of FETs at low temperatures. It can be verified from the I-V curves at 4.2 K that the resistance of these FETs are $\sim 1 - 2 \text{ k}\Omega$ for typical regions of operation as an amplifier (saturation or near saturation), depending on the gate potential. Given cable capacitances of 500 pF (conservative estimate), the bandwidth can be estimated to be around 1 MHz. Thus these wide FETs satisfy the

requirement of a low temperature amplifier with sufficient bandwidth in order to do measurements upto 1 MHz.

The following section describes the fabrication and characterization of FETs with lower capacitance, but low bandwidth that can be used as the first-stage amplifiers.

5.7 FETs with 21fF Input Capacitance

In this section the fabrication of FETs with low input capacitance is described. In order to keep input capacitance below 30 fF, the area of the gate and the channel have to be adjusted given that the 2DEG for this particular structure is located 1500 \AA beneath the surface. For a channel width of $20\mu\text{m}$ and a gate width of $15\mu\text{m}$, the capacitance is 21fF. Also, this geometry makes it practical, since feature sizes are easy to realize using unsophisticated photolithography. Hence this geometry is chosen. The length of the channel was kept at $100\mu\text{m}$ as in the wide FETs to enable one to use the same first-step mask as before. The FETs are fabricated using the same technique described for the wide FETs. A fabricated FET is shown in Figure 5.12. Figure 5.12 shows a magnified SEM micrograph of the gate region. This demonstrates that the gate is continuous over the channel, as is required for proper operation of the FET.

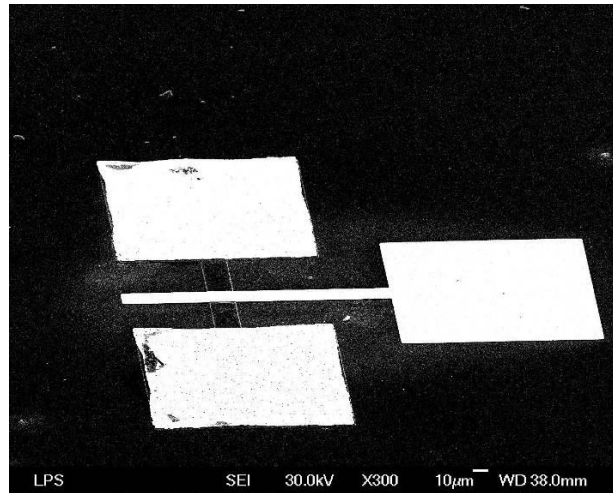


Figure 5.12 SEM Micrograph of a FET with lower capacitance

Upon fabrication the FETs were characterized and the I-V curve at 4.2 K is shown in Figure 5.14. The I-V characteristics of the FET confirm that they work at 4.2 K with gate potential modulating the current in the channel. The current through the channel is effectively pinched off for $V_{GS} < -4.5V$. The transfer characteristic of this FET at 4.2 K is shown in Figure 5.15. From the transfer characteristics, it can be inferred that the transconductance g_m of this FET is $\sim 1mS$.

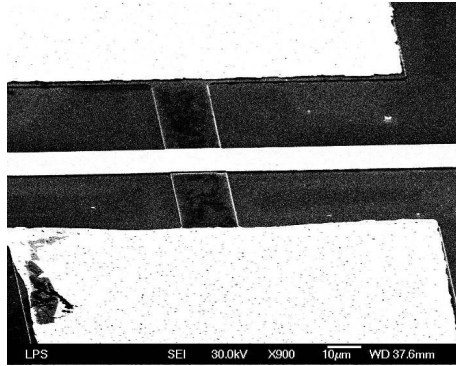


Figure 5.13 Close-up of the gate region of the channel

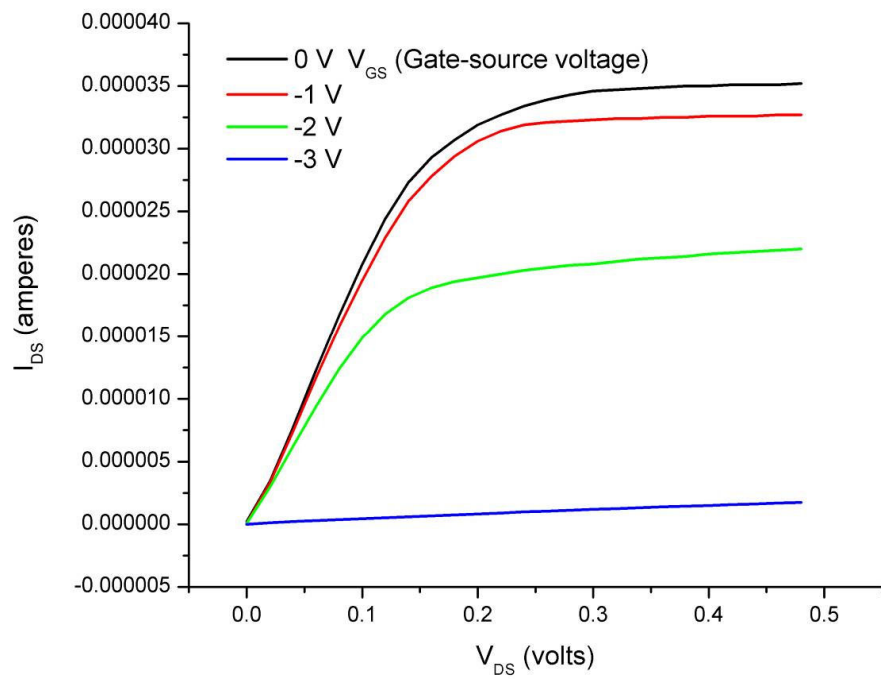


Figure 5.14 Measured I-V characteristic for the low capacitance FET at 4.2K

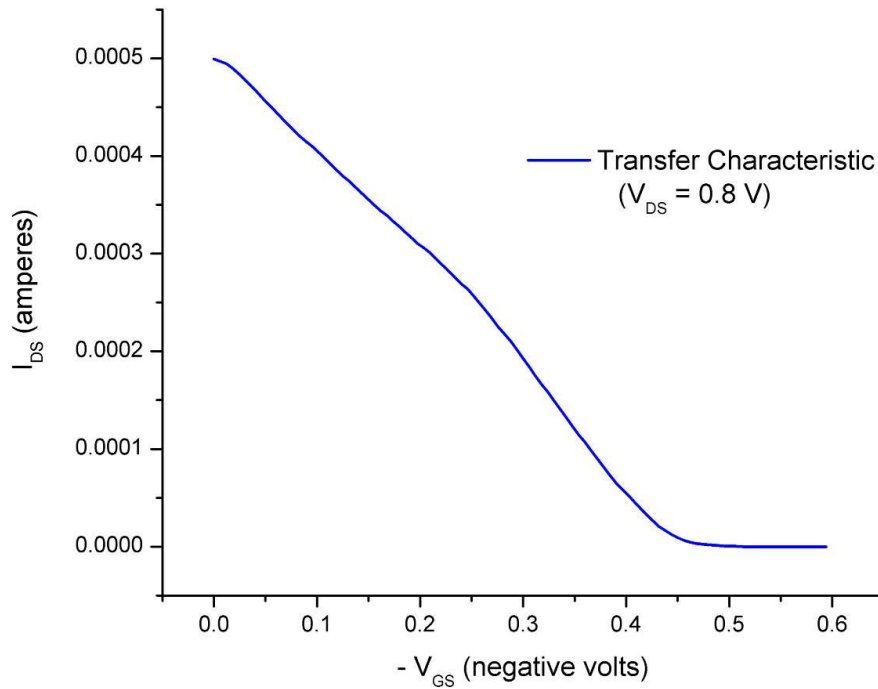


Figure 5.15 Measured transfer characteristic for the low capacitance FET at 4.2 K

In order to operate the FET as an amplifier, a resistor is coupled to the FET as shown in Figure 5.16. The voltage gain of an amplifier configured such is given as follows:

$$\text{Gain} = g_m \times R_D \tag{5.1}$$

Since g_m is given by the slope of the transfer curve, the gain of an FET can be determined by the value of the bias resistor R_D . We chose a value of 200 k Ω for this FET in order to get voltage gain of 10-50.

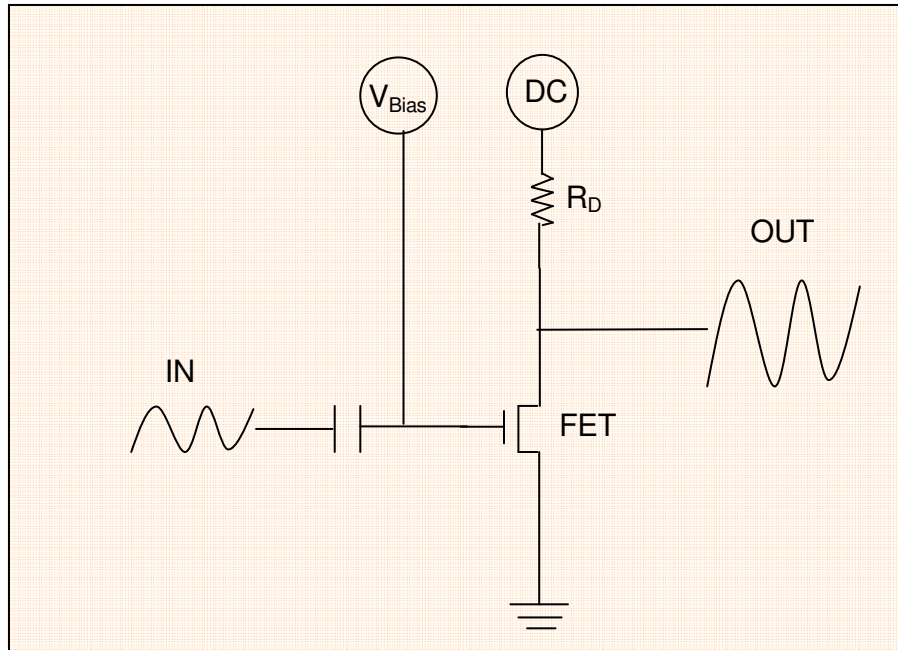


Figure 5.16 A simplified circuit demonstrating the use of FETs as amplifiers

Another important parameter of the narrow FETs is the power dissipation. Since these FET are designed for use directly on the cantilever chips, large power dissipation can heat the cantilever chips. Typical cryostats can tolerate power dissipation in the region of a few milliwatts. The power dissipation of the transistor is simply the product of the current and the voltage through the channel, if gate leakage effects are ignored. Since the gain depends on the operational characteristics of the FET, it is instructional to find the how the power dissipation varies with the gain of the amplifier.

Such a plot for the FET amplifier at 4K is shown below. The power dissipation even at relatively high gain (>20) is less than 10 μW , which is very suitable for low-temperature applications.

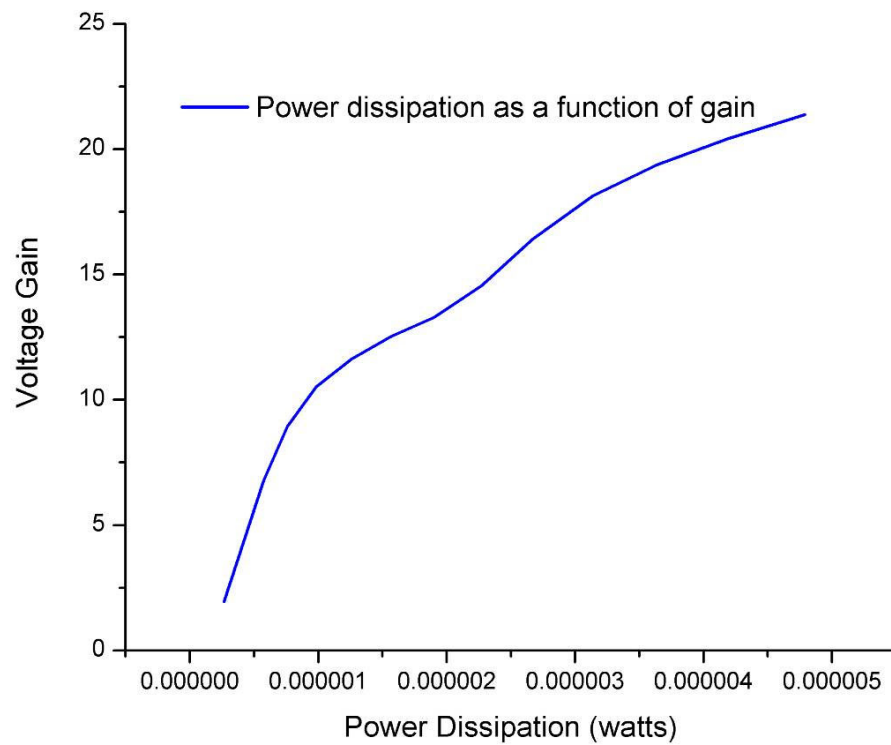


Figure 5.17 Measured relationship between gain and power dissipation

Thus, the FETs with low capacitance (21fF) are characterized at low temperatures. The power dissipation through the FETs is acceptable for He-3 cryostats that are used for MRFM experiments.

5.8 Conclusion

In this chapter, the successful fabrication and measurement of the characteristics of two FETs was described. One of the FETs, with the 21 fF input capacitance, can eventually be integrated onto the same chip as the mechanical layers, thus enabling an integrated read-out of mechanical motion.

The second FET can serve as an amplifier close by, for instance on the same circuit board, and can serve to further transform impedance and increase the bandwidth of measurement. Since the structure of both FETs is identical, it is entirely possible to fabricate both FETs, on the same chip as the mechanical components too. Thus the fabrication and successful characterization of these FETs makes possible a variety of different configurations for testing. For the purposes of initial measurements, the wide FET will be used.

Chapter 6

MEASUREMENTS AND CHALLENGES

6.1 Issues of Measurement of the Cantilever Motion

In any type of ultrasensitive measurement technique the issue of parasitic capacitance, from bond pads, wire bonds, leads and the cables is always a concern. While impedance transformation is the most common and practical technique used in all ultrasensitive measurements, such techniques become more difficult as cantilever masses become smaller.

Another issue is the relatively unknown frequency as well as the Q of the cantilevers. In order to find the resonance frequency a broadband technique is required, which was among the reasons for an FET-based detection. However, since the parasitic capacitance for the set-up described in this dissertation (where integration of FETs on the mechanical layers has not been carried out) is prohibitive, it would be very useful to know the resonance frequency prior to an electronic read-out.

6.2 Experimental Set-Up to Read-Out Cantilevers

As described in Section 3.7, the FET detection without integration of the FETs on the same chip as the cantilevers will not be sensitive enough for direct read-out of the thermomechanical noise. This is because of the large

parasitic capacitance due to the bond pads and the wire bonds. Further the FET with 2pF input capacitance was used, thus adding to the parasitic capacitance.

In order to keep the noise of the electronics low, and to increase the Q of the resonator, all measurements were performed at vacuum at 4.2 K. This was done in the probe described in Appendix B. The expected position detection sensitivity of the system can be obtained from the spreadsheet described in Appendix C and is estimated to be $4.3 \times 10^{-17} \text{N}/\sqrt{\text{Hz}}$. This is significantly lower than the thermomechanical noise figure of $2.5 \text{aN}/\sqrt{\text{Hz}}$, hence it would not be possible to directly measure the thermomechanical noise peak at the resonant frequency of the cantilever. Hence, the cantilever needs to be driven in order to obtain a signal above the noise floor of the detector.

In order to drive the cantilevers, the cantilever chip is mounted on a piezoelectric stack [37]. This must be done ensuring that care is taken to minimize cross-talk of the drive with the cantilever signals. In order to electrically isolate the cantilever system from the piezoelectric stack, the top of the stack (on which the chip was mounted using silver paste) was grounded. The bottom of the stack was attached with conducting silver paste to a gold-plated cover slip. The cover slip was then attached to the grounding plane of the circuit board. This arrangement is done so that the piezoelectric stack is not driven on the side the cantilever is mounted, thus minimizing cross-talk. This is shown schematically in Figure 6.1.

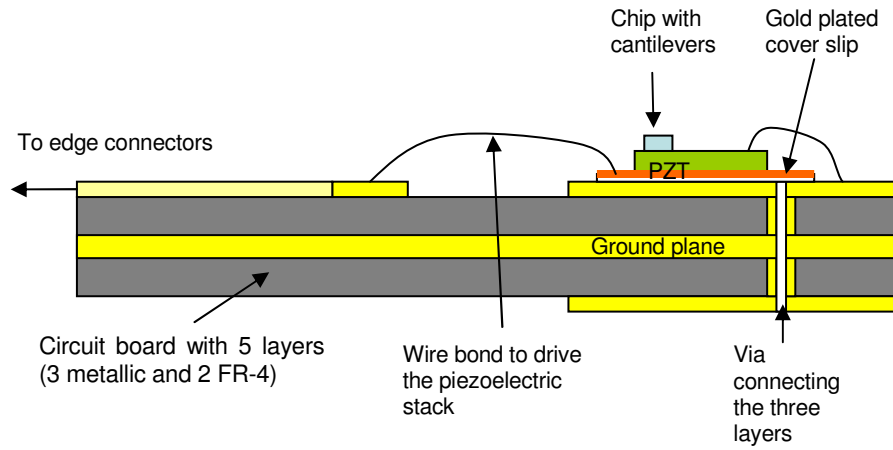


Figure 6.1 Figure showing the mounting of cantilever on piezoelectric stack to minimize cross-talk

The circuit used to couple the cantilevers to the wide FET described in Section 5.6 is shown in Figure 6.2. The V_{Bias} is the voltage bias for the cantilevers, and must not exceed the pull-in voltage. The V_{DC} is a DC potential applied to bias the FET operating point such that the FET has minimum leakage current. The V_{DS} is as before the drain-source voltage, and is applied such that the FET is biased at the desired operating point. In addition, to monitor the gain constantly, a lock-in was used, with a small AC applied at the gate. The gain was monitored at lower frequencies (typically 10 kHz).

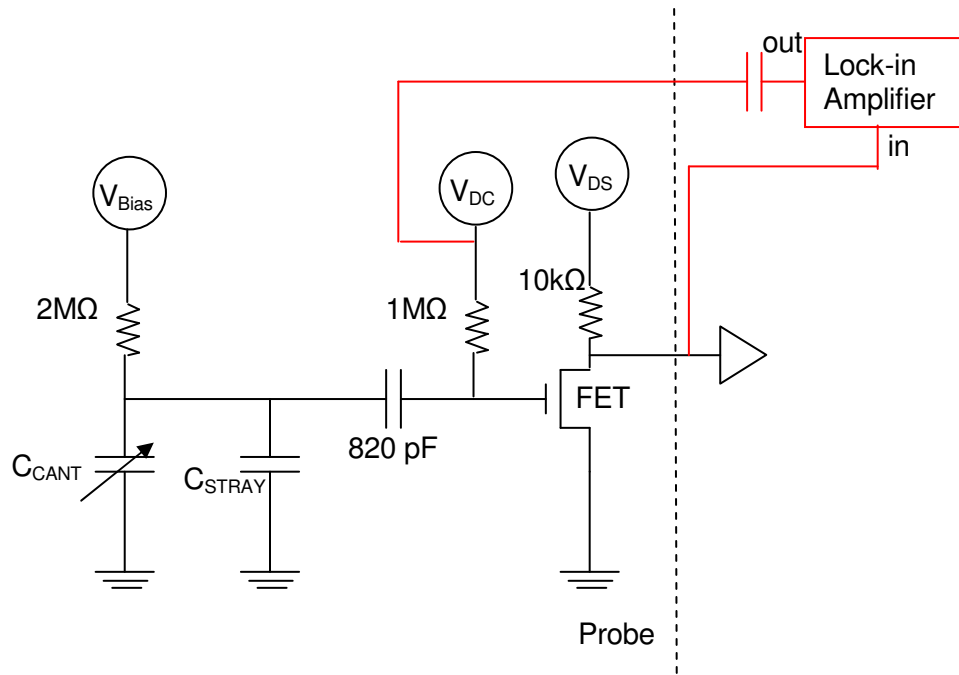


Figure 6.2 Circuit for measurement of cantilevers coupled to the wide FET

The temperature was monitored using a carbon glass thermometer as described in Appendix B. The cantilever chips were attached to the piezoelectric disc which was connected to the top by a separate wire. This set-up is shown in Figure 6.3.

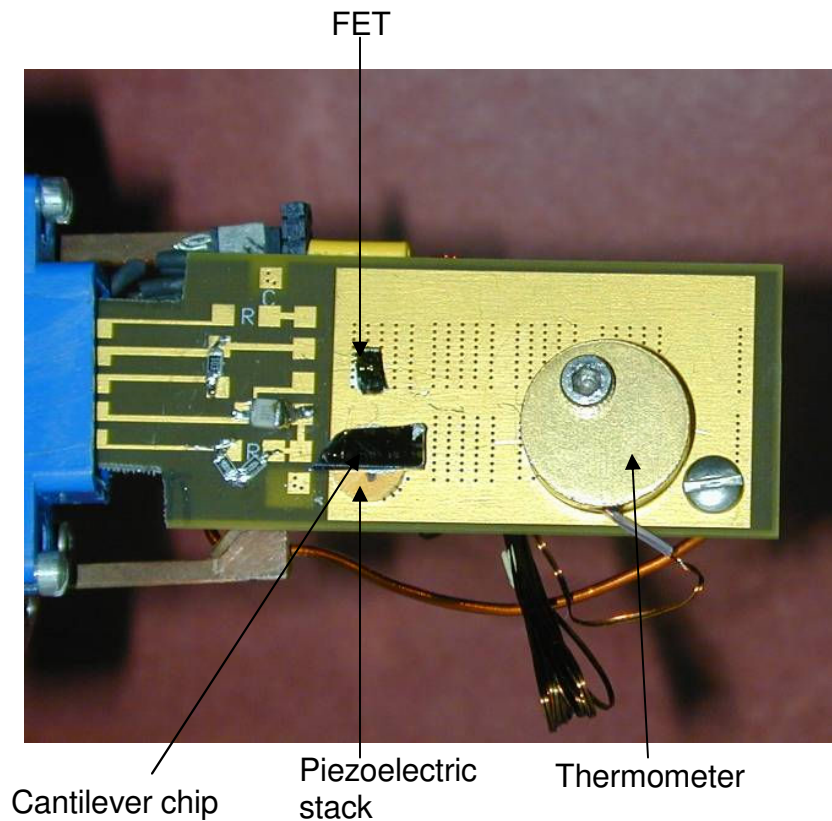


Figure 6.3 Photograph showing the circuit board used for measurements

Each individual circuit component was tested for their usability at 4.2 K prior to mounting on the circuit board. The cantilevers thus mounted on the probe were hermetically sealed using indium seals and cooled down to 4.2K in liquid helium. The value of the cross-talk when a AC voltage is applied to the piezoelectric stack can be monitored at the output of the FET without having a DC bias on the cantilever. The cross talk was approximately $10\mu\text{V}$ per volt supplied to the stack. For motion of a nanometer at low temperatures, the

amount of voltage to be applied would be between 20 and 50 V. Thus the amount of voltage due to cross talk can be as high as 50 μ V. This would severely restrict the experiment's capability. Thus this approach was abandoned, since the cross-talk corrupted the measurements. It is noted that extreme care was taken to minimize the effects of cross-talk, and this value could not be reduced further easily.

Another approach is to directly read-out the cantilever thermal noise using the FET without additional excitation of the cantilevers. This method though at a first glance appears to be less favorable than using excitation, it can be shown is better than using excitation with cross-talk. Since the expected thermomechanical noise is much lower (8aN/ $\sqrt{\text{Hz}}$ corresponding to about 0.23 $\text{\AA}/\sqrt{\text{Hz}}$) than the expected sensitivity of position detection (3.7 $\text{\AA}/\sqrt{\text{Hz}}$), it is not possible to read-out the cantilevers without several averages. However, with 1000 averages of the signal, it is possible to increase the signal-to-noise ratio to approximately 10. Thus, this method was used to perform measurements of the cantilevers. Also since the expected Q of the cantilevers is fairly high, the averages were carried out over frequency ranges of 1kHz, and the frequency was swept from 60kHz to 250kHz. However, this method did not yield the resonant frequency and the Q of the cantilever.

Thus it is seen that direct measurement of the cantilever motion at resonance is not trivial without having prior knowledge of the resonant

frequency. In order to find the resonance frequency two alternate methods were attempted. The goal is to use these methods to find the resonant frequency and then read the cantilevers electronically.

6.3 SEM-based detection

As mentioned in the previous section, the frequency of the cantilevers is to be determined by alternative techniques. One of the issues in trying to read-out objects that are very small like these cantilevers is alignment. The SEM has been used successfully to measure mechanical resonance as described in [39]. This technique is useful because imaging of the cantilever is done prior to alignment, thus enabling us to position the cantilever in the path of an electron beam.

In this technique the mechanical resonator is placed in an SEM and imaged at high magnification (typically 50,000 or above). Thus imaging of the beam is done in the SEM. Then, the resonator is placed such that there is a component of motion perpendicular to the electron beam. The resonator can be excited by mounting it on a piezoelectric stack. The electron beam is then focused on a specific point on the edge of the resonator and the SEM is switched to point mode. Thus now, as the resonator moves in and out of the line of the electron beam, the detector of the SEM has an output at the frequency of the resonator. The output of the detector is analyzed using a spectrum analyzer or a network analyzer.

For the purposes of this dissertation, this technique was used to find the resonant frequency of the cantilever. We looked at the thermal noise peak at room temperature at high vacuum in a field emission scanning electron microscope, where the sample was tilted from the horizontal. This was done to ensure that there is a component of mechanical motion perpendicular to the electron beam. The beam was focused on an edge of the cantilever and the output of the secondary detector of the SEM was monitored with a spectrum analyzer via a voltage amplifier. Two SEMs were used – a LEO 1550 VP and a JEOL JSM-6500F. For the LEO 1550 VP, two hermetic feed-throughs to the chamber were made to enable the excitation of a piezoelectric stack.

The cantilever chip was mounted on the piezoelectric stack and placed in the SEM. The feed through were connected to the output of a network analyzer. However, drifting of the beam at high magnifications caused the beam edge to move away from the center of the beam during measurement. This could be because of the relaxation of the mechanical screws of the SEM used. In order for such a technique to be successful, the drift of the image must be addressed.

It was initially thought that the drift was occurring because of the cantilever getting charged (since the beam is isolated from ground). In order to address this, the beam pads were wire bonded to a ground plane. The piezoelectric stack was excited using a network analyzer and the output of the

secondary detector of the SEM was monitored by the analyzer. However, this did not minimize the image drifting [37].

Thus at this time we are unable to make measurements using this technique, Problems with both image drift as well the transparency of the cantilever could be an issue. Since this technique is mostly empirical with almost no quantitative estimates on sensitivity, it is difficult to determine with precision the exact reason for not being able to find the frequency of the cantilevers.

6.4 Optical Detection of Cantilevers

Another approach is to use optical interferometry. This technique needs advanced interferometry techniques, since typical optical fibers are 9 μ m is diameter and given the transparency of the cantilever the reflected signal would not be sufficient to find the resonance frequency. Also of issue is the alignment of the laser on the cantilever, which requires microscopes with CCD. Such a set-up has been designed and used for sensitive position detection in [40].

This set-up at Boston University was employed to find the frequency and Q of the cantilevers. The set-up included a vacuum chamber in which the cantilevers were mounted on a piezoelectric stack. The chamber was then pumped down to 10mT. The cantilever was then imaged using a lens. The lens served a dual purpose – magnification of the cantilevers such that it can be

seen easily on the monitor screen, as well as focusing of the laser such that the laser spot is smaller than or comparable to the width of the cantilever. This is in contrast to the MRFM measurements that are done without lenses, where the spot size is comparable to the core diameter of the fiber ($\sim 9\mu\text{m}$).

Both Michelson interferometry as well as Fabry-Perot Interferometry techniques were used [41]. Neither technique yielded the frequency of the cantilever.

6.5 Discussion

It is clear that the resonant frequency of the cantilever is to be known in advance in order to make further measurements using the capacitive detection scheme. The finesse of measurements using either the SEM or optical measurements can be improved. Future work will concentrate on the use of one of these detection schemes at room temperature to ascertain the frequency and the Q of the cantilever beams. Once the Q and the frequency are known the exact mechanical impedance of the beam given by Equation (3.5) can be known. Further it would also make the FET-based detection easier, given that current sensitivity of the scheme is estimated to be $\sim 10^{-17}\text{N}/\sqrt{\text{Hz}}$, lower than the thermomechanical noise. There is also the possibility that at lower temperatures, the Q of the resonator may be significantly higher ($>10^5$) which could substantially improve the sensitivity of the cantilevers.

Chapter 7

CONCLUSION AND CONTRIBUTIONS

7.1 Introduction

The previous chapters in this dissertation illustrated a lightless technique to capacitively read-out the position of a ultra-sensitive cantilever. In Chapter 2, a successful fabrication technique with high yield for making thin cantilevers for MRFM purposes was described. Chapter 3 explained the design of a proposed lightless detection technique using capacitive detection. In Chapters 4 and 5 the successful fabrication of a cantilever double layer was described as well as the fabrication and characterization of FETs for operation at low temperatures was discussed. The resonator structure fabricated is just 30 nm thick and is first [31] of only two known ultra-thin cantilevers [44]. In Chapter 6, the non-triviality of the problem of experimentally finding the resonance frequency was examined and some attempted techniques were discussed. In this chapter, I shall conclude this dissertation with a section on the use of direct impedance transformation method (without FETs) to read-out the cantilevers and the contributions of this dissertation.

7.2 Proposed Direct Impedance Transformation

In this section I would like to present a potential impedance transformation scheme for ultra-sensitive measurement using the current double capacitive system without the need for integration. The reason for this is that if the frequency and Q of the cantilevers can be determined using the methods described in 6.1 above, then it is possible to use the method described in 3.6 in combination with other impedance transformation techniques to read out the position. This particular proposal has one distinct, but significant advantage. The parasitic capacitance of the previous scheme can be resonated away using a system of tank circuits. Thus the parasitic capacitance can be a part of the capacitor in a resonant tank circuit.

However, this would require an amplifier with impedance that is lower, such that the mechanical impedance can be transformed to the input of the amplifier. This technique is common, since many amplifiers have an input impedance of 50Ω . However, any amplifier that is used must have a current noise that is not too high such that the current noise drives the cantilever system. This is a requirement in many ultra-sensitive measurements, and a very elegant description of this is available in [42].

The current noise of an amplifier can be conveniently expressed as a temperature equivalent of the cantilever system; typically manufacturers of very low noise amplifiers specify the noise temperature of the amplifier. Some

of the best amplifiers with ultra-low noise temperatures are available for high frequencies [32]. However, for the frequencies of interest in this dissertation (20-300 kHz), the lowest current noise commercially available amplifiers with 50Ω input have a noise temperature of around 40 K [for instance the AM1431 amplifier, manufactured by Miteq Incorporated, Hauppauge, New York]. This means that the best sensitivity that can be achieved is that of the thermomechanical noise of the cantilever at 40K.

It is interesting to use this figure to find the sensitivity of this detection method. Given the dimensions of the cantilever as described in Chapter 3, the mechanical impedance of the cantilever system at resonance is given by Equation 3.14 and is estimated to be $3.51\text{ M}\Omega$ (assuming $Q = 15,000$). Given that the input to the amplifier is 50Ω , the high mechanical impedance is required to be transformed to 50Ω . This can be easily achieved by means of a tank circuit. This is represented in Figure 7.1, where the cantilever at resonance is shown as R_m , the mechanical resistance. The impedance transformation is to be achieved by a tank circuit with inductor L_{TANK} and a capacitor to ground C_{TANK} .

From the figure, it is clear that the C_{TANK} to ground can be the stray capacitance. So long as the value of C_{TANK} required is less than or equal to the stray capacitance of the double cantilever system, this particular impedance transformation scheme can be extremely powerful, since it can resonate the

stray capacitance as part of a tank circuit. Thus the division of the signal by the stray capacitance is minimized.

For the geometry described in this section, the impedance of the tank circuit required to transform $3.51 \text{ M}\Omega$ to 50Ω is given by

$$Z_{LC} = \sqrt{R_m \times 50} \tag{7.1}$$

Z_{LC} is calculated to be $13.25\text{k}\Omega$. The corresponding values for L_{TANK} and C_{TANK} at the resonant frequency of the cantilever (195 kHz) can be calculated to be 11.3 mH and 64 pF respectively. Clearly the required C_{TANK} is greater than the parasitic capacitance (about 2 pF). The required Q for the tank circuit is simply $R_m/\omega.L_{TANK}$, and is shown to be a reasonable 265 .

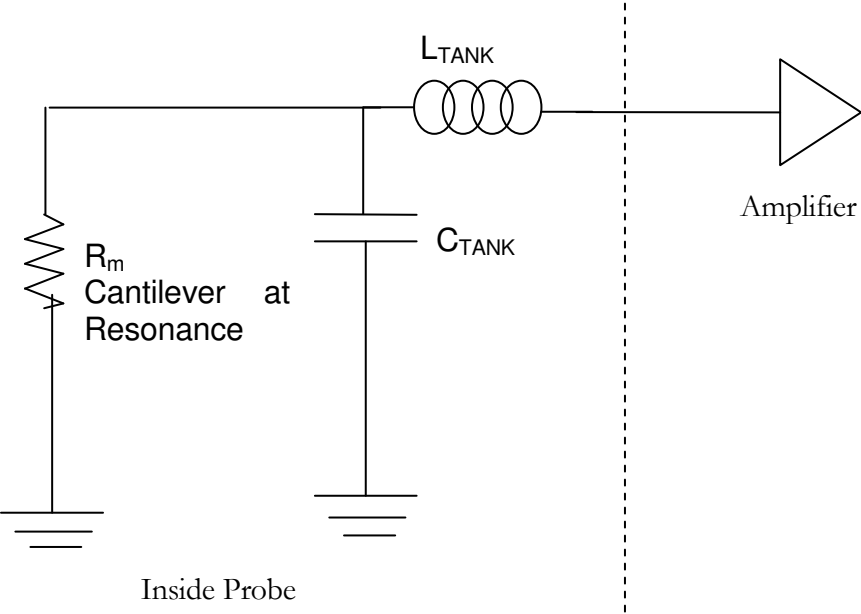


Figure 7.1 Transformation of Mechanical Impedance to the lower input impedance of amplifier by a tank circuit

For a room temperature, commercially available amplifier with a noise temperature of 40K, the calculated position detection sensitivity for $Q=15000$ is 2×10^{-21} N/ $\sqrt{\text{Hz}}$. Thus it is clear that the impedance transformation technique is quite powerful in eliminating signal division due to parasitic capacitance. The thermomechanical noise for this geometry at 40 K (the noise temperature of the amplifier) is $8\text{aN}/\sqrt{\text{Hz}}$.

The above formalism describes the extreme sensitivity that can be obtained by a simple capacitive detection scheme using an impedance transformation. The sensitivity of this scheme can be greatly improved with the availability of amplifiers with low input impedance and low noise temperatures. One such amplifier is a superconducting quantum interference device or the SQUID. SQUIDs are renowned for their very low current noise ($<1\text{pA}/\sqrt{\text{Hz}}$) and are used extensively in low noise applications such as radio astronomy.

Impedance matching by itself is not a simple process, given that the tank circuit requires very high value inductors as above. However, this is a technical issue that can be resolved through the judicious use of a series of impedance transforming elements such as transformers and tank circuits designed such the stray capacitance is eliminated. Also the bond-pads can easily be reduced in area (since the current pads are $220\mu\text{m}$ on a side, and wire bonding can be done to pads as small as $50\mu\text{m} \times 50\mu\text{m}$).

It is also noted that SQUIDs typically have very low input impedances. SQUID inputs are complex, but the inductive part of the input can be resonated away using a capacitor. For the SQUID described in [43], the resistive part of the input impedance for the frequencies of the cantilevers in this dissertation is calculated to be as low as $\sim 10^6 \Omega$. Direct impedance transformation would require very high inductance values with high Q, thus requiring bulky superconducting inductors. Hence a scheme gradually step down the impedance to the value of the SQUID input needs to be developed.

7.3 Contributions

The contributions of this dissertation are as follows:

1. The fabrication of ultra-thin single crystal silicon cantilevers required for initial experiments in Magnetic Resonance Force Microscopy. This entailed the development of a method to easily and reliably suspend cantilevers on an edge. The Dicing Saw Method described in Section 2.9 is a new method developed in this dissertation that can considerably lower manufacturing costs [24].
2. The design of an integrated, light-free position detection scheme based on capacitive detection with potential for zeptonewton force sensitivity. This is the first scheme for integrated, light-free detection of cantilevers for MRFM.

3. Fabrication of double capacitive cantilevers in crystalline Gallium Arsenide. The resonating cantilever to be used for MRFM measurements was only 30nm thick, and was the first report of such a thin cantilever [31].
4. The design and fabrication of FETs in Gallium Arsenide heterostructures and their characterization at 4.2 K.
5. Laid the groundwork for future research towards single spin sensitivity using capacitive detection schemes, and established a plan to accomplish this goal.

7.4 Towards Single Spin Sensitivity – Future Work

In this dissertation, I have described my efforts towards realization of a capacitive position detection scheme. In Section 7.2, I describe the use of an impedance matching technique that has potential for ultra-sensitive force detection using capacitive detection. As evidenced in Chapter 6, it is very useful and perhaps necessary to know the frequency of the cantilevers in advance of an all-electrical read-out.

Thus, locating the frequency of the cantilevers using an alternate method prior to all-electronic detection is probably the most straightforward and practical approach towards single spin sensitivity. I propose the following plan towards attaining the goal of a light-free technique for single spin sensitivity: -

1. Find the most user-friendly technique to locate the frequency of the cantilevers at room temperature. This can most likely be done using SEM-based detection, or by optical detection. Both methods have required sensitivity as described elsewhere, but the SEM method is more widely available, and can be used as part of the imaging process.
2. Once the frequency of the cantilever is located, and its Q at room temperature is known, this would give an idea to the most ideal technique for detection. Note that high Q s would lend very well to impedance matching techniques, since then, the inductance required for the tank circuit would be more practical.
3. If the impedance matching technique is unsuitable, then integration of the FET with the mechanical elements can be carried out. Since both parts have been realized separately in this dissertation, this should be an attainable goal.
4. Once this technique has been demonstrated, a suitable geometry with low thermomechanical noise can be designed using the spreadsheet in Appendix C. Smaller beams would probably be better suited to direct impedance matching techniques. The amplifier to be used must have very low current noise at the cantilever frequency - this can possibly be a SQUID.

Appendix A

EXPRESSING MECHANICAL MOTION IN ELECTRICAL TERMS

A mechanical element in motion and with a sense electrode for capacitive detection is represented in a circuit as a variable capacitor. Once biased with a large DC source (large such that it is practically constant as compared to the time constant of the resonator), this changing capacitor functions as an AC source in the circuit with a frequency corresponding to that of mechanical motion. This is the basis of capacitive detection in MEMS devices.

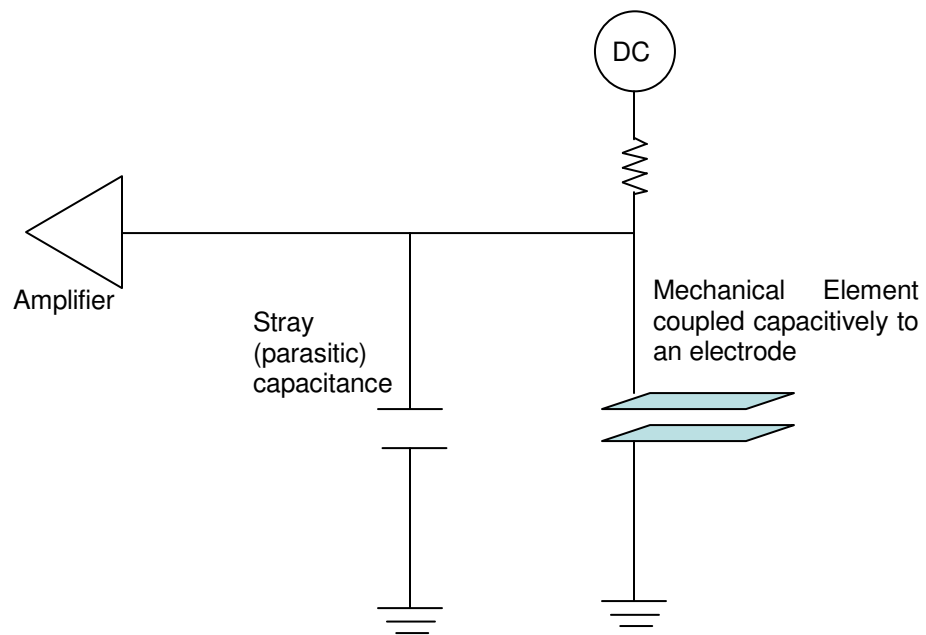


Figure A.1 Representation of a mechanical element (moving) coupled to a sensing electrode for capacitive sensing.

Reflectometry measurements are very common for capacitive sensing. However, reflectometry methods typically require very well matched impedances. The following formalism follows Keith Schwab and colleagues' technique to model nanomechanical in terms of impedances. When the resonator is displaced, the electrical capacitance between the resonator and the gate, C_{Cant} , is modified. For small relative displacements, $x(t)$, the capacitance is given by

$$C_{Cant}^x(x(t)) = \frac{C_{Cant}}{\left(1 + \frac{x(t)}{d}\right)} \approx C_{Cant} \cdot \left(1 - \frac{x(t)}{d}\right), \quad (\text{A-1})$$

where d is the resonator-gate separation, and $x \gg d$. A potential difference, V_{Bias} , between the resonator and the gate is established in addition to an oscillating potential $V_s(t) = V_s e^{i\omega t}$. These voltages will create forces which

cause the resonator to move. The motion will be given by Newton's Laws:

$$m\ddot{x} + \gamma\dot{x} + kx = F(t), \quad (\text{A-2})$$

where m is the mass, γ is the linear dissipation constant, k is the mechanical spring constant, and the dots refer to the first and second derivative with respect to time. The force between the gate and the resonator is given by:

$$\begin{aligned} F(t) &= -\frac{\partial U}{\partial x} = -\frac{\partial}{\partial x} \left(\frac{1}{2} C_{Cant}^x(x(t)) \cdot (V_{Bias} + V_s e^{i\omega t})^2 \right) \\ &\approx \frac{1}{2} \frac{C_{Cant}}{d} \cdot (V_{Bias}^2 + 2V_{Bias} V_s e^{i\omega t} + V_s^2 e^{2i\omega t})^2 \end{aligned} \quad (\text{A-3})$$

where we have assumed that the displacements are small $x(t) \ll d$. The first term is constant, causing a static deflecting, and is not important for this discussion. The third term oscillates at twice the applied frequency and also is not important here. The second term will produce a driving force at the applied frequency and is inserted into Equation 3.2:

$$\ddot{x} + \frac{\gamma}{m} \dot{x} + \omega_0^2 x = \frac{C_{\text{Cant}} V_{\text{Bias}}}{dm} V_s e^{i\omega t} \quad (\text{A-4})$$

where $\omega_0 = \sqrt{\frac{k}{m}}$. Assuming a harmonic solution for $x(t) = x(\omega)e^{i\omega t}$, we

find:

$$x(\omega) = \frac{C_{\text{Cant}} V_{\text{Bias}}}{dm} \frac{V_s}{\omega_0^2 - \omega^2 + i \frac{\omega \omega_0}{Q}} \quad (\text{A-5})$$

where $Q = \frac{m\omega_0}{\gamma}$. Using $Q = CV$, and Equation 3.2, the charge on the

gate is given by:

$$\begin{aligned} Q &= C_{\text{Cant}}^x (x(t))(V_{\text{Bias}} + V_s e^{i\omega t}) = C_{\text{Cant}} \cdot \left(1 - \frac{x(\omega)e^{i\omega t}}{d}\right) (V_{\text{Bias}} + V_s e^{i\omega t}) \\ &= C_{\text{Cant}} (V_g + V_s e^{i\omega t}) - \frac{C_{\text{Cant}} x(\omega)e^{i\omega t}}{d} (V_{\text{Bias}} + V_s e^{i\omega t}) \\ &\approx C_{\text{Cant}} (V_{\text{Bias}} + V_s e^{i\omega t}) - \frac{C_{\text{Cant}} V_{\text{Bias}} x(\omega)e^{i\omega t}}{d} \end{aligned} \quad (\text{A-6})$$

where we have dropped the piece oscillating at 2ω , which is small.

The time derivative to Equation 3.6 will give the current:

$$\begin{aligned}
I = \dot{Q} &= i\omega C_{Cant} V_s e^{i\omega t} - \frac{i\omega C_{Cant} V_{Bias} x(\omega) e^{i\omega t}}{d} \\
&= \left[i\omega C_{Cant} - i\omega \frac{C_{Cant}^2 V_{Bias}^2}{d^2 m} \frac{1}{\omega_0^2 - \omega^2 - i\frac{\omega\omega_0}{Q}} \right] V_s e^{i\omega t}
\end{aligned} \tag{A-7}$$

Comparing the equations in Equation 3.7, it is clear that motion produces electrical current, I_{RLC} :

$$I_{RLC} = -\frac{i\omega C_{Cant} V_{Bias}}{d} x(\omega) e^{i\omega t} \tag{A-8}$$

This will be a useful expression for understanding the position sensitivity.

Defining the total impedance, $Z_T(\omega)$, as $I = \frac{1}{Z_T(\omega)} V_s e^{i\omega t}$, one can see that

the current is given by two parallel contributions, through the capacitance C_g , and through a parallel RLC circuit shown in Figure 3.4. The impedance of the parallel combination of C_g and the RLC circuit is given by:

$$\begin{aligned}
Z_T(\omega)^{-1} &= i\omega C_{Cant} + Z_{RLC}(\omega)^{-1} \\
Z_{RLC}(\omega) &= i\omega L_m + \frac{1}{i\omega C_m} + R_m
\end{aligned} \tag{A-9}$$

giving currents through the RLC circuit:

$$I_{RLC}(\omega) = \frac{V_s e^{i\omega t}}{Z_{RLC}(\omega)} = -i\omega \frac{V_s e^{i\omega t}}{L_m \left[\omega_0^2 - \omega^2 + i\frac{\omega\omega_0}{Q} \right]} \tag{A-10}$$

where $\omega_0^2 = \frac{1}{L_m C_m}$, and $Q = \frac{\omega_0 L_m}{R_m}$. Comparing Eq. 10 and Eq. 7, it is

apparent that:

$$\begin{aligned} L_m &= \frac{d^2 m}{V_{Bias}^2 C_{Cant}^2} \\ C_m &= \frac{V_{Bias}^2 C_{Cant}^2}{\omega_0^2 d^2 m} \\ R_m &= \frac{d^2 m}{V_{Bias}^2 C_{Cant}^2} \frac{\omega_0}{Q} \end{aligned} \tag{A-11}$$

Thus the mechanical motion can be completely modeled by an equivalent RLC circuit with circuit values shown in Equation 3.11. This formality will be useful in future discussions pertaining to the impedance of the circuit and impedance matching techniques. This formality is not novel, but has been employed in MEMS filters for several years [28]. However, the use of this electrical analogue for impedance matching in order to do ultrasensitive detection in nanomechanical resonators was recently demonstrated by Schwab et.al. (Unpublished paper).

Appendix B

THE EXPERIMENTAL SET-UP

The printed circuit board was a five layer board with soft gold plating to allow for gold-wire bonding. There is a central ground plane that is connected to a grounded area on either side of the board. These grounded areas are used for mounting the chips and for attaching grounding copper wires to allow for proper thermalization. The board was attached to the end of a stainless steel probe made for the purpose of experimentation at low temperatures (up to 4.2K). The attachment was a 10-wire PCB edge connector. The PCB was custom made to fit into the edge connector. This allowed for ease of mounting the chips on the board and then inserting the board into the edge connector. Pictures of the board are shown in Figure B.1.

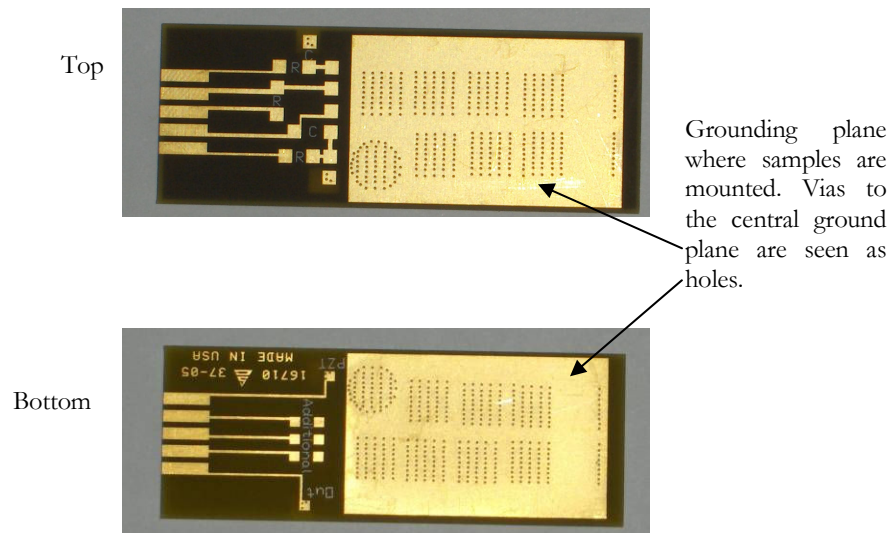


Figure B.1 Both sides of the circuit board are shown

The edge connector was firmly attached to the bottom end of the probe. Ten stainless steel coaxial cables with Teflon coating (Lakeshore Coax Cable CC-SS-500) were attached to the edge connector. These coaxial lines were then soldered on to hermetic BNC connectors at the top of the probe. The shields of the coaxial cables were grounded at the top. The bottom of the probe and the circuit board is shown in Figure B.2.

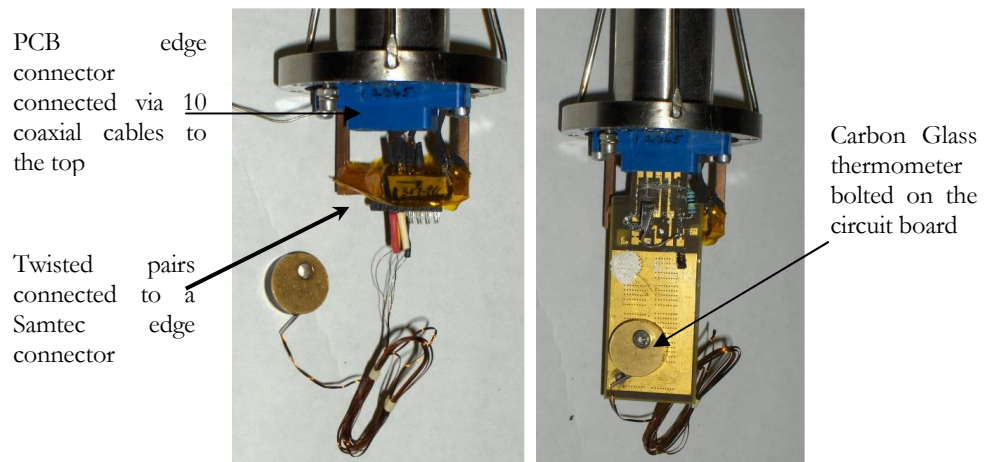


Figure B.2 The bottom of the probe showing the connections and the board attachment

In addition to the coaxial cables, six twisted pairs were also connected to a SAMTEC connector at the bottom of the probe. The twisted pairs were connected to a Fisher (Fischer 105, 24 pin) connector at the top. Four of the leads are used for connecting a Lakeshore CGR-1-2000-CD carbon-glass thermometer that was capable of accurate temperature measurement up to 1K.

The thermometer was calibrated at the factory. The probe is shown in Figure B.3.



Figure B.3 Clockwise from left: The probe; close up of the top of the probe showing the BNC connectors, pressure gauge and the evacuation valve; The bottom can and that can be screwed on hermetically with an indium seal.

Appendix C (Electronic file)

SPREADSHEET TO ESTIMATE CAPACITIVE DETECTION PARAMETERS

This Spreadsheet estimates values of thermomechanical noise and position detection sensitivity for capacitive detection, using rectangular cantilevers
 To find values, change any values highlighted in green. Note the units in the adjacent column. The highlighted cells in blue gives sensitivity estimates
 The cells highlighted in yellow give values for the circuit analysis as well as circuit component values.
 ALL VALUES ARE IN SI UNITS UNLESS OTHERWISE NOTED

GaAs Capacitive Scheme Parameters			
	Thickness is	30.00 nm	
	The length is	10.00 Microns	
	and width is	3.00 Microns	
	for a gap of	3.00 Microns	
Beam Parameters			
Young's Modulus	E	8.55E+10 Pa	Boltzman 1.38E-23 SI units
Thickness in m	t	3.00E-08 m	Q 15000
Width in m	W	3.00E-06 m	T 4.2 K
Length in m	L	1.00E-05 m	
	density	5320 kg/m ³	
Area of the cantilever	Area	3.00E-11 m ² =	3.00E-07 cm ²
Capacitive Gap in m	Cap. Gap	3.00E-06 m =	3.00E+00 um ²
Mass of cantilever	m	1.15E-15 SI units	
Stiffness	k	1.73E-03 N/m	
Resonance Frequency	fc	1.95E+05 Hz	
Frequency	w0	1.17E+06	
	4kkt	4.01E-25	2pifQ 5.78E+10
Thermomechanical Noise Calculated	Sf-thermal	2.63615E-18	Sd due to thermal noise 2.28E-11
	Capacitance calculations		
Capacitance of the cantilevers	C	8.85E-17	
Calculated Pull-in volts	Pull-in Vol	10.83426767 Volts	
		10834.26767 Millivolts	
80% of pull-in voltage		8.667414136	
Voltage Noise of amplifier	Amplifier Noise	50 nV/Rt. Hz	If parasitic capacitance can be resonated away
Position detection sensitivity with parasites	Sd	3.74E-10	No Parasite: 1.73E-14
Corresponding force sensitivity with parasites	Sf-detector	4.31899E-17	Sf 2.00E-21
Circuit Analysis			
The following are values for an equivalent circuit to the mechanics	Lm	17576.89893 H	
	Cm	4.14E-17 F	
This is the 'mechanical' impedance	Rm	1.37E+06 ohm	
This is the required tank circuit impedance	Z-tank	8285.433712 ohm	using Z-LC=SQRT(Rm*50)
Corresponding L of tank	L-tank	7.07E-03 H	Q for Tank 1.66E+02
C of tank	C-tank	1.03009E-10 F	
Assuming 220x220 um total area, bond pads that are 150X150 Assuming a projection of 50um length and 20um width	Parasitic Capacitance estimates		
	Area of bond pads	4.84E-08	
	Projection area	0.000000001	
	Total	4.94E-08	
	Bond_pad Capacitance	1.79E-12 F	
	Wirebond Capacitance	1.00E-13	
	HEMT Input	2.10E-14	
	Total Parasites	1.91E-12	
Casimir Force	Force	5.93E-11 N	
Force Required to bring plates together	Force	5.19E-09 N	
Is this Design OK for Casimir Force?			
Yes, Casimir Forces are not sufficient to cause stiction			

Figure C.1 Snap-shot showing the spreadsheet that is attached as an electronic file to this dissertation

References

- [1] Cleland, A, *Foundations of Nanomechanics*, Springer Verlag, 2002.
- [2] De Borst, R.; Sluys, L.J.; Muhlhaus, H.-B.; Pamin, J.; “Fundamental issues in finite element analyses of localization of deformation,” *Engineering Computations*, vol.10, no.2, 1993.
- [3] Schwab, K.C.; Henriksen, E.A.; Worlock, J.M.; Roukes, M.L.; “Measurement of the Quantum of thermal conductance,” *Nature*, vol.404, no.6781, 2000.
- [4] Knobel, R.G.; Cleland, A.N.; “Nanometer-scale displacement sensing using a single electron transistor,” *Nature*, vol.424, no.6946, 2003.
- [5] LaHaye, M.D.; Buu, O.; Camarota, B.; Schwab, K.C.; “Approaching the quantum limit of a nanomechanical resonator,” *Science*, vol.304, no.5667, 2004.
- [6] Naik, A.N.; Buu, O.; LaHaye, M.D.; Armour, A.D.; Blencowe, M.P.; Clerk, A.A.; Schwab, K.C.; *Nature*, In press 2006
- [7] Mamin, H.J.; Rugar, D.; “Sub-attoneutron force detection at millikelvin temperatures,” *Applied Physics Letters*, vol.79, no.20, 2001.
- [8] Alcalá, J.; Giannakopoulos, A.E.; Suresh, S.; “Continuous measurements of load-penetration curves with spherical microindenters and the

estimation of mechanical properties,” *Journal of Materials Research*, vol.13, no.5, 1998.

- [9] Fritzsche,W.; Takac,L.; Henderson,E.; “ Application of Atomic Force Microscopy to Visualization of DNA, Chromatin, and Chromosomes,” *Critical Reviews in Eukaryotic Gene Expression*, vol.7, no.3, 1997.
- [10] James, T.L.; *Fundamentals of NMR*, Chapter 1, <http://www.biophysics.org/education/james.pdf>
- [11] Sidles, J.A.; “Noninductive detection of single-proton magnetic resonance,” *Physics Review Letters*, Vol.58, 1991.
- [12] Kane, B.E.; “A silicon-based nuclear spin quantum computer,” *Nature*, vol.393, no.6681, 1998.
- [13] Mamin, H. J. and Rugar, D.; “Sub-atonewton force detection at millikelvin temperatures,” *Applied Physics Letters*, vol. 79, 2001.
- [14] Gabrielson, T. B.; “Mechanical-Thermal Noise in Micromachined Acoustic and Vibration Sensors,” *IEEE Trans. Electron Devices*, vol. 40, no. 5, 1993.
- [15] Stowe, T.D.; Yasumura, K.; Kenny, T.W.; Botkin, D.; “Attonewton force detection using ultrathin silicon cantilevers,” *Applied Physics Letters*, vol.71, no.2, 1997.
- [16] Rugar, D; Budakian, R; Mamin, HJ; Chui, B.W.; “Single spin detection by magnetic resonance force microscopy,” *Nature*, Vol 430, 2004

- [17] Mozyrsky, D; Martin, I.; Pelekhov, D.; Hammel, P.C.; “Theory of spin relaxation in magnetic resonance force microscopy,” *Applied Physics Letters*, Vol. 82, No. 8, 2003.
- [18] Berman, G.P.; Gorshkov, V.N.; Rugar, D.; Tsifrinovich, V.I.; “Spin relaxation caused by thermal excitations of high-frequency modes of cantilever vibrations,” *Physical Review B (Condensed Matter and Materials Physics)*, vol.68, no.9, 2003.
- [19] Hosaka, S; Etoh, K; Kikukawa, A; Koyanagi. H; “Megahertz silicon atomic force microscopy .AFM. cantilever and high-speed readout in AFM-based recording,” *Journal of Vacuum Science and Technology B*, vol. 18, no. 1, 2000.
- [20] Mamin, H.J.; Rugar, D.; “Sub-attoneutron force detection at millikelvin temperatures,” *Applied Physics Letters*, vol.79, no.20, 2001.
- [21] Perkin Elmer Instruments 7280 DSP lock-in amplifier.
- [22] Staveley NDT Technologies, EBL-4 piezoelectric stack, <http://www.staveleyndt.com/products/ebllzt.html>.
- [23] Pelekhov D.V.; Selcu, C.; Banerjee, P.; Fong K.C.; Hammel, P.C.; Bhaskaran, H.; and Schwab, K.; ‘Lightfree magnetic resonance force microscopy for studies of electron spin polarized systems ,’ V. 286, *Journal of Magnetism and Magnetic Materials*, 2005

- [24] Bhaskaran, H; “Method to Suspend Micro/ Nanocantilevers on an edge,”
Invention disclosure, University of Maryland, Patent pending, 2006
- [25] Beck, R.G.; Eriksson, M.A.; Topinka, M.A.; and Westervelt, M.;
“GaAs/AlGaAs self-sensing cantilevers for low temperature scanning
probe microscopy,” *Applied Physics Letters*, Vol. 73, No. 8, 1998.
- [26] Cho, Y.-H.; Kwak, B.M.; Pisano, A.P.; Howe, R.T.; “Viscous energy
dissipation in laterally oscillating planar microstructures: a theoretical
and experimental study,” *Proceedings. IEEE. Micro Electro Mechanical
Systems. An Investigation of Micro Structures, Sensors, Actuators,
Machines and Systems (Cat. No.93CH3265-6)*, New York, NY, USA:
IEEE, 1993.
- [27] Mar, D. J.; Westervelt, R. M.; Hopkins, R. F.; “Cryogenic field-effect
transistor with single electron charge sensitivity,” *Applied Physics
Letters*, Vol. 64, No. 31, 1994.
- [28] Liwei Lin; Howe, R.T.; Pisano, A.P.; “Microelectromechanical filters for
signal processing,” *Journal of microelectromechanical systems*, Vol. 7,
No. 3, 1998.
- [29] Sedra, A.S.; Smith, K.C.; *Microelectronic Circuits*, Oxford University
Press, 1998
- [30] Horowitz, P; Hill, W; *The Art of Electronics*, Cambridge University
Press, 1998

- [31] Bhaskaran, H; Pelekhov, D.V.; Hammel, P.C.; Schwab, K;
“Development of Ultra-sensitive Capacitive Readout for Magnetic
Resonance Force Microscopy,” Proceedings of Integrated
Nanosystems: Design Synthesis and Application, Berkeley, CA, 2005.
- [32] The author acknowledges Chris Richardson, Kanakraju Subramanian
and Lynn Calhoun for growing wafers of the required cross section for
fabrication of double capacitive cantilevers.
- [33] Agilent Technologies Technical Data Sheet; “Low Noise Pseudomorphic
HEMT in a Surface Mount Plastic Package,” Part number ATF-35143,
2004
- [34] Oukhanski, N.; Grajcar, M.; Il'ichev, E.; Meyer, H.-G.; “Low noise, low
power consumption high electron mobility transistors amplifier, for
temperatures below 1 K,” *Review of Scientific Instruments*, Vol. 74, No.
2, 2003.
- [35] Junmin Hu; Beck, R. G.; Tao Deng; Westervelt, R. M.; Maranowski, K.
D.; Gossard, A. C.; Whitesides George M.; “Using soft lithography to
fabricate GaAs/AlGaAs heterostructure field effect transistors,” *Applied
Physics Letters*, Vol. 71, No. 14, 1997
- [36] William, R.E.; *Gallium Arsenide Processing Techniques*, Artech House,
Inc., 1984.

- [37] Staveley NDT Technologies, EBL-3 Piezoelectric stack, <http://www.staveleyndt.com/products/ebllzt.html>.
- [38] The author is grateful to Eyal Buks and Inna Kozinsky for very enlightening discussions and helpful suggestions
- [39] Buks, E; Roukes, M.L.; “Stiction, adhesion energy, and the Casimir effect in micromechanical systems,” *Physical Review B* Vol. 63: No.3, 2001
- [40] Kouh, T.; Karabacak, D.; Kim, D. H.; Ekinici, K. L.; “Diffraction effects in optical interferometric displacement detection in nanoelectromechanical systems,” *Applied Physics Letters*, Vol. 86 2005
- [41] Karabacak, D.; Kouh T.; Ekinici, K. L.; ” Analysis of optical interferometric displacement detection in nanoelectromechanical systems,” *Journal of Applied Physics*, Vol. 98, 2005
- [42] Lahaye, M.L.; *The Radio-Frequency Single-Electron Transistor Displacement Detector*, PhD Dissertation, University of Maryland 2005.
- [43] Falferi, P.; “ $120 \text{ } \hbar$ SQUID amplifiers with a high- Q resonating input load,” *Classical and Quantum Gravity*, Vol. 21, 2004
- [44] Shekhawat, G.; Tark, S-H; Dravid, V.P.; “MOSFET-Embedded Microcantilevers for Measuring Deflection in Biomolecular Sensors,” *Science*, Vol. 311, No. 5767, 2006

[45] Bhaskaran, H.; Schwab, K.C.; “An Integrated Capacitively Detected Micromachined/ Nanofabricated Cantilever Force Detector Coupled to a Transistor,” Invention Disclosure, University of Maryland (2004)